



ΠΑΝΕΠΙΣΤΗΜΙΟ ΚΡΗΤΗΣ
UNIVERSITY OF CRETE



FORTH
INSTITUTE OF ELECTRONIC STRUCTURE AND LASER



University of Crete
School of Sciences
Department of Materials Science and Technology

Doctor of Philosophy thesis

3D Mechanical Metamaterial Scaffolds for Tissue Engineering Applications

George Flamourakis

Supervisor: Prof. K. Velonia
Advisors: Dr. M. Farsari & Dr. A. Ranella

Heraklion, Crete
September 2022

Table of Contents

Table of Contents	1
Acknowledgments	5
Abstract.....	6
Chapter 1.....	8
1 Introduction	8
1.1 Scaffolding in Tissue engineering	8
1.2 The Contribution of Metamaterials in Tissue Engineering	9
1.2.1 Auxetic metamaterials	11
1.2.2 Non-Auxetic	14
1.2.3 Tuneable porosity	15
1.2.4 Tuneable stiffness	16
1.2.5 Other applications.....	17
1.3 4D bioprinting advances	18
1.3.1 Metamaterials in bone tissue engineering	21
1.4 Light- assisted fabrication methods of Mechanical Metamaterials.....	22
1.4.1 Multiphoton lithography.....	24
1.5 Extrusion based	24
1.6 Future perspectives and issues	25
1.7 Purpose of thesis and outline	25
2 Theoretical background	35
2.1 Multiphoton absorption	35
2.2 Difference in the cross section of the focused spot in 1PA and 2PA.....	36
2.3 The focal volume (voxel).....	37
2.4 Multiphoton polymerization.....	40
2.5 Two-step absorption instead of two-photon absorption	42
2.6 Stereolithography.....	42
2.7 Fluorescence mechanism.....	43

2.8	Materials for MPL	44
2.8.1	Organics	45
2.8.2	Hybrid materials	45
2.9	Materials mechanical properties	46
2.9.1	Stress- strain curve	47
2.9.2	Hooke's law	48
2.10	Metamaterials	49
2.11	Auxetic metamaterials	50
2.12	Ultralight, Ultra-stiff mechanical metamaterials	50
2.13	Tissue Engineering	52
2.13.1	Biomaterials	53
2.14	Mechanical Stress types cells experience	56
2.15	Cell Mechano-sensing and Mechano-transduction	56
2.15.1	Focal Adhesion Kinase (FAK)	57
2.15.2	Hippo pathway	58
2.15.3	YAP/TAZ complex	60
2.16	Bone regeneration	60
2.16.1	Runx2 is affected by YAP	61
Chapter 3		71
3	Materials and Methods	71
3.1	Material Synthesis	71
3.2	Scaffold fabrication using Multiphoton Lithography	72
3.3	3D printer and resin	74
3.4	3D printer scaffold preparation	75
3.5	Nano dynamic Mechanical Measurement and Analysis (Nano-DMA)	75
3.6	Cell culturing	75
3.7	SBB treatment	76
3.8	Live/Dead assay	77
3.9	Scanning Electron Microscopy	78

3.10	Immunofluorescence staining	79
3.11	Differentiation medium	80
3.12	DAB staining	80
3.13	Confocal microscopy.....	80
3.14	Real time PCR analysis	81
Chapter 4.....		85
4	Results	85
4.1	Mechanical simulations	85
4.1.1	Auxetic bowtie	85
4.1.2	Kelvin foam	86
4.1.3	Auxetic v.2 scaffold	87
4.2	Characterization of mechanical properties of the photoresin SZ2080.....	88
4.3	Fabrication of the bowtie Auxetic scaffold	91
4.4	NIH-3T3 fibroblast cell line interactions with the Auxetic scaffold.....	94
4.5	High polymer autofluorescence inhibits the use of advanced imaging methods.....	96
4.6	Unlocking the confocal potentials: the Sudan Black B photoinitiator variant of SZ2080.....	97
4.7	SBB cell study in simple geometries	99
4.8	SBB variant in mechanical metamaterials	101
4.9	Cell Morphology of MSCs with mechanical Metamaterials.....	103
4.10	Cell Penetration and directionality studies.....	104
4.11	Cell Morphology in differentiation conditions.....	106
4.12	Runx2	110
4.13	Runx2 gene expression	112
4.14	Yap protein.....	114
4.15	Summary	116
4.16	Breaking the size barrier: SLA method	118
Discussion.....		120

5	<i>List of publications</i>	<i>128</i>
6	<i>List of conferences.....</i>	<i>129</i>
7	<i>Funding.....</i>	<i>130</i>

Acknowledgments

First of all, I would like to thank my supervisors, Dr. Maria Farsari, Primal Investigator of the Non-Linear Lithography group of the Institute of Electronic Structure and Laser at Foundation of Research and Technology Hellas (IESL/FORTH), Dr. Anthi Ranella, PI of Tissue Engineering and Regenerative Medicine and Immunoengineering group of IESL/FORTH and Prof. Kelly Velonia, PI of the Synthetic Biomaterials group in Department of Materials Science and Technology of University of Crete for their guidance and numerous hours of discussions and brainstorming. Their help was absolutely catalytic for achieving my goals and fulfilling this work during those difficult pandemic years.

I would like to thank the senior members of both groups, Dr. Vaso Melisinaki and Maria Manousaki for their valuable help and discussion about laser technologies and fabrication optimizations, Dr. Elmina Kampouraki for her expertise in material synthesis, Dr. Gordon Zyla for inspiration and great collaboration in problem-solving. Also, Dr. Phanee Manganas, Dr. Lina Papadimitriou, and Dr. Evi Kavatzikidou for discussing with me the biological barriers and challenges I faced.

Of course, and most importantly, all of my fellow PhD students who started this journey almost the same period as me and struggled together. Thank you, Dimitra Ladika, for the support, and mentorship you gave me all those years as I found a real friend in you, and Antoni Korda for the support and the experiments we did together for our publications.

Special thanks to an older member of the NLL group, Ioannis Spanos, for teaching me 3Dpoli coding and most importantly for helping me with my first publication. I would also like to thank Dr. Zacharias Vangelatos from Berkeley University for his valuable help in nanoindentation experiments and our SEM technician Aleka Manousaki for countless hours spend with me on SEM microscope trying to capture as better image as possible.

Furthermore, special thanks to all members of both groups for making my years in PhD pass a little more enjoyable with all our fun having within the institute and out. I would like to thank Maria Papageorgiou and Vaso Pateraki for the excellent collaboration we had for the 3D printer experiments and the writing of the paper. Lastly, I'd like to acknowledge my parents and my sister for truly supporting me all those years.

Without you all, this work would never be possible. Thank you

Abstract

The aim of this thesis is to utilize the unlimited versatility of light- based additive manufacturing alongside with the formulation of photoresins in order to produce different mechanical metamaterial structures that will be used as scaffolds for the study of cellular responses of different cell lines. Furthermore, this study investigates in great depth the osteogenic differentiation potential of those environments in Mesenchymal Stem Cell differentiation.

For the purpose of the study, two main mechanical metamaterial scaffolds were fabricated by Multiphoton Polymerization on flat glass substrates. More precisely, i) Auxetic scaffolds that display negative Poisons' Ratio were fabricated and characterized, and ii) tetrakaidekahedron lattice (popularly known as Kelvin foam) that shows great stiffness while being extremely lightweight. Both metamaterials were fabricated using the hybrid organic-inorganic photresin SZ2080TM. For the fabrication of the fluorescent free version of those scaffolds, a novel approach was followed where the photoinitiator of the material was replaced by a dye that was later used as a post fabrication treatment of the polymeric structure in order to quench the high levels of fluorescence. Moreover, several optimizations needed to take place as the scaffolds needed to have a large size in order to host a great number of cells to make accurate measurements.

Initially, an organic- inorganic photo resin was used to fabricate simple structure such as boxes and cylinders that were used in a nano indenter system to characterize its' mechanical properties. The results that we acquired showed that the polymerized material shows great hardness and stiffness which is proportional to the laser power of the system. Afterwards, using 3D software we created two different types of Auxetic scaffolds based on the bowtie geometry. Those scaffolds were simulated under axial force and the negative poison ratio was proved theoretically and experimentally. Following the simulations, several optimization steps were made to the fabrication procedure in order to 3D print high resolution- large scaffolds that then used for cell culturing. We proved that even the material itself is very hard with a Hardness of around 2GPa, due to the special geometry of the unit cells cell were able to bend and deform it easily without breaking it.

The second part of this thesis involves the development and optimization of a variant of SZ2080TM that has low autofluorescence. For that instance, Sudan Black B (SBB) dye was used as a replacement of the photoinitiator that the resin in synthesized by default with, and as a post fabrication treatment. We showed that SBB can initiate photo-polymerization with MPL

technique as we created complicated metamaterial scaffolds, and that the newly fabricated structures show 99% lower autofluorescence. Then, cytotoxicity assays were performed with MSCs, and confocal microscopy was used to visualize the cells in those scaffolds. As a result, this material is excellent for cell culture as no cytotoxicity was observed and confocal microscopy could be ultimately used for quantification of proteins in the cells.

The third part involves advanced biology experiments in an effort to study how auxetic mechanical environment affects the osteogenic differentiation of Mesenchymal Stem Cells (MSCs), as in recent years the effect of mechanical properties in that cell line has been thoroughly studied. More precisely, the two scaffolds mentioned before, were fabricated through Multiphoton Lithography (MPL) on the same glass substrate and MSCs were cultured on them for different time periods from 2 days to 28 days in the presence and absence of osteogenic differentiation medium. Then, the samples were fixed and observed with Scanning electron microscopy (SEM), and Confocal microscopy. Moreover, we developed a novel protocol in order to prepare the sample for Polymerase chain reaction (PCR) of the cells cultured on the scaffolds as this was a very challenging procedure due to the small size of the fabricated scaffolds. Lastly, we quantified two important proteins for mechanotransduction and differentiation: the Yes associated protein 1 (YAP) and Runx- related Transcription factor 2 (Runx2). Mechanotransduction, by definition, is the mechanism by which cells translate mechanical stimuli into cellular responses to a variety of mechanical loads and characteristics such as stiffness or Hardness. We showed that YAP protein is translocated to the nucleus in a higher ratio on Kelvin foam, where it remains in the cytoplasm on the Auxetic. Lastly, Runx2 shows an increase in the case of Auxetic scaffold, hinting the reverse relationship that those two proteins have. Analysis of those very complicated 3D environments was conducted with ImageJ through a novel custom pipeline developed especially for the need of this study.

Lastly, a new approach for the fabrication of large scaffolds was followed by using a stereolithographic approach with a commercially available 3D printer that uses photosensitive resin and a UV lamp to 3D print the structures. We showed that with this approach it is possible to create large mechanical metamaterial scaffolds from complicated STL files and use them with several different cell lines where no cytotoxicity was observed. In that way, the main drawback of the limited size is surpassed as a great number of cells can be cultured, and the scaffolds are easily manipulated.

Chapter 1

1 Introduction

1.1 Scaffolding in Tissue engineering

Apart from blood cells which resides in a flowing environment, almost all the other cell types in human tissues are anchorage-dependent, which means that they reside in a matrix called extracellular matrix (ECM) which most of the times is synthesized by cells themselves. There are plentiful types of ECM in human tissues, which usually have multiple physical characteristics and tissue-specific composition [1], [2]. As for the functions of ECM, they can be generally classified into five categories:

- Firstly, ECM provides structural support and physical cues for cells residing in that specific tissue.
- Secondly, ECM provides the tissue with specific mechanical properties, such as rigidity and elasticity that is associated with the tissue functions.
- Thirdly, ECM may actively provide bioactive cues to the residing cells for regulation of their activities [3].
- Fourthly, ECM can act as reservoir of growth factors and potentiate their bioactivities.
- Fifthly, ECM provides a degradable environment so as to allow neovascularization and remodelling in response to developmental, physiological and pathological challenges during tissue dynamic process.

Consequently, the best artificial scaffold for an engineered tissue should be closest the ECM of the target tissue in its native state. Nevertheless, the multiple functions, the complex composition and the dynamic nature of ECM in native tissues is extremely difficult to mimic. Therefore, contemporary concept of scaffolding in tissue engineering is to mimic the functions of native ECM. As a result, the important roles played by scaffolds in engineered tissues are analogous to the functions of ECM in native tissues and are associated with their architectural, biological, physical, and mechanical features[4], [5].

Scaffolds play an essential role in Tissue Engineering (TE) because they provide mechanical support, allow perfusion of nutrients and oxygen, transfer biochemical signals that

modulate cell behavior and can be used to potentially release drugs and growth factors. Furthermore, biomaterials that may be used for tissue regeneration must exhibit tailorable properties to enhance cell attachment, migration, growth, and differentiation, prevent undesirable host responses that may lead to inflammation at the biomaterial interface, display chemical and mechanical stability for providing structural support while demonstrating controllable microstructure and adequate porosity, and sometimes have good biodegradability without producing toxic residues and byproducts. Based on all those requirements, scaffolds are divided into 3 categories: architecture materials, hybrid or composite materials and hydrogels [6]. In particular, architected materials which are drawing the attention over the last years, can be created by various fabrication techniques, such as electrospinning, freeze-drying, gas foaming, solvent casting, particulate or porogen leaching, phase separation, self-assembly, and, most importantly, Additive Manufacturing (AM) [7].

Consequently, there is an important effort to mimic the ECM by fabricating scaffolds and provide the tissue with the right cues in order to keep cells proliferating and functioning as they were in the native tissue. That's the main reason why research has drawn attention over the last decades in scaffolding. Moreover, the 3D surrounding is the default environment that a cell experience and is far more different than the 2D experiments the fields of biology currently uses [8].

1.2 The Contribution of Metamaterials in Tissue Engineering

In the field of tissue engineering, one of the main goals is the design and engineer of the desired scaffold that can home cells and direct their functions. Mechanical metamaterials offer an opportunity to expand the forms of mechanical signals in a reproducible way, thus they can be utilized to fabricate advanced scaffolds to precisely tune the biological behaviors of cells and tissues. A new concept of “meta-biomaterial” has arisen, referring to the mechanical metamaterials with biomimicry properties that are barely found in conventional porous biomaterials [9]. Generally, there are five categories of mechanical metamaterials that have been used in TE: Auxetics, Non- Auxetics, Ultra -stiff, isotropic, triply periodic minimal surfaces (TPMS) and deployable (**Table 1**).

Those special metamaterials have been constructed to exhibit paradoxical physical phenomena [10], and most importantly negative Poisson's ratio, as was fabricated by Wagener *et al* by using two photon polymerization (TPP) [11]. Human brilliance, mathematical innovations, and occasionally nature were used as inspirations to construct innovative

structures with unusual capabilities. The class of such materials, known as metamaterials, first began in 1998 with the work by Harris *et al.* as porous implants [12] and comprises biomimetic materials generated using nature-derived structures. Mechanical metamaterials have also provided radical designs of functional tissue scaffolds, demonstrating remarkable promise in bone tissue regeneration and orthopedic implants[13], and even having a high surface-to-volume ratio [14].

Underlying microstructure governs the physical qualities of meta-biomaterials: for example, the properties of natural materials such as wood have been used to build hard tissue replacements [15]. Metamaterials have recently been proposed to augment implants and tissue scaffolds for various organs, however the scalability of existing production technologies limits the implementation of innovative microarchitectures in operational prototypes[16].

Natural-derived and synthetic hydrogels, which make up a substantial percentage of bioinks, not only imitate the ECM but also allow for the printability and manufacturability of cell-laden structures. Hydrogels offer a hydrated environment as well as mechanical supports, allowing hydrogel molecules to interact in 3D and promoting cell adhesion and proliferation [17]–[21]. There is a plethora of hydrogels currently used for TE applications. Alginate, hyaluronic acid, gelatin, collagen I, fibrin, agarose, and basement membrane are examples of naturally-derived hydrogels, whereas polyethylene glycol and poloxamers are examples of synthetically-derived hydrogels [22]. Decellularizing the natural tissue-specific ECM as a bioink solution for bioprinting cell-laden structures is one clever way and is currently trending [23]. Porcine cartilage, heart tissue extracted from animals, and adipose tissue from donors' liposuction operations were treated in one example of the decellularization procedure [24].

Table 1. Mechanical Metamaterials and their applications in TE.

Category	Characteristics	Material	Cell type/ application	Reference
Auxetic	Negative Poison's Ratio	PEGDA	10T1/2, proliferation, migration	[25]
		Negative photoresist	MSCs, attachment and migration	[26]
		Negative photoresist	C2C12 muscle precursor cells, myotube formation	[27]
		SZ2080 TM	NIH/3T3 fibroblasts, proliferation, penetration	[28]
		SZ2080 TM	MSCs, 3D tissue assembly	[29]
		Chitosan	Cardiac patch	[30]
Ultra- stiff	Lightweight scaffolds with high mechanical strength	GelMa	Schwan cells, proliferation, differentiation	[31]
		Ti6AL4V	BM-MSCs, osteogenesis	[32]
		Negative photoresist	Saos-2 cells, adhesion, mineralization	[33]
TPMS	Bone-like zero mean curvature	steel	Osteosarcoma cells, proliferation	[34]
		Ti	Bioactive bone implant	[35]
Deployable	origami	Shape memory alloy	Vascular stent	[36]

1.2.1 Auxetic metamaterials

The field of TE struggles to recreate the natural properties of such environments by the creation of special auxetic scaffolds. Recent studies have demonstrated the application of auxetics in TE [37], [38] as several biological tissues have been reported as behaving in an auxetic manner, defined by a negative Poisson's ratio such as skin, arteries, tendons, and cancellous bone [28]. Auxetic properties are not that common in nature but can be achieved by designing particular microstructured architectures and manufacturing them with varied materials and methods such as Additive Manufacturing (AM). Such structure was first proposed by Critchley *et al.* [39] where for the first time auxetic foams were manufactured and also, were customized and fabricated without any random cell orientation, providing a new methodology to generate foam structures with stability and homogeneity. This proposed geometry was then used by many studies as the reentrant honeycomb architecture, herein referred to as 'bowtie' auxetic scaffolds [11]. A re-entrant auxetic structure is developed from

the hexagonal honeycomb design by changing the internal angles of the unit cell so that has negative values instead of positive.

Recent study suggested the fabrication by Melt Electro Writing (MEW) of scaffolds with adjustable Poisson's ratio which is suitable in certain biological applications for mimicking the behavior of native tissue mechanics [40]. Another important area where auxetic scaffolds are very useful is their use as cardiac patches. Cardiovascular diseases (CVDs) are the leading causes of death and disability around the globe where biomaterials and tissue engineering research may be one of the most promising solutions. The human heart's Young Modulus has a range from 0.02 to 0.5 MPa making auxetic cardiac patches the perfect candidates for such a wide range as shown by a study from Kpnisi *et al.* [41].

Embryonic fibroblast cells were observed to distort laser-made auxetic lattices in an early investigation, whilst the lattice with the related positive Poisson's ratio showed negligible deformation [25]. The cells displayed linear or rounded morphology when grown on either re-entrant or chiral structures, as opposed to spherical or star-shaped morphology when grown on coverslips. Because the surface adhesion force was greater than the gravitational force, these MSCs attempted to climb onto the auxetic structures rather than falling through the holes. Furthermore, cell attachment deformed the auxetic structures and generated a shift in their resonance frequency, which can be employed as a sensor for cell development [26]. In another work, C2C12 myoblasts displayed effective muscle development on TPP-fabricated elastic auxetic micro-scaffolds. Under bipolar pulsed field stimulation, myotubes fused on these scaffolds demonstrated active actuation [27].

In recent study Wang *et al.* showed that by seeding MSCs on both octet truss and auxetic metamaterials, a mesenchymal microtissue model could be constructed. MSCs elongated and separated by the struts as individual cells on the octet truss structures, whereas auxetic structures facilitated cell aggregation and tissue development. Furthermore, Finite Element Analysis (FEA) simulation revealed that the deformation patterns for the metamaterials under biological stress differed significantly from the deformation patterns under standard mechanical loading tests [29]. The limitation of this work was that the size of the overall scaffolds was only 12 unit cells, which made it not ideal for a real life scaffolds where a large number of cells proliferate and adapt.

Cells produce compressive traction force on auxetic metamaterials, resulting in local densification of cellular units. This characteristic not only strengthens the material scaffolds under mechanical pressure, but it also helps to generate strong intercellular connections for 3D tissue construction. TPP was used to create auxetic scaffolds with two distinct pore size

diameters to facilitate 3D fibroblast culture [28]. Cells could penetrate and deform the structure in case of large pores, and also align to the unit cells direction.

The deformability and fracture resistance of auxetic structures show considerable benefits for building elastic patches for soft tissue regeneration. In recent work by Chen *et al.* extrusion-based bioprinting enabled the creation of a neural cell-laden auxetic patch capable of withstanding tensile forces of up to 20% strain [31]. Encapsulated Schwann's cells exposed to cyclic stretch had higher cell survival, proliferation rate, and nerve growth factor (NGF) production than cells exposed to static culture. The auxetic patch's exceptional flexibility and degradability may have a synergistic influence on its improved performance in nerve tissue regeneration.

The human heart is one of the most physically active organs, thus developing cardiac patches that can withstand dynamic mechanical loads is crucial. To address this issue, Kapnisi *et al.* created a micro-patterned auxetic patch with re-entrant honeycombs. The mechanical property of the auxetic patch may be adjusted by altering the diameters of cellular units to match the mechanical strength and structural anisotropy of the myocardium. *Ex vivo* research shown that auxetic patches might adapt to heart motions. The patch integrated well with the left cardiac ventricle after transplantation in a rat model with myocardial infarction (MI) and resulted in minor fibrotic responses. By two weeks, the MI rats with patch implantation had a substantial rise in left ventricular mass, which was predicted to reduce heart wall stress and attenuate hypertrophy [30].

The latest review by Haag *et al.* [42] included the most recent work done on auxetic scaffolds and tissue engineering (**Figure 1**). As an example, Olvera *et al.* used a "missing-rib" auxetic design to compensate for the restricted elastic deformation of poly(-caprolactone) (PCL). The missing-rib unit cell is created by selectively removing ribs from a network while maintaining the internal angles. Furthermore, the electrical demands of the heart muscle were addressed by covering the scaffold with polypyrrole, resulting in a cell-free electroconductive auxetic cardiac patch that matches the mechanical anisotropy of human myocardium [43].

Despite the intriguing features of auxetic meta-biomaterials, only a few research have been conducted to evaluate the biological response. As a result, we are only scratching the surface of how the negative Poisson's ratio influences the proliferation and differentiation of cells implanted in this environment. Scaffold design, on the other hand, begins at the nanostructure within the deposited fiber itself, which may be modified and regulated to further replicate the multiple levels of native hierarchy.

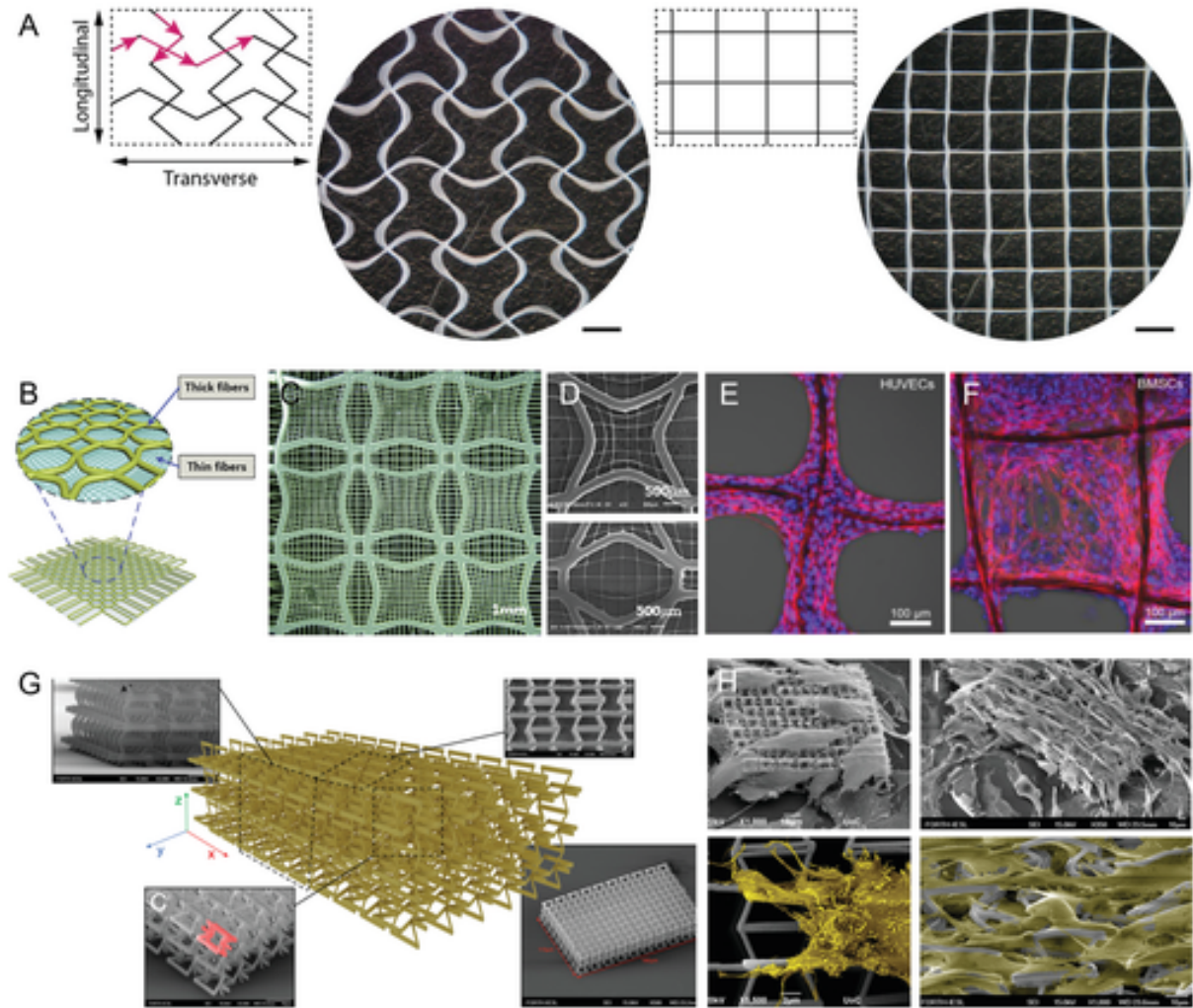


Figure 1. Auxetic mechanical metamaterials **A) D.** **B)** A multi-scale scaffold with configurable Poisson's ratio created by merging thick and thin fibers. **C)** An optical microscope view of the whole scaffold, which was created using a multi-scale direct writing approach. **D)** SEM photos of thick and thin fibers. **E, F)** Confocal laser-scanning pictures of scaffolds sown for 30 days with **E)** HUVECs and **F)** bone marrow stem cells. **G)** CAD model and SEM photos of an auxetic mechanical metamaterial scaffold with a re-entrant hexagonal structure through MPL. **H)** Scaffold with small pores and **I)** Scaffold with big pores seeded with mouse fibroblasts. Figure used with permission from [42].

1.2.2 Non-Auxetic

Non-auxetic structures, on the other hand, are typically bending-dominated topologies, such as diamond and rhombic dodecahedron, which results in a critical deformation under mechanical compression. Each node in a diamond unit has 16 identical edges and 14 vertices, and each node is connected to four others by an interior angle of 109.5° [44]. Such structure has been recently fabricated as a hip replacement structure [45] as it benefits from the fact that such architecture improves the compliance of biomaterials under mechanical force. In addition,

combining auxetic and non-auxetic structures with an optimized structural gradient could provide a moderate mechanical strength and smooth internal stress transition, which can be engineered as the next generation of tissue engineering scaffolds.

Inspired by biological membranes and block copolymers, nanolabyrinth structures are composed of triply periodic minimum surfaces (TPMS) with crystallographic group symmetry [46]. A minimal surface is one that is locally area-minimizing, meaning that a tiny section has the least feasible area for a surface spanning its border. Soap films is a characteristic example of them. Minimal surfaces must have zero mean curvature, which means that the sum of the principal curvatures at each point is also zero. Minimal surfaces with crystalline structures, in the sense of repeating themselves in three dimensions, are particularly intriguing, therefore named as triply periodic. Surface designs such as Schwarz P ("Primitive"), Schwarz D ("Diamond"), and Schwarz G ("Gyroid") can achieve zero mean curvature at each point on the surface by locally minimizing the surface area for a given boundary. Smooth surfaces, as opposed to lattice geometries, reduce stress concentration and prevent catastrophic collapse in the structure [47].

More crucially, they can be used to tune the anisotropic behaviors of the structures, making them compliant in some directions but exceedingly stiff in others. Because of their anisotropic features, nano-labyrinth structures are promising possibilities for bioimplants and ultra-light structures.

1.2.3 Tuneable porosity

Porosity is an important design characteristic for architected scaffolds because it influences cell activity and mass transfer. MSCs cultured on scaffolds with diamond crystal units and gradient density, for example, as shown by a study from Wang *et al.*, had increased alkaline phosphatase activity (ALP), an indication of osteoblast development, even though all scaffolds resulted in equal shape, viability, and proliferation rate [32]. High porosity at the outside layer of the scaffolds encouraged higher cell growth and avoided the occurrence of pore blockage, while low porosity at the interior layer of the scaffolds allowed for more cell adhesion, making this diamond crystal design unique.

In another study by Ma *et al.*, gyroid lattices were constructed using SLM from simulation-aided designs in order to better correlate the scaffold porosity and cellular behavior [34]. This particular geometry is a great example of a TPMS Porous Scaffolds. The major element that encouraged cell proliferation was discovered to be an increase in permeability

brought on by high porosity. On the scaffolds with bigger pores, fewer cells were observed at the onset of cell attachment. Larger pore diameters, however, allowed for faster oxygen and nutrient transfer, which ultimately encouraged the rapid growth of cells within the scaffolds. The balance between the scaffolds' surface area and permeability can also be used to maximize the top limit of cell density, as has been demonstrated.

1.2.4 Tuneable stiffness

For mechanobiological research in a range of mechanical conditions, scaffold stiffness manipulation is crucial. Even though changing the composition or design of conventional materials allows for easy tuning of stiffness, doing so would eventually alter other mechanical properties of the scaffolds, such as porosity. It is challenging to independently evaluate how mechanical stiffness affects cellular activities. Metamaterial scaffolds' stiffness can be changed without compromising other properties by changing their microscopic geometries. For instance, TPP was used to accurately print 3D nanolattice scaffolds made of tetrakaidekahedral unit cells, also known as Kelvin foam by Maggi *et al.* [33]. In this study, in order to give the scaffolds varying stiffness ranging from 0.7 MPa to 100 MPa but the same pore size, the struts' radius and hollowness of individual units were changed. On the most flexible nanolattice, osteoblast-like cells produced more intracellular F-actin and minerals than those on the stiffer scaffolds. Based on these findings, a model was developed to explain how scaffold stiffness and actin concentration relate to one another. By using this model, the scaffold stiffness could be further optimized for maximum actin synthesis and bone cell proliferation.

The design of TPMS sheet scaffolds with three distinct cellular geometries—primitive, gyroid, and diamond—with determined porosity, Young's modulus, and pore diameters was done using a parametric optimization method in order to produce metamaterial scaffolds that meet the needs of various tissue engineering applications by Vijayavenkataraman *et al.* [48]. The authors have tailored the cellular dimensions of metamaterial scaffolds to fit with a variety of soft and hard tissues based on the report of tissue-specific mechanical characteristics. By combining two basic materials with distinct Young's moduli, this optimization technique may also be used to create novel scaffolds with non-uniform mechanical characteristics. The mechanical heterogeneity may influence the differentiation of stem cells cultivated on the scaffolds into various lineages. The structural gradient found in biological tissues, such as the zonal cartilage, may also be replicated by stacking primitive, gyroid, and diamond structures in a particular arrangement or by mixing primitive structures with different cellular dimensions.

In another study, primitive sheet and gyroid Pneumatic melt extrusion was used to precisely design and print TPMS and cubic scaffolds after overcoming several production obstacles such determining the best print and material parameters for optimum pore development, reducing strand residue puller, and maximizing layer height. Afterwards, the scaffolds were seeded with osteoblasts, and Alamar blue and SEM images of the samples provided significant evidence of both the mechanical and biochemical compatibility, demonstrating the ability of melt extrusion printing to accurately create porous TPMS structures that serve as an ideal biomimetic niche for bone formation [49].

1.2.5 Other applications

Because of their distinctive deformations, mechanical metamaterials can also be employed to build artery or oesophageal stents [36], [50], [51]. For example, Ali *et al.* created an auxetic and biocompatible polypropylene film based on rotating-squares shape that could be wrapped around a cylindrical rod to produce a tubular stent. This might be employed for palliative treatment of oesophageal cancer and dysphagia prevention by expanding the tubular stent due to its auxetic properties[36]. Similarly, Gatt *et al.* developed a second-order hierarchical stent derived from rotating-squares shape that might increase the magnitude of Poisson's ratio, lowering inflammation owing to decreased contact area. The hierarchical design may also be employed in skin grafts due to the reduced pressure on the swollen region [52]. A rationally designed hip implant that combines auxetic (negative Poisson's ratio) and traditional honeycomb (positive Poisson's ratio) structures is one of the most recent advancements. Its goal is to reduce the likelihood of a bone implant interface failure by lowering the possibility of wear particles entering the enclosed space and mechanically stimulating bone growth to improve fixation [53]. They 3D printed these hybrid meta-implants with biomedical-grade titanium alloy Ti6Al4V-ELI using SLM. The implant is built in such a manner that when mechanical loading occurs, the region with a positive Poisson's ratio compresses, causing the region with auxetic structures to expand. This compresses the surrounding bone along both implant contact lines, preventing wear particles from entering the interface and stimulating bone development. These studies show the promise of architected cellular materials in synthesizing structured biomaterials with appropriate mechanical characteristics and topology to offer a suitable environment for cell development, enabling for the creation of more effective and safer prostheses.

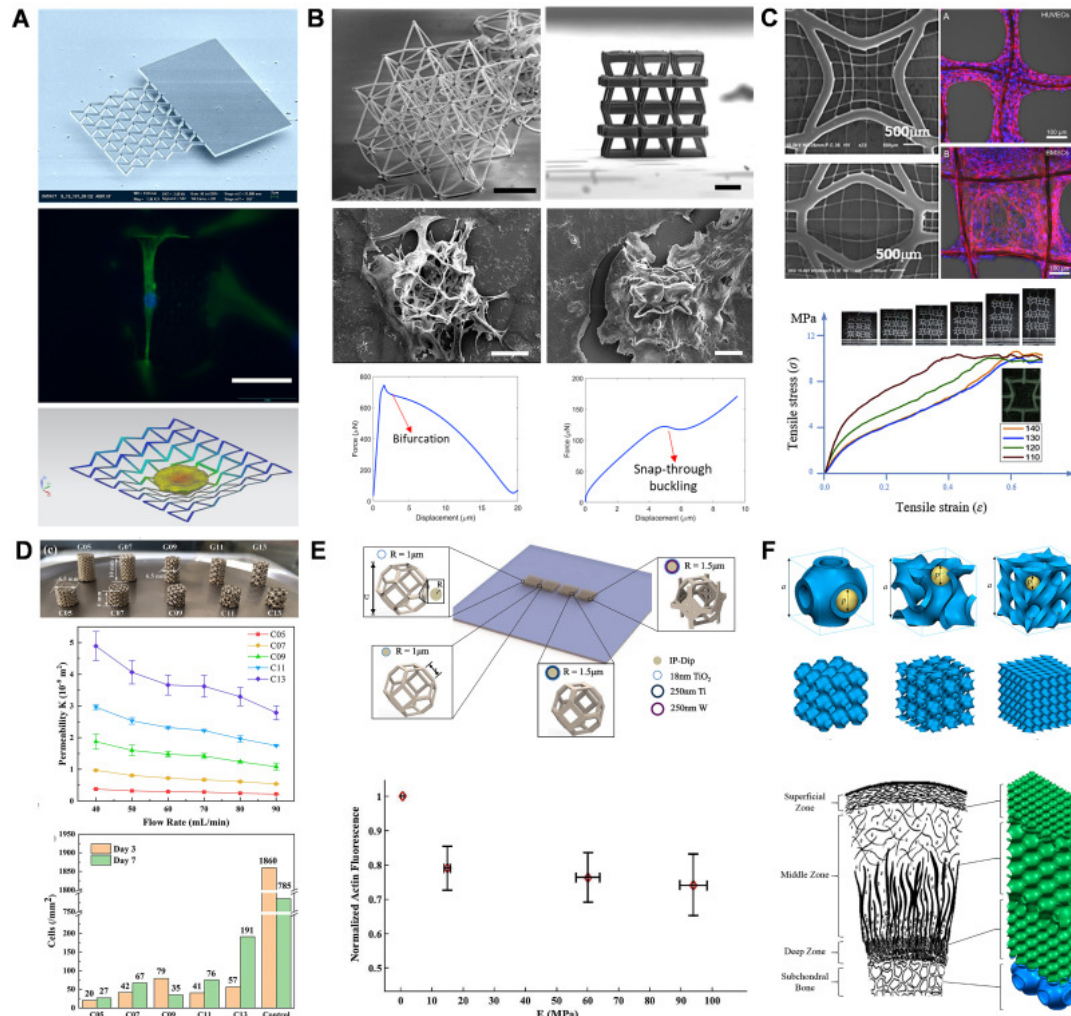


Figure 2. Different mechanical metamaterial and their applications in tissue engineering. **A)** By using deep reactive ion etching, Auxetic cantilevers with nanoscopic precision were created. When MSCs connected, they displayed a change in resonant frequency. **B)** Under the mechanical pressure of mesenchymal *Stem Cells*, octet truss and auxetic lattices displayed various deformation patterns. **C)** MEW *technique* made it possible to create auxetic webs with adjustable Poisson's ratio by weaving together thick and thin threads. Vascular endothelial cells encircled the thin fibers while bone marrow stem cells filled the wide spaces between them. **D)** Higher porosity and permeability gyroid lattices prevented the initial adherence of human cancer cells but encouraged cell growth after seven days. **E)** Tetrakaidekahedral units' strut radius and hollowness might be altered to provide a wide variety of stiffness values while maintaining a consistent pore size. A phenomenological model was created based on the correlation between f-actin expression and scaffold stiffness to direct future bone scaffold design. **F)** To facilitate the creation of TPMS metamaterial scaffolds that are more comparable to biological tissues, a parametric optimization approach that takes into account several mechanical characteristics was developed. Figure used with permission from [54].

1.3 4D bioprinting advances

4D bioprinting is the next-gen application of externally stimulating materials into TE. One example of shape change achieved by so-called 4D printing is the employment of stimuli

to trigger the spontaneous creation of a tube. Nature inspired this notion, which was then applied to shape-memory polymers [55]–[59].

Table 2 shows a range of 4D printing processes that are based on a specific environmental input. The fourth dimension in 4D bioprinting is sometimes misunderstood as tissue construct maturation [60]. It is the stimuli-based rearrangement that differentiates 4D printing and distinguishes it from the typical tissue maturation observed inside TE for decades [61]. Gladman *et al.* created a composite bioink that allows them to manage the elastic and swelling anisotropies by shear-induced alignment of cellulose fibrils inside a soft acrylamide matrix, inspired by the morphological reaction of plants to changes in humidity or light levels. This method replicates the directional orientation of cellulose fibrils in plant cell walls, resulting in a variety of local swelling behaviours. It was demonstrated that the expected and targeted biomimetic shape transition may be accomplished simply by experimenting with alternative laydown patterns that include variations in filament size, orientation, and spacing [62].

Kim *et al.* created a multi-cellular trachea tissue out of photopolymerizable silk fibroin bioink using 4D bioprinting based on digital light processing (DLP). By adjusting the shape (external condition) along with the composition (internal condition) of the printed hydrogels, they were able to accomplish anisotropic swelling. The bi-layered constructions, which included a base layer of human turbinate-derived stem cells and a patterned layer of human chondrocytes, demonstrated a 2-week in vitro shape change from a sheet-like structure to a hollow tube. Furthermore, 8 weeks after implantation into rabbits' injured tracheas, neo-cartilage development and a freshly created respiratory epithelial layer were seen [63].

Constante *et al.* expanded on the 4D printing strategy by combining two materials produced using separate manufacturing processes, 3D extrusion printing and MEW, to regulate the orientation of myoblasts on the tube inner wall via surface patterning. [67] Alignment is important in the directed contraction of muscle fiber bundles formed by the development of myoblasts into myotubes. Matrixes that facilitate cell alignment and 3D organization are required to replicate the natural ECM and construct anisotropic tissue architectures. Prior to shape transformation, a self-folding bilayer comprising printed methacrylated alginate with an inter-fiber spacing of 500 μm and melt electrowritten PCL fibers with a distance of 100 μm was seeded with cells. Variations in the elastic modulus of the hydrogel may be achieved depending on the crosslinking duration and photo-initiator concentration, resulting in changes in tube diameter. However, the inhomogeneous swelling was induced by a crosslinking gradient, with the top layer of the scaffold having a larger degree of crosslinking than the lower layers [64].

Living cell traction force has also been investigated as a driving mechanism for shape modification of flat geometrical shapes. This method is known as cell origami, and it is extremely biocompatible since external stimuli that are not generally seen in vivo may be avoided [65]. Nonetheless, a patterning material to which the cells can adhere is required, and top-down techniques have shown difficulties in terms of uniform cell distribution and density following seeding [66]. Modular assembly biomimetic design techniques, on the other hand, utilise cell sheets, spheroids, and tissue strands as building blocks rather than permanent exogeneous scaffolds.

Using metamaterials as a substrate for mechanobiology studies is still at a really early stage of development but can have already many promising results. The analysis of cell behaviors and responses on the metamaterials is not highly varied emphasizing the morphological characterization of cell shape, attachment, and proliferation. The biological investigations still focus on how macroscopic mechanical properties of the metamaterial scaffolds influence cell and tissue phenotypes but lack in-depth studies on how microscopic unit structures affect cell remodeling and molecular characterizations on cell metabolism, cytoskeleton organization, gene expression, and cell signaling will significantly advance the understanding of the complicated cell-material interactions [67].

Table 2. Materials for 4D printing with their fabrication methods and the external stimulus. Table used from [59].

External stimulus	3D architecture	4D architecture	Manufacturing technology	Shape transformation mechanism	Application
Hydration	Bilayers with different laydown pattern	Flower/plants	3D printer (ABG 10 000, Aerotech)	Changes in filament size, orientation, and spacing result in anisotropic swelling	Plant-inspired shapes
	Rectangular and square bilayer with base and patterned layer	Tube, flower	DLP	Different geometries and hydrogel compositions result in anisotropic swelling	Multi-cellular trachea mimetic tissue
	Double layer circular film (20 mm diameter with 0.5 mm spacing); MEW: printed on top of hydrogel; parallel deposited fibers with 0.1 mm spacing	Tube	3D extrusion printing and MEW	Anisotropic swelling caused by crosslinking gradient	Engineering of tissues with uniaxial cell orientation
	20 × 5 mm ² rectangular and parallel MEW fibers with 0.1 mm spacing	Scroll-like structure	3D printing and MEW	Shear-induced anisotropy	Muscle tissue regeneration
Temperature	3D honeycomb patterned hydrogel disc	Tube	Direct printing machine (Cellink BioX 3D printer)	Temperature dependent asymmetric swelling/shrinkage	Thermal actuators for soft robotics, active implantology; hollow tubes for biomedical engineering
Light	Bilayer helix	Complex shape	MPL	Anisotropic material density results in internal stress after plasmonic heating of gold nanorods	Adaptive bioinspired soft materials
Electric field	Gripper consisting of two beams; transporter consisting of hairs and a bridge; 3D printed human-like structure	Gripping an object; transporting an object; walking motion	DLP	Nonuniform swelling of electroactive hydrogels due to a concentration gradient of mobile cations caused by electric field	Soft robotic actuation; artificial muscle; TE
pH	Cylindrical tubes	Cylindrical tubes	Stereolithography (SLA)	Swelling and shrinkage as response to changes in the environmental pH	Scaffolds for TE
Ion concentration	Fibrous bilayer (PCL-poly(glycerol sebacate) and methacrylated hyaluronic acid)	Scroll-like structure	Electrospinning	Changes in bilayer thickness and medium counterion concentration result in different diameters (0.1–40 mm)	Artificial nerve graft

1.3.1 Metamaterials in bone tissue engineering

Bone tissue comprises a non-mineralized organic component and a mineralized inorganic component as a hierarchical structure spanning several size scales. Any osteogenic biomaterials or scaffolds must have exceptional compressive strength and excellent fracture toughness[50]. Metamaterials based on light-assisted and extrusion-based 3D bioprinting would allow for a wide range of structural options, from honeycomb to more complicated shapes. By combining biodegradable materials and inorganic phases, composite bioinks enable access to all 3D bioprinting modalities. Commercially available biodegradable bioinks, such as PCL-based materials, are emerging as promising candidates for the development of functional meta-biomaterials [68]. Metallic constructions can give a cost-effective justification for permanent implantation. The best alloys for bone implant applications include titanium, stainless steel, and cobalt chrome alloys. Metal 3D printing technology, however, is not currently capable of producing production-grade metal components with the dimensional precision required for such applications. We intend to do particular study on the use of biocompatible metals for

patient-specific implants. The main difficulties with metallic implants are surface roughness and interior defects caused by the sintering process. It is vital to enable high process stability by enhancing implant quality in order to fully exploit the potential of metallic metamaterials. The use of theoretical structures to increase the stability of implants minimizes their prices and the impact on patients' quality of life. Light-assisted AM is one strategy that may be utilized while taking temperature into account. A decreased energy density reduces the temperature gradient mechanism, and part quality may improve. The promise of SLM/SLS will be realized through broadening the material palette. In the case of wrought and cast goods, thermomechanical processing to establish precise microstructure-property-performance linkages is a potential approach for steel, aluminum alloy, and superalloy product development [69].

1.4 Light- assisted fabrication methods of Mechanical Metamaterials

One of the most straightforward ways of fabricating complicated mechanical metamaterials is through various light assisted methods which solidify photopolymerizable material by subjecting it to focused light beams while it is still liquid-like. Depending on the light wavelength, light excitation, and ink feeding method, the procedures may vary. Galvanometers or micro-mirror devices can be utilized to concentrate and guide the created light, whereas laser beams or collimated light sources are often employed for light creation. The material production process is then induced via vat polymerization, powder-bed fusion, or directed energy deposition processes. Stereolithography (SLA) and digital light processing (DLP)-based SLA have been suggested as sophisticated manufacturing technologies for polymers and plastics. The most advanced techniques currently used, are summarized in **Figure 3**.

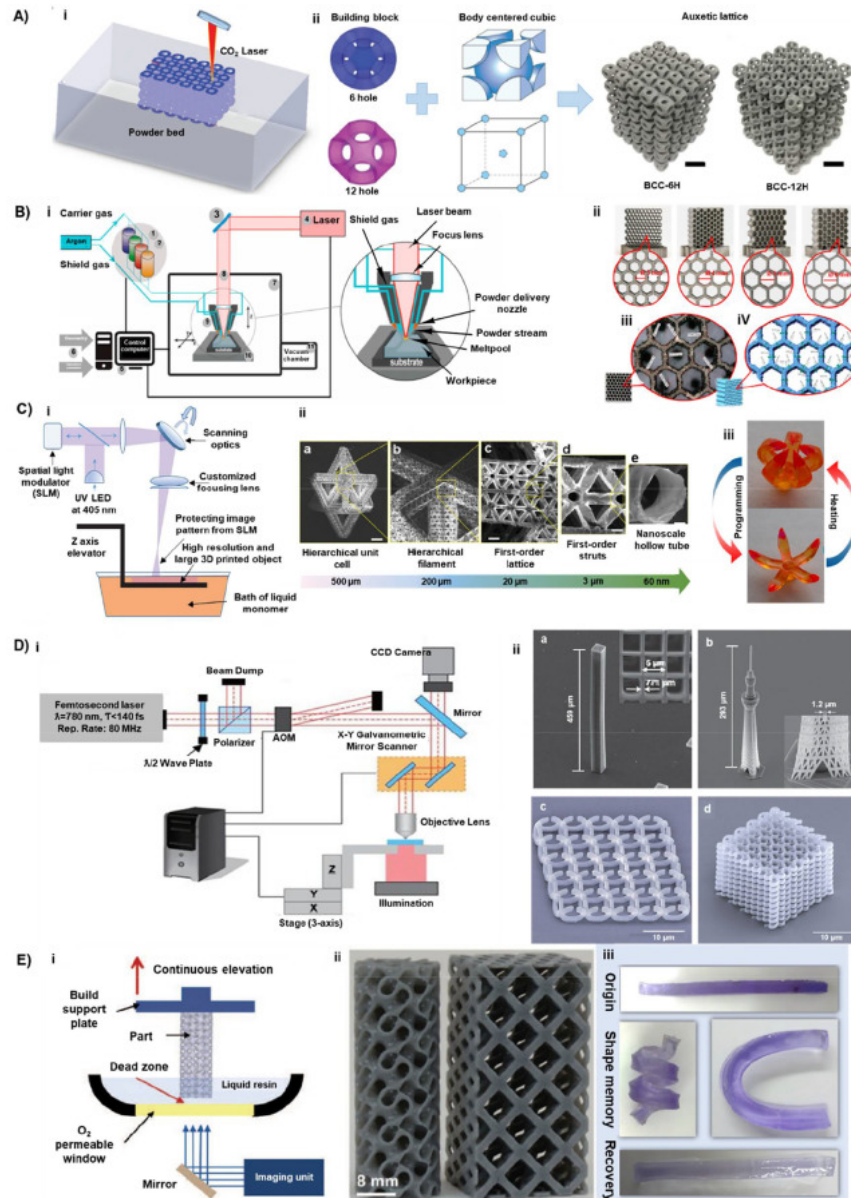


Figure 3. Schematic representation of Light assisted additive manufacturing techniques are currently used for the fabrication of metamaterials. **A)** Typical building platform for SLS and illustration of the concept of designs of BCC-6H and BCC-12H scaffolds [70]. **B)** Illustration of the LENS system, (ii) four variants of Ti6Al4V thin-walled honeycomb structures with different unit cell size, (iii) with the application of optical microscopy, and (iv) a 3D model. **C)** Schematic illustration of large area projection micro-stereolithography, (ii) (a-e) scanning electron microscopy images showing cross-section breakdown of structural hierarchy of the multi-scale metamaterial unit cell [16] and (iii) the demonstration of the transition between as printed shape and temporary shape of multi-material shape memory grippers [71]. **D)** (i) Schematic illustration of Two Photon Absorption, (ii) (a,b) scanning electron micrographs of 6 × 6 grid structure “Tokyo Skytree” fabricated by TPA with 100× microscope objective [72] , (c,d) a 3D split-ring metamaterial structure, fabricated using a metal-binding hybrid polymer composite. Figure used with permission from [6].

1.4.1 Multiphoton lithography

From the light assisted methods, multi-photon lithography (MPL) is amongst the most powerful 3D printing technique which enables the direct writing of computer-based designed geometries and structures within the volume of a photosensitive material [73], [74]. This technique was first demonstrated in 1997 [75], and it was used by the photonics fields community for the fabrication of a plethora of 3D structures such as mechanical metamaterials [37], [67], [76]–[78].

TPP is a potential approach for high-resolution 3D printing that can produce arbitrary and ultraprecise 3D structures with resolutions of less than 100 m (as low as 30 nm). Such structures may be micro/nanophotonics [79], microfluidics [80] drug delivery devices, transdermal needles [81], and bioimplants [82]. Photopolymerization may occur in any 3D spatial location in a substrate according to the CAD model, eliminating the need for supporting material in contrast to traditional SLA techniques, which confine polymerization to only the printing area's surface. Furthermore, the UV light used in SLA may cause photochemical damage to biological tissue, but the NIR spectrum light source utilized in TPA allows for the production of photopolymerized 3D structures in the presence of cells. This makes TPA an appealing approach for bioprinting drug-delivery systems, microelectromechanical systems (MEMs), and tissue engineering scaffolds [83].

1.5 Extrusion based

Extrusion-based technologies, in general, deposit a viscous paste-like ink layer by layer through an extruder nozzle. In the case of fused deposition modelling (FDM), the ink melts before passing through the nozzle and solidifies after being deposited onto a solid substrate or the previous layers. A thermally induced diffusion process bonds and welds the deposited layers. When compared to traditional techniques, this technology generates a selective layer-by-layer construction that provides greater design and production freedom. This section begins with extrusion-based approaches that employ single printheads before transitioning to multi-printhead systems. While light-assisted methods are appropriate for both metals and polymers, extrusion-based approaches are mostly applicable to polymer-based and polymer-metal composite metamaterials.

1.6 Future perspectives and issues

The use of metamaterials as a platform for mechanobiology research is still in its early stages. Only the morphological characterization of cell form, adhesion, and proliferation is highlighted in the investigation of cell behaviours and reactions on metamaterials. Biological research continues to focus on how the macroscopic mechanical characteristics of metamaterial scaffolds influence cell and tissue phenotypes, but, as shown above, there are few in-depth studies on how micro/nano unit structures influence cell remodelling. More molecular characterizations of cell metabolism, cytoskeleton organization, gene expression, and cell signalling would be extremely beneficial. Based on the broad and accurate metamaterial designs, we could increase our understanding of cell-material interactions. To increase the functionality of meta-implants, the design requirements for specific tissue types or disease states must be developed further. In addition to the geometric design, the material degradation profile, external triggers for shape alteration, and surface biofunctionalization should be considered when optimizing implants for minimally invasive delivery. Tissue integration enhancement is especially crucial for implants intended for long-term use, which necessitates a better mechanistic understanding of cell-material interactions based on in vitro metamaterial model systems.

1.7 Purpose of thesis and outline

Over the last few decades, the need for a biomimetic approach has emerged, which leads to fabricating scaffolds inspired by the nature. This study is no exception. One of the main inspirations was the hexagonal architecture found in the honeycomb, a design that has inspired numerous studies and structures, including the multi-billion NASA James Webb space telescope which aims to observe the most distant object in the cosmos [84]. This hexagonal architecture was used to design the tetrakaidekahedron structure, known as kelvin foam, and also the Auxetic bowtie structure. Through those two geometries two different mechanical environments were created, one ultra-stiff and one elastic derived from the same material.

The purpose of this thesis is first to fabricate the aforementioned structures to characterize their physicochemical properties and to study the cell responses to them. Second, this work aims to evaluate the effect of the mechanical properties of the scaffolds on the osteogenic differentiation potential of MSCs by monitoring Yap protein via confocal microscopy and Runx2 via both PCR and confocal microscopy. In order to use the confocal microscope in its all potential the development of a new non fluorescent material was crucial. Consequently, we

developed the SZ2080TM non fluorescent variant and a post- fabrication protocol that enabled us to have zero fluorescence background. In that way and by further optimizing 3D printing to rapidly fabricate large scaffolds, we tested the different mechanical environments towards osteogenic differentiation of MSCs.

This thesis follows the next outline:

- **Chapter 1** presents a general introduction in mechanical metamaterials in tissue engineering applications as well as the work that has been done concerning the different geometries that were fabricated, the different methods are used for the creation of those scaffolds and the tissues that those structures aimed for. Furthermore, the trend of 4D bioprinting is analyzed. The auxetic scaffolds were focused more as this is the main scaffold of this thesis and is one of the most important categories of mechanical metamaterials.
- In **Chapter 2**, all the theoretical background is going to be analyzed. More specifically, the theory behind two photon absorption and two photo polymerization as well as the parameters that affect the voxel size will be presented. Afterwards, the main mechanical characteristic of materials will be analyzed followed by the theory of biomaterials. Lastly, an extended analysis of mechanical forces and mechanotransduction sensing pathways inside the cells is presented alongside with a detailed analysis of the interaction between various key proteins.
- In **Chapter 3**, the experimental equipment used for the fabrication of the mechanical metamaterial scaffolds, the materials and the preparation processes of the cell seeding and culturing, as well as, the direct laser writing (DLW) protocol followed in this thesis will be presented.
- **Chapter 4** presents the experimental results starting with the theoretical mechanical simulations of the different scaffolds, followed by the optimization, fabrication, characterization and cell seeding of the first auxetic scaffolds. Then, the major drawback of autofluorescence is issued followed by the establishment of novel techniques and fabrication alterations to create large- autofluorescence free polymers for confocal microscopy. Lastly, by taking advantage of those scaffolds, the influence of auxetic environment on the osteogenic differentiation of MSCs is explored.
- **Chapter 5** presents the conclusion of this work and the future perspectives.

References

- [1] S. F. Badylak, “Xenogeneic extracellular matrix as a scaffold for tissue reconstruction,” *Transpl Immunol*, vol. 12, no. 3–4, pp. 367–377, 2004, doi: 10.1016/J.TRIM.2003.12.016.
- [2] D. M. Bissell and M. O. Choun, “The role of extracellular matrix in normal liver,” *Scand J Gastroenterol*, vol. 23, no. S151, pp. 1–7, 1988, doi: 10.3109/00365528809095908.
- [3] U. Hersel, C. Dahmen, and H. Kessler, “RGD modified polymers: Biomaterials for stimulated cell adhesion and beyond,” *Biomaterials*, vol. 24, no. 24, pp. 4385–4415, 2003, doi: 10.1016/S0142-9612(03)00343-0.
- [4] M. E. Furth, A. Atala, and M. E. van Dyke, “Smart biomaterials design for tissue engineering and regenerative medicine,” *Biomaterials*, vol. 28, no. 34, pp. 5068–5073, Dec. 2007, doi: 10.1016/j.biomaterials.2007.07.042.
- [5] G. F. Muschler, C. Nakamoto, and L. G. Griffith, “Engineering principles of clinical cell-based tissue engineering,” *J Bone Joint Surg Am*, vol. 86, no. 7, pp. 1541–1558, 2004, doi: 10.2106/00004623-200407000-00029.
- [6] E. Dogan, A. Bhusal, B. Cecen, and A. K. Miri, “3D Printing metamaterials towards tissue engineering,” *Appl Mater Today*, vol. 20, p. 100752, Sep. 2020, doi: 10.1016/J.APMT.2020.100752.
- [7] M. I. Echeverria Molina, K. G. Malollari, and K. Komvopoulos, “Design Challenges in Polymeric Scaffolds for Tissue Engineering,” *Front Bioeng Biotechnol*, vol. 9, p. 231, Jun. 2021, doi: 10.3389/FBIOE.2021.617141/XML/NLM.
- [8] A. Sharaf, B. Roos, R. Timmerman, G.-J. Kremers, J. J. Bajramovic, and A. Accardo, “Two-Photon Polymerization of 2.5D and 3D Microstructures Fostering a Ramified Resting Phenotype in Primary Microglia,” *Front Bioeng Biotechnol*, vol. 0, p. 1105, Jul. 2022, doi: 10.3389/FBIOE.2022.926642.
- [9] A. A. Zadpoor, “Meta-biomaterials,” *Biomater Sci*, vol. 8, no. 1, pp. 18–38, Jan. 2020, doi: 10.1039/C9BM01247H.
- [10] M. Wegener, “Metamaterials beyond optics,” *Science (1979)*, vol. 342, no. 6161, pp. 939–940, Nov. 2013, doi: 10.1126/SCIENCE.1246545/ASSET/78039256-3B42-486D-B670-F8614B01CE5B/ASSETS/GRAPHIC/342_939_F1.JPEG.
- [11] T. Bückmann *et al.*, “Tailored 3D mechanical metamaterials made by dip-in direct-laser-writing optical lithography,” *Advanced Materials*, vol. 24, no. 20, pp. 2710–2714, 2012, doi: 10.1002/adma.201200584.
- [12] L. D. Harris, B.-S. Kim, and D. J. Mooney, “Open pore biodegradable matrices formed with gas foaming,” 1998, doi: 10.1002/(SICI)1097-4636(19981205)42:3.

- [13] C. Y. Lin, N. Kikuchi, and S. J. Hollister, “A novel method for biomaterial scaffold internal architecture design to match bone elastic properties with desired porosity,” *J Biomech*, vol. 37, no. 5, pp. 623–636, May 2004, doi: 10.1016/J.JBIOMECH.2003.09.029.
- [14] V. J. Chen and P. X. Ma, “Nano-fibrous poly(l-lactic acid) scaffolds with interconnected spherical macropores,” *Biomaterials*, vol. 25, no. 11, pp. 2065–2073, May 2004, doi: 10.1016/J.BIOMATERIALS.2003.08.058.
- [15] S. Amin Yavari *et al.*, “Relationship between unit cell type and porosity and the fatigue behavior of selective laser melted meta-biomaterials,” *J Mech Behav Biomed Mater*, vol. 43, pp. 91–100, Mar. 2015, doi: 10.1016/J.JMBBM.2014.12.015.
- [16] X. Zheng *et al.*, “Multiscale metallic metamaterials,” *Nature Materials* 2016 15:10, vol. 15, no. 10, pp. 1100–1106, Jul. 2016, doi: 10.1038/nmat4694.
- [17] T. Jungst, W. Smolan, K. Schacht, T. Scheibel, and J. Groll, “Strategies and Molecular Design Criteria for 3D Printable Hydrogels,” *Chem Rev*, vol. 116, no. 3, pp. 1496–1539, Feb. 2016, doi: 10.1021/ACS.CHEMREV.5B00303.
- [18] C. Thamm, E. DeSimone, and T. Scheibel, “Characterization of Hydrogels Made of a Novel Spider Silk Protein eMaSp1s and Evaluation for 3D Printing,” *Macromol Biosci*, vol. 17, no. 11, Nov. 2017, doi: 10.1002/mabi.201700141.
- [19] D. F. D. Campos *et al.*, “The stiffness and structure of three-dimensional printed hydrogels direct the differentiation of mesenchymal stromal cells toward adipogenic and osteogenic lineages,” *Tissue Eng Part A*, vol. 21, no. 3–4, pp. 740–756, Feb. 2015, doi: 10.1089/ten.tea.2014.0231.
- [20] H. Y. Wang and Y. Q. Zhang, “Processing silk hydrogel and its applications in biomedical materials,” *Biotechnol Prog*, vol. 31, no. 3, pp. 630–640, May 2015, doi: 10.1002/btpr.2058.
- [21] S. R. MacEwan and A. Chilkoti, “Elastin-like polypeptides: biomedical applications of tunable biopolymers,” *Biopolymers*, vol. 94, no. 1, pp. 60–77, 2010, doi: 10.1002/bip.21327.
- [22] “Essentials of 3D Biofabrication and Translation - Anthony Atala, James J Yoo - Google Books.”
https://books.google.gr/books?hl=en&lr=&id=6uKcBAAQBAJ&oi=fnd&pg=PP1&ots=YwYL7TeHfK&sig=4b2zDG2UUyE3B2GLiGrAe4bMGOQ&redir_esc=y#v=onepage&q&f=false
 se (accessed Aug. 28, 2022).
- [23] X. Zhang, X. Chen, H. Hong, R. Hu, J. Liu, and C. Liu, “Decellularized extracellular matrix scaffolds: Recent trends and emerging strategies in tissue engineering,” *Bioact Mater*, vol. 10, pp. 15–31, Apr. 2022, doi: 10.1016/J.BIOACTMAT.2021.09.014.

- [24] F. Pati *et al.*, “Printing three-dimensional tissue analogues with decellularized extracellular matrix bioink,” *Nat Commun*, vol. 5, Jun. 2014, doi: 10.1038/NCOMMS4935.
- [25] W. Zhang, P. Soman, K. Meggs, X. Qu, and S. Chen, “Tuning the poisson’s ratio of biomaterials for investigating cellular response,” *Adv Funct Mater*, vol. 23, no. 25, pp. 3226–3232, Jul. 2013, doi: 10.1002/ADFM.201202666.
- [26] A. D. Lantada, A. Muslija, and J. P. Garcia-Ruiz, “Auxetic tissue engineering scaffolds with nanometric features and resonances in the megahertz range,” *Smart Mater Struct*, vol. 24, no. 5, p. 055013, Apr. 2015, doi: 10.1088/0964-1726/24/5/055013.
- [27] M. R. Gullo, S. Takeuchi, and O. Paul, “Muscle-actuated bio-hybrid mems by cell culture and differentiation on me tamaterial micro-scaffolds,” *Proceedings of the IEEE International Conference on Micro Electro Mechanical Systems (MEMS)*, vol. 2016-February, pp. 721–724, Feb. 2016, doi: 10.1109/MEMSYS.2016.7421729.
- [28] G. Flamourakis *et al.*, “Laser-made 3D Auxetic Metamaterial Scaffolds for Tissue Engineering Applications,” *Macromol Mater Eng*, vol. 2000238, p. 10.1002/mame.202000238, 2020, doi: 10.1002/mame.202000238.
- [29] C. Wang, Z. Vangelatos, T. Winston, S. Sun, C. P. Grigoropoulos, and Z. Ma, “Remodeling of Architected Mesenchymal Microtissues Generated on Mechanical Metamaterials,” <https://home.liebertpub.com/3dp>, Dec. 2021, doi: 10.1089/3DP.2021.0091.
- [30] M. Kapnisi *et al.*, “Auxetic Cardiac Patches with Tunable Mechanical and Conductive Properties toward Treating Myocardial Infarction,” *Adv Funct Mater*, vol. 28, no. 21, p. 1800618, May 2018, doi: 10.1002/ADFM.201800618.
- [31] Y. W. Chen, K. Wang, C. C. Ho, C. T. Kao, H. Y. Ng, and M. Y. Shie, “Cyclic tensile stimulation enrichment of Schwann cell-laden auxetic hydrogel scaffolds towards peripheral nerve tissue engineering,” *Mater Des*, vol. 195, p. 108982, Oct. 2020, doi: 10.1016/J.MATDES.2020.108982.
- [32] H. Wang, K. Su, L. Su, P. Liang, P. Ji, and C. Wang, “The effect of 3D-printed Ti6Al4V scaffolds with various macropore structures on osteointegration and osteogenesis: A biomechanical evaluation,” *J Mech Behav Biomed Mater*, vol. 88, pp. 488–496, Dec. 2018, doi: 10.1016/J.JMBBM.2018.08.049.
- [33] A. Maggi, H. Li, and J. R. Greer, “Three-dimensional nano-architected scaffolds with tunable stiffness for efficient bone tissue growth,” *Acta Biomater*, vol. 63, pp. 294–305, Nov. 2017, doi: 10.1016/j.actbio.2017.09.007.
- [34] S. Ma *et al.*, “Manufacturability, Mechanical Properties, Mass-Transport Properties and Biocompatibility of Triply Periodic Minimal Surface (TPMS) Porous Scaffolds Fabricated by

- Selective Laser Melting,” *Mater Des*, vol. 195, p. 109034, Oct. 2020, doi: 10.1016/J.MATDES.2020.109034.
- [35] M. Croes *et al.*, “A multifaceted biomimetic interface to improve the longevity of orthopedic implants,” *Acta Biomater*, vol. 110, pp. 266–279, Jul. 2020, doi: 10.1016/J.ACTBIO.2020.04.020.
- [36] K. Kuribayashi *et al.*, “Self-deployable origami stent grafts as a biomedical application of Ni-rich TiNi shape memory alloy foil,” *Materials Science and Engineering: A*, vol. 419, no. 1–2, pp. 131–137, Mar. 2006, doi: 10.1016/J.MSEA.2005.12.016.
- [37] G. Flamourakis *et al.*, “Laser-made 3D Auxetic Metamaterial Scaffolds for Tissue Engineering Applications,” *Macromol Mater Eng*, vol. 305, no. 7, pp. 1–9, 2020, doi: 10.1002/mame.202000238.
- [38] P. Mardling, A. Alderson, N. Jordan-Mahy, and C. L. Le Maitre, “The use of auxetic materials in tissue engineering,” *Biomater Sci*, vol. 8, no. 8, pp. 2074–2083, Apr. 2020, doi: 10.1039/C9BM01928F.
- [39] R. Critchley, I. Corni, J. A. Wharton, F. C. Walsh, R. J. K. Wood, and K. R. Stokes, “The preparation of auxetic foams by three-dimensional printing and their characteristics,” *Adv Eng Mater*, vol. 15, no. 10, pp. 980–985, Oct. 2013, doi: 10.1002/ADEM.201300030.
- [40] Y. Jin *et al.*, “Fabrication of multi-scale and tunable auxetic scaffolds for tissue engineering,” *Mater Des*, vol. 197, Jan. 2021, doi: 10.1016/J.MATDES.2020.109277.
- [41] M. Kapnisi *et al.*, “Auxetic Cardiac Patches with Tunable Mechanical and Conductive Properties toward Treating Myocardial Infarction,” *Adv Funct Mater*, vol. 28, no. 21, 2018, doi: 10.1002/adfm.201800618.
- [42] H. Haag, P. D. Dalton, and V. Bloemen, “The Synergy of Biomimetic Design Strategies for Tissue Constructs,” *Adv Funct Mater*, vol. 32, no. 32, p. 2201414, Aug. 2022, doi: 10.1002/ADFM.202201414.
- [43] X. Xin, L. Liu, Y. Liu, and J. Leng, “4D Printing Auxetic Metamaterials with Tunable, Programmable, and Reconfigurable Mechanical Properties,” *Adv Funct Mater*, vol. 30, no. 43, p. 2004226, Oct. 2020, doi: 10.1002/ADFM.202004226.
- [44] S. M. Ahmadi *et al.*, “Mechanical behavior of regular open-cell porous biomaterials made of diamond lattice unit cells,” *J Mech Behav Biomed Mater*, vol. 34, pp. 106–115, Jun. 2014, doi: 10.1016/J.JMBBM.2014.02.003.
- [45] H. M. A. Kolken *et al.*, “Additively manufactured space-filling meta-implants,” *Acta Biomater*, vol. 125, pp. 345–357, Apr. 2021, doi: 10.1016/J.ACTBIO.2021.02.020.

- [46] A. Pressley, “Gauss’s Theorema Egregium,” pp. 229–246, 2001, doi: 10.1007/978-1-4471-3696-5_10.
- [47] O. Al-Ketan, R. Rezgui, R. Rowshan, H. Du, N. X. Fang, and R. K. Abu Al-Rub, “Microarchitected Stretching-Dominated Mechanical Metamaterials with Minimal Surface Topologies,” *Adv Eng Mater*, vol. 20, no. 9, p. 1800029, Sep. 2018, doi: 10.1002/ADEM.201800029.
- [48] S. Vijayavenkataraman, L. Zhang, S. Zhang, J. Y. H. Fuh, and W. F. Lu, “Triply periodic minimal surfaces sheet scaffolds for tissue engineering applications: An optimization approach toward biomimetic scaffold design,” *ACS Appl Bio Mater*, vol. 1, no. 2, pp. 259–269, Aug. 2018, doi: 10.1021/ACSABM.8B00052/ASSET/IMAGES/MEDIUM/MT-2018-000523_0008.GIF.
- [49] N. S. al Hashimi, S. S. Soman, M. Govindharaj, and S. Vijayavenkataraman, “3D printing of complex architected metamaterial structures by simple material extrusion for bone tissue engineering,” *Mater Today Commun*, vol. 31, p. 103382, Jun. 2022, doi: 10.1016/J.MTCOMM.2022.103382.
- [50] A. K. Miri *et al.*, “Ectopic bone formation in rapidly fabricated acellular injectable dense collagen-Bioglass hybrid scaffolds via gel aspiration-ejection,” *Biomaterials*, vol. 85, pp. 128–141, Apr. 2016, doi: 10.1016/J.BIOMATERIALS.2016.01.047.
- [51] M. N. Ali and I. U. Rehman, “An Auxetic structure configured as oesophageal stent with potential to be used for palliative treatment of oesophageal cancer; Development and in vitro mechanical analysis,” *J Mater Sci Mater Med*, vol. 22, no. 11, pp. 2573–2581, Nov. 2011, doi: 10.1007/S10856-011-4436-Y/FIGURES/11.
- [52] R. Gatt *et al.*, “Hierarchical Auxetic Mechanical Metamaterials,” *Scientific Reports 2015 5:1*, vol. 5, no. 1, pp. 1–6, Feb. 2015, doi: 10.1038/srep08395.
- [53] H. M. A. Kolken, S. Janbaz, S. M. A. Leeftang, K. Lietaert, H. H. Weinans, and A. A. Zadpoor, “Rationally designed meta-implants: a combination of auxetic and conventional meta-biomaterials,” *Mater Horiz*, vol. 5, no. 1, pp. 28–35, Jan. 2018, doi: 10.1039/C7MH00699C.
- [54] C. Wang, Z. Vangelatos, C. P. Grigoropoulos, and Z. Ma, “Micro-engineered architected metamaterials for cell and tissue engineering,” *Mater Today Adv*, vol. 13, p. 100206, Mar. 2022, doi: 10.1016/J.MTADV.2022.100206.
- [55] X. Wan, L. Luo, Y. Liu, and J. Leng, “Direct Ink Writing Based 4D Printing of Materials and Their Applications,” *Advanced Science*, vol. 7, no. 16, p. 2001000, Aug. 2020, doi: 10.1002/ADVS.202001000.

- [56] S. Tibbits, “4D printing: Multi-material shape change,” *Architectural Design*, vol. 84, no. 1, pp. 116–121, Jan. 2014, doi: 10.1002/AD.1710.
- [57] M. Zarek, N. Mansour, S. Shapira, and D. Cohn, “4D Printing of Shape Memory-Based Personalized Endoluminal Medical Devices,” *Macromol Rapid Commun*, vol. 38, no. 2, Jan. 2017, doi: 10.1002/MARC.201600628.
- [58] S. Miao *et al.*, “Stereolithographic 4D Bioprinting of Multiresponsive Architectures for Neural Engineering,” *Adv Biosyst*, vol. 2, no. 9, Sep. 2018, doi: 10.1002/ADBI.201800101.
- [59] X. Kuang *et al.*, “Advances in 4D Printing: Materials and Applications,” *Adv Funct Mater*, vol. 29, no. 2, Jan. 2019, doi: 10.1002/ADFM.201805290.
- [60] S. v. Murphy, P. de Coppi, and A. Atala, “Opportunities and challenges of translational 3D bioprinting,” *Nature Biomedical Engineering 2019 4:4*, vol. 4, no. 4, pp. 370–380, Nov. 2019, doi: 10.1038/s41551-019-0471-7.
- [61] R. Langer and J. P. Vacanti, “Tissue Engineering,” *Science (1979)*, vol. 260, no. 5110, pp. 920–926, 1993, doi: 10.1126/SCIENCE.8493529.
- [62] A. Sydney Gladman, E. A. Matsumoto, R. G. Nuzzo, L. Mahadevan, and J. A. Lewis, “Biomimetic 4D printing,” *Nature Materials 2016 15:4*, vol. 15, no. 4, pp. 413–418, Jan. 2016, doi: 10.1038/nmat4544.
- [63] S. H. Kim *et al.*, “4D-bioprinted silk hydrogels for tissue engineering,” *Biomaterials*, vol. 260, p. 120281, Nov. 2020, doi: 10.1016/J.BIOMATERIALS.2020.120281.
- [64] J. Uribe-Gomez *et al.*, “Shape-Morphing Fibrous Hydrogel/Elastomer Bilayers Fabricated by a Combination of 3D Printing and Melt Electrowriting for Muscle Tissue Regeneration,” *ACS Appl Bio Mater*, vol. 4, no. 2, pp. 1720–1730, Feb. 2021, doi: 10.1021/ACSABM.0C01495/SUPPL_FILE/MT0C01495_SI_001.PDF.
- [65] K. Kuribayashi-Shigetomi, H. Onoe, and S. Takeuchi, “Cell Origami: Self-Folding of Three-Dimensional Cell-Laden Microstructures Driven by Cell Traction Force,” *PLoS One*, vol. 7, no. 12, p. e51085, Dec. 2012, doi: 10.1371/JOURNAL.PONE.0051085.
- [66] L. Ouyang, J. P. K. Armstrong, M. Salmeron-Sanchez, and M. M. Stevens, “Assembling Living Building Blocks to Engineer Complex Tissues,” *Adv Funct Mater*, vol. 30, no. 26, p. 1909009, Jun. 2020, doi: 10.1002/ADFM.201909009.
- [67] C. Wang, Z. Vangelatos, C. P. Grigoropoulos, and Z. Ma, “Micro-engineered architected metamaterials for cell and tissue engineering,” *Mater Today Adv*, vol. 13, Mar. 2022, doi: 10.1016/J.MTADV.2022.100206.
- [68] E. Dogan, A. Bhusal, B. Cecen, and A. K. Miri, “3D Printing metamaterials towards tissue engineering,” *Appl Mater Today*, vol. 20, Sep. 2020, doi: 10.1016/j.apmt.2020.100752.

- [69] Y. Huo *et al.*, “A Critical Review on the Design, Manufacturing and Assessment of the Bone Scaffold for Large Bone Defects,” *Front Bioeng Biotechnol*, vol. 9, Oct. 2021, doi: 10.3389/FBIOE.2021.753715/PDF.
- [70] B. Yuan *et al.*, “Machine-Learning-Based Monitoring of Laser Powder Bed Fusion,” *Adv Mater Technol*, vol. 3, no. 12, p. 1800136, Dec. 2018, doi: 10.1002/ADMT.201800136.
- [71] Q. Ge, A. H. Sakhaei, H. Lee, C. K. Dunn, N. X. Fang, and M. L. Dunn, “Multimaterial 4D Printing with Tailorable Shape Memory Polymers,” *Sci Rep*, vol. 6, Aug. 2016, doi: 10.1038/SREP31110.
- [72] K. Obata, A. El-Tamer, L. Koch, U. Hinze, and B. N. Chichkov, “High-aspect 3D two-photon polymerization structuring with widened objective working range (WOW-2PP),” *Light: Science & Applications 2013 2:12*, vol. 2, no. 12, pp. e116–e116, Dec. 2013, doi: 10.1038/lssa.2013.72.
- [73] M. Farsari, M. Vamvakaki, and B. N. Chichkov, “Multiphoton polymerization of hybrid materials,” *Journal of Optics*, vol. 12, no. 12, 2010, doi: 10.1088/2040-8978/12/12/124001.
- [74] Z. Vangelatos, V. Melissinaki, M. Farsari, K. Komvopoulos, and C. Grigoropoulos, “Intertwined microlattices greatly enhance the performance of mechanical metamaterials,” *Mathematics and Mechanics of Solids*, vol. 24, no. 8, pp. 2636–2648, 2019, doi: 10.1177/1081286519848041.
- [75] S. Maruo, O. Nakamura, and S. Kawata, “Three-dimensional microfabrication with two-photon-absorbed photopolymerization,” *Opt Lett*, vol. 22, no. 2, pp. 132–4, Jan. 1997.
- [76] Z. Vangelatos, V. Melissinaki, M. Farsari, and K. Komvopoulos, “In-growth of microlattices greatly enhances the performance of mechanical metamaterials,” pp. 1–18, 2018.
- [77] Z. Vangelatos, V. Melissinaki, M. Farsari, K. Komvopoulos, and C. Grigoropoulos, “Intertwined microlattices greatly enhance the performance of mechanical metamaterials,” *Mathematics and Mechanics of Solids*, vol. 24, no. 8, pp. 2636–2648, 2019, doi: 10.1177/1081286519848041.
- [78] Z. Vangelatos *et al.*, “Strength through defects: A novel Bayesian approach for the optimization of architected materials,” *Sci Adv*, vol. 7, no. 41, Oct. 2021, doi: 10.1126/SCIADV.ABK2218.
- [79] M. Farsari and B. N. Chichkov, “Two-photon fabrication,” *Nature Photonics 2009 3:8*, vol. 3, no. 8, pp. 450–452, Aug. 2009, doi: 10.1038/nphoton.2009.131.
- [80] J. Mačiulaitis *et al.*, “Preclinical study of SZ2080 material 3D microstructured scaffolds for cartilage tissue engineering made by femtosecond direct laser writing lithography,” *Biofabrication*, vol. 7, no. 1, 2015, doi: 10.1088/1758-5090/7/1/015015.

- [81] J. Torgersen, X. H. Qin, Z. Li, A. Ovsianikov, R. Liska, and J. Stampfl, “Hydrogels for Two-Photon Polymerization: A Toolbox for Mimicking the Extracellular Matrix,” *Adv Funct Mater*, vol. 23, no. 36, pp. 4542–4554, Sep. 2013, doi: 10.1002/ADFM.201203880.
- [82] M. A. Skylar-Scott *et al.*, “Guided Homing of Cells in Multi-Photon Microfabricated Bioscaffolds,” *Adv Healthc Mater*, vol. 5, no. 10, pp. 1233–1243, May 2016, doi: 10.1002/ADHM.201600082.
- [83] J. Torgersen, X. H. Qin, Z. Li, A. Ovsianikov, R. Liska, and J. Stampfl, “Hydrogels for Two-Photon Polymerization: A Toolbox for Mimicking the Extracellular Matrix,” *Adv Funct Mater*, vol. 23, no. 36, pp. 4542–4554, Sep. 2013, doi: 10.1002/ADFM.201203880.
- [84] J. Kalirai, “Scientific discovery with the James Webb Space Telescope,” <https://doi.org/10.1080/00107514.2018.1467648>, vol. 59, no. 3, pp. 251–290, Jul. 2018, doi: 10.1080/00107514.2018.1467648.

Chapter 2

2 Theoretical background

It is of great importance for one to study the theoretical analysis of the means and techniques that will be used during the experimental processes. Therefore, a consistent theoretical approach could be used either to predict the results of the experimental process, or alternatively, may be used in order to prove and explain the experimental results. Moreover, many times the theoretical models and simulations proved to be useful for understanding the underlying physical mechanisms of the experimental results.

Within the thesis, multi-photon polymerization was used to create mechanical metamaterial scaffolds that were then used to house the culture of cell lines such as MSCs and fibroblasts. Thus, in that chapter, the theoretical basis of materials and techniques that are required for those experiments will be presented.

2.1 Multiphoton absorption

The simultaneous absorption of two photons by the same molecule was first theoretically analyzed in the 1930s by Göppert-Mayer [1] one of the very few women to win the Nobel prize in Physics, and had to past 30 years to be proven experimentally in 1961 soon after the invention of the LASER technology. The further development of the ultrashort pulsed lasers made it possible to exploit this theory.

The main difference between one-photon absorption (1PA) and two-photon absorption (2PA) is that 2PA involves the simultaneous interaction of two photons, which increases with the square of the light intensity, whereas 1PA depends linearly on the intensity. This is why 2PP is only observed in intense laser beams, particularly focused pulsed lasers, which generate a very high photon density. Typically, 2PA is the way to reach a demanded excited energy state by using photons of half energy (which correspond to double the wavelength) instead of one photon transition.

Two-photon absorption (TPA) is a popular multiple-photon excitation approach to the initiation of photo-chemical changes. There are two different mechanisms of TPA: sequential and simultaneous two-photon excitation [2]. The sequential excitation involves the excitation of the absorbing species to a real intermediate state. This first excited state becomes populated

by the first absorbed photon and has a well-defined lifetime, typically 10^{-4} to 10^{-9} seconds. Then, a second photon is absorbed, as shown in **Figure 4.a, b** as well as the other mechanism. In this case there is no real intermediate state, but a virtual intermediate state is created by the interaction of the absorbing species with the first photon. Only if the second photon arrives within the virtual state lifetime, about 10^{-15} seconds, it can be absorbed. Therefore, in the second case higher intensities are required.

In case of single-photon absorption (**Figure 4.a**), the absorbing species is raised from the ground state (S_0) to an excited state (S_1) when it absorbs the energy of the single-photon, which is equal to $h\nu = E_1 - E_0$, where h is Planck's constant and ν the frequency of the incident light, while E_0 and E_1 are the energy levels ($E_0 < E_1$) of the absorbing species.

In the case of TPA, two photons, each with half energy of the gap between the two energy levels, namely $h\nu/2$, induce the electron transition. The most commonly lasers used for TPA are Ti: sapphire lasers because they produce ultrahigh peak power with a very short pulse width of approximately 100 femtoseconds (fs) or less. Furthermore, these lasers are very useful for TPP because of their central wavelength of approximately 800nm, which is close to half of the wavelength of the polymerization.

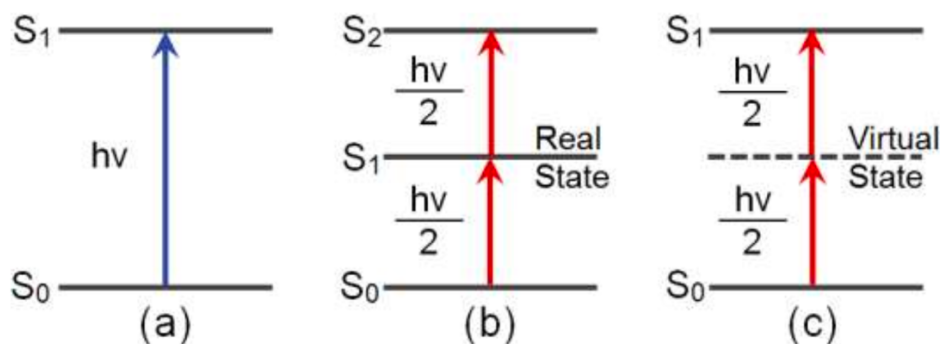


Figure 4. Schematic representation of the different excitation methods. A) Single photon excitation, b) Two photon sequential excitation c) Two photon simultaneous excitation.

2.2 Difference in the cross section of the focused spot in 1PA and 2PA

When a collimated laser beam is tightly focused with a high NA lens into a photo resin, photon-density profiles are made with a constant total number of photons at every cross-section in the focused spot. In **Figure 5** the photon density profiles of 1PA versus 2PA are shown. In case of 1PA, we see that along the optical axis of the focused laser beam the integration of the intensity remains the same through the whole volume, whereas in case of 2PA the highest intensity is reached only in the middle of the focal spot.

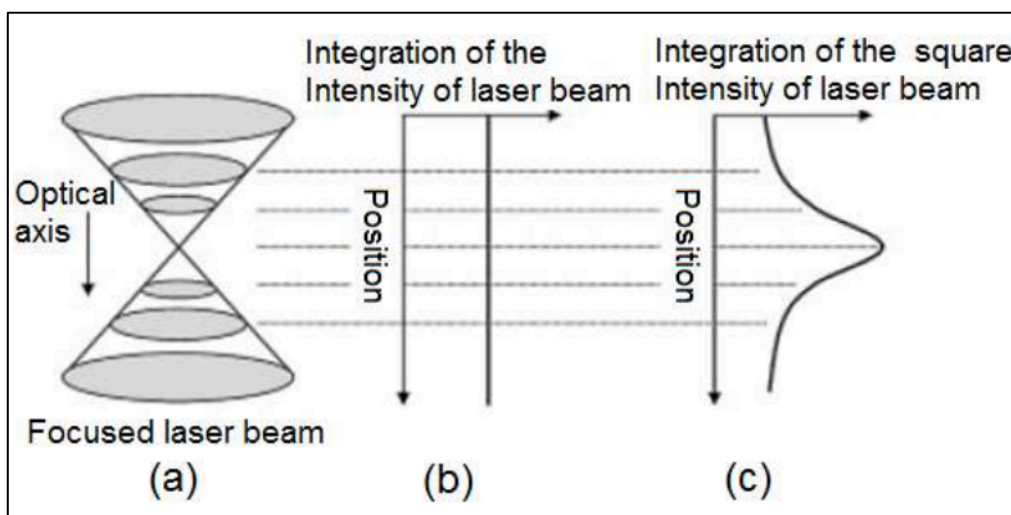


Figure 5. Comparison of TPA with single photon absorption generated by a tightly focused laser beam: (a) schematic diagram of focused laser beam; (b) total single photon absorption per transverse plane; (c) total two photon absorption per transverse plane, which is calculated by integrating the square intensity over the plane with respect to the optical axis. Figure used from [3].

2.3 The focal volume (voxel)

The voxel is the most important aspect of MPL and is defined as the pixel that a 3D structure has. A collimated beam of monochromatic light (for the multiphoton polymerization $\lambda=780\text{nm}$) of uniform intensity can be focused on a defined spot whose diameter is proportional to the wavelength and inversely proportional to the numerical aperture (NA) of the lens [4]. The excitation volume can be defined as the ellipsoid within which the excitation density is more than 50% at the center of the focus. The highest resolution (and thus the smallest excitation volume) available is provided to the users by commercially available oil-immersion objectives with a NA of 1.4. In such high NA, the width of the voxel at a wavelength of 800 nm is 0.29mm for 1 Photon Absorption and 0.21mm for 2PA. Unfortunately, the resolution is much poorer in the direction parallel to the beam: the length of the excitation volume is 1.08mm in the 1PA case and 0.78mm in the 2PA case. The ratio length/width of the excitation ellipsoid is 3.7:1; this ratio is a realistic lower limit, increasing sharply as the objective's NA decreases. That means that the voxel gets higher and higher by using objective lenses with lower magnifications (e.g., 40X, 20X, 10X, etc.) and lower NAs, losing all the resolution on the z-axis. As we can see in **Figure 6**, the excitation of a fluorescent dye (fluorescein) by 1Photon Absorption (1PA) (at 488 nm) generates a stream of emission along the beam path, whereas two Photon Absorption (2PA) (at 960 nm) gives a sharp point of emission at the focus volume

of the objective. 3D manipulating this very tightly defined voxel into a photo resin allows us to fabricate three-dimensional microscopic structures with sub-micrometer resolution. Other than microfabrication, 2PA is a convenient technique used in a plethora of applications such as 2PP microscopy [5], tracers, probes and sensors [6], photodynamic therapy [7] and even three-dimension optical storage [8].

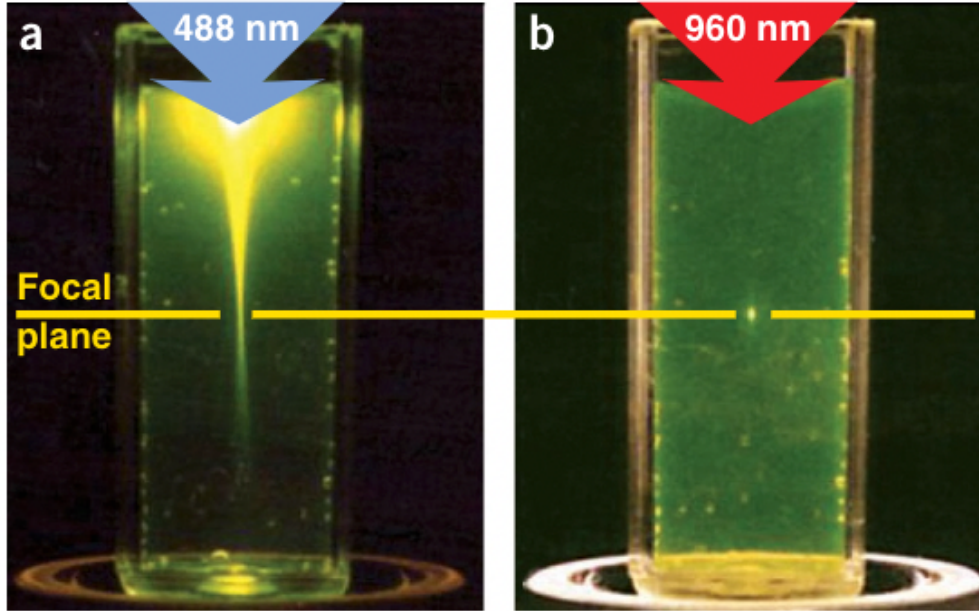


Figure 6. Localization of excitation by two-photon excitation. a) Single-photon fluorescein excitation by focused 488-nm light (0.16 NA). b) Two-photon excitation using focused (0.16 NA) femtosecond pulses of 960-nm light. Figure used from [4].

Typically, the smallest lateral size of the voxel for a commercial MPL system functioning at the 780 nm wavelength region is around 200 nm [9]. However, since the voxel is narrowed to an area within the focal point, reducing the wavelength can diminish the voxel's size. An evaluation of the voxel radius for NA values >0.7 has been proved to be [10]:

$$r_{xy} = \frac{0.32\lambda}{\sqrt{2}(NA)^{0.91}} \quad (1)$$

Where λ is the wave length and NA the Numerical aperture. This equation shows that the voxel diameter is right proportional to the wavelength of the incident radiation [11]. Previous work by Mueller et al. [12] demonstrated the development of an MPL setup operating at just 405 nm wavelength laser and achieving polymeric lines of just 68 nm.

The resolution of microstructures fabricated with TPP is determined by the size of the voxels (volumetric pixels). The intensity distribution of the laser beam (assumed to be Gaussian) can be expressed with the following equation (2) [13]:

$$I(r_0, 0) = I_0 \exp\left(-\frac{2r_0^2}{\omega_0^2}\right) \quad (2)$$

Where r_0 , I_0 and ω_0 are the radius of the beam, the beam intensity at the central axis in the focus plane, and the radius of the focused beam spot, respectively. Furthermore, the intensity profile along the optical axis can be expressed with equations (3) and (4) in terms of the amount of laser power (P_t) and by assuming that the geometry of the beam shape is given by a hyperbolic function (3) and (4):

$$I(r_z, z) = 2P_t/\pi\omega(z)^2 \exp[-2r_z^2/\omega(z)^2] \quad (3)$$

$$\omega(z) = \frac{\lambda}{\pi \tan\left[\sin^{-1}\left(\frac{NA}{n}\right)\right]} \sqrt{\left[1 + \left(\frac{\lambda z}{\pi \omega_0^2}\right)^2\right]} \quad (4)$$

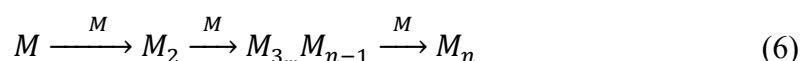
Where r_z , $\omega(z)$, λ , n , and NA are the coordinate along the radial axis of the beam, the radius of the focused beam along the optical axis (z), the wavelength, the index of refraction of the immersion oil, and the value of the numerical aperture, respectively. The density of radicals (r) produced by the femtosecond laser pulses in the polymerization process varies with the square of the beam intensity [14] and is given by the equation (5):

$$\frac{\partial p}{\partial t} = (\rho_0 - \rho)\delta \cdot I^2 \quad (5)$$

Where δ is the effective two-photon cross-section for the generation of radicals. These results show that a high spatial resolution can be achieved in the near threshold region of low laser power (<60 mW) and for short exposure times (<30 msec), and that the voxel length is more sensitive to the laser power than to the exposure time.

2.4 Multiphoton polymerization

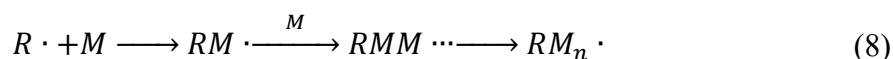
By taking advantage of the multiphoton absorption, we can use this technique to initiate the polymerization process through multiphoton polymerization. According to this technique, a femtosecond laser beam is tightly focused inside a photosensitive material that comprises from the photoinitiator, which will provide the material with the free radicals, the monomer, and, most of the time, a crosslinker. The basic components of the starting liquid material are monomers and oligomers. Upon light excitation, the monomers or oligomers may be solidified by two means: polymerization and crosslinking [15]. In photo-polymerization the formation of the polymeric chain is described from the equation:



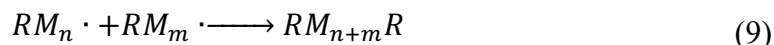
Here M is the monomer or oligomer unit, and M_n , the macromolecule containing n monomer units. The quantum yield of general monomers and oligomers is low. In order to increase the initiating efficiency, one or several low-weight molecules that are more sensitive to light irradiation are added. They form initiating species of radicals or cautions by absorbing photons. Such small molecules are called photo-initiators:



where I denote the photo-initiator, $R \cdot$ the free radicals and I^* an intermediate state of the photo-initiator after absorbing the photons. Therefore, the polymerization process is more precisely described by the succeeding equation:



The photo-produced radicals react with monomers or oligomers, producing monomer radicals, which combine with new monomers, and so on; so the monomer radicals expand in chain reaction, until two radicals meet with each other. This chain propagation stops in either of the following channels:



Typically, FRP consists of 4 fundamental processes: 1) **initiation**: the creation of the radical, 2) **growth**, the addition of monomers to the radical, 3) **termination**, the addition of two separate radicals to generate an inert polymer and 4) **transfer**, the termination of a polymer chain and the subsequent initiation of a new one. For a radical type initiator, benzoyl is the most widely used chromophore, which must have the initiator, since it exhibits good absorption in the UV region.

After polymerization, the oligomer constitutes the backbone of the polymer network. The physical, chemical and mechanical properties of the solidified resin in strictly depend on the nature and structure of the oligomer. Oligomers generally contain at least two reactive groups, from which both cross-linking and polymerization could occur.

In general, the MPL method depends on several parameters, summarized in **Table 3**.

Table 3. Parameters of MPL and their typical reported values [16].

Parameter	Value	Comments
λ	515, 800 and 1030 nm	400, 532 and 1064 nm are also possible
τ	10–325 fs	ps, ns and CW are also possible
R	1 kHz–100 MHz	Single pulse and GHz reported, too
v_v	100 $\mu\text{m/s}$ (10–10,000 $\mu\text{m/s}$)	Not relevant for projection/interference lithography
t_{exp}	10 μs –10 ms	0.1–10 s exposure can be applied in interference lithography
P_a	0.02–70 mW	More than 100 mW power can be applied in interference lithography
P_p	0.3–47 kW	Peak power per pulse is more important than the average
E_p	0.1–7 nJ	Lower than 0.1 nJ and higher than 7 nJ values can be observed
D	20 pJ–650 μJ	Accumulated dose of multiple individual pulses
NA	1.4 (1.35–1.45)	Only tight focusing or immersion oil objectives ($NA > 1.3$) are considered.
F^a	3 $\mu\text{J/cm}^2$ –21 kJ/cm^2	Accumulated exposure dose per area at the sample
I^a	0.2–7 TW/cm^2	>20 TW/cm^2 can be calculated, if assuming 100% objective transmittance
I_v^a	2–150 TW/cm^3	Towards considering the energy is absorbed within volume not at the surface
W_{abs}^b	80 pJ/cm^3 –0.3 mJ/cm^3	Absorbed energy density per single pulse

2.5 Two-step absorption instead of two-photon absorption

The quadratic optical nonlinearity arising from two-photon absorption delivers the vital spatial concentration of excitation in three-dimensional (3D) laser nanoprinting, with extensive applications in multiple fields. Femtosecond lasers allow for efficient two-photon absorption but are accompanied by several issues, including higher-order processes, cost, reliability, and size. A recent study has introduced a two-step absorption that replaces the two-photon absorption as the primary optical excitation procedure. Under proper circumstances, two-step absorption displays the same quadratic optical nonlinearity as two-photon absorption. A novel photoresist system was introduced based on a photoinitiator supporting two-step absorption, a scavenger, and a triacrylate. Therefore, this system allowed for printing 3D microstructures using $\sim 100\mu\text{W}$ power from a low-cost, compact continuous wave laser diode emitting at 405 nm. This work is essential as it paves the way for a drastic shrinking and cost decrease of 3D laser fabrication systems [17].

2.6 Stereolithography

Two-photon polymerization is an excellent method that enables the user to produce very high-resolution structure at a cost of long fabrication time and relatively small fabrication volumes and is ideal for studying basic cell biology [18], [19]. Other studies have utilized diffractive optic elements (DOEs) to split the laser beam into an array of 9 beams with lower power by rapid fabrication of 9 simultaneous unit cells achieving an astonishing $0.9 \cdot 10^7$ voxels/s writing speed [20]. Even if this fabrication speed is really fast, the handling of MPL fabricated scaffold is nearly impossible due to their relatively small size, fact that consist a major drawback in case those scaffolds need to get transplanted and handled by clinicians.

To overcome these drawbacks, attention has been drawn towards other printing methods such as one-photon polymerization, a powerful Stereolithographic (SLA) technique[21]. Commercial 3D printers oftentimes take advantage of this technique by utilizing an inverted UV lamp under a tank containing a UV curable resin. The platform is connected to a Z-axis, enabling the system movement during scaffold fabrication in a layer-by-layer manner[22]. The ease of use, the ability of large-scale scaffold fabrication and the affordability due to the advances in 3D printer technology, has allowed printers to find use in applications such as cell studies, tissue engineering, microfluidics, biotechnology and even teaching purposes[23], [24]. The use of such a system has been previously reported for the creation of Bioinks[25], [26].

Considering the aforementioned, the suitable printing method for scaffold fabrication should be selected attentively. The large gap between scaffold dimensions and the resolution of printing techniques is a serious consideration, especially in the case of grafts that are meant to be used as implants for tissue regeneration[27]–[29]. Large-scale scaffolds fabricated with 2PP exhibit high resolution but are challenging and time-consuming to fabricate, while scaffolds fabricated with 3D printers reach the necessary scale easily, but might lack the micro- or even nanometer resolution cell environments require.

2.7 Fluorescence mechanism

There are numerous types of luminescence that differ in how the system is stimulated, for example, electroluminescence is excited by an electric current, chemiluminescence is generated by a chemical process, and photoluminescence is excited by photons. Photoluminescence is further subdivided into fluorescence and phosphorescence. The primary distinction between fluorescence and phosphorescence is the duration of luminosity. When the light is turned off, the fluorescence stops immediately. Phosphorescence, on the other hand, might linger for hours after the excitation has stopped.

Because phosphorescing molecules may emit light for far longer periods of time than fluorochromes, there must be a variation in how they store excitation energy. The difference is due to the two types of excitation levels, singlet excited state and triplet excited state, which are based on differing spin alignments.

Spins are electron properties. In layman's words, the spin represents the electron's angular momentum created by spinning. The spin of an electron can be positive (+1/2) or negative (-1/2). Spin pairs of higher energy levels can be either parallel or antiparallel to one other. Individual angular momentums compensate for each other in antiparallel spin pairs, resulting in a total spin of zero. This spin alignment is referred to as a singlet state. Two parallel spins do not compensate and provide a result other than zero. In this instance, the spins are considered to be in a triplet condition.

When electrons return from a singlet excited state to the ground state, they fluoresce. However, in some molecules, the excited electrons' spins can be converted to a triplet form via a process known as inter system crossover. Until they reach the triplet ground state, these electrons lose energy. This state has more energy than the ground state but less energy than the singlet excited state. As a result, the electrons cannot readily return to the singlet state, nor can

they quickly return to the ground state, because quantum physics only allows total spins with a value of zero.

However, only a few transitions from the triplet ground state to the ground state are conceivable at any one moment. These modifications cause photon emission and phosphorescence. Because just a few events may occur at a time, the triplet ground state acts as an energy store, allowing phosphorescence to occur over a longer time period.

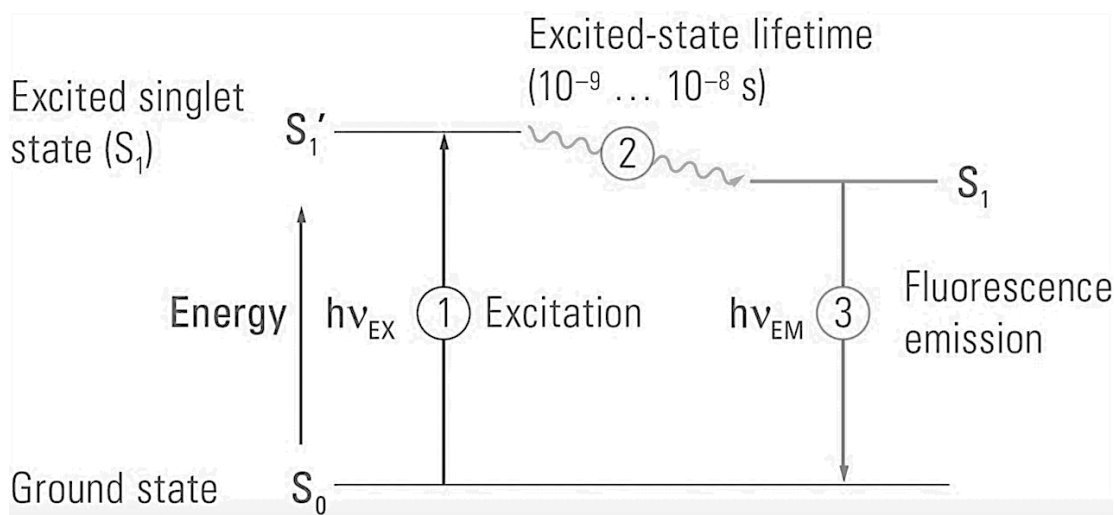


Figure 7. When light of a certain wavelength (excitation wavelength) hits a molecule (e.g. in a fluorophore) the photons are absorbed by electrons of the molecule. The electrons are subsequently elevated from their ground state (S_0) to a higher energy level, known as the excited state (S_1'). This is known as excitement (1). The excited-state lifespan is rather brief (usually 10^{-9} - 10^{-8} seconds), and part of the electron's energy is wasted during that period (2). The remaining energy taken up during excitation is lost as electrons leave the excited state (S_1) and return to the ground state (3). In the case of fluorophores, the energy is released as light (fluorescence emission) of a longer wavelength than the excitation light (and so with less energy). Stokes' shift is the name given to this phenomenon.

2.8 Materials for MPL

The materials (organic or composite) that are used nowadays in 3D structuring by MPL are similar to those employed in conventional lithographic applications. The system comprises two main components, the polymerizable material, which will produce the 3D structure, and a photoinitiator, which is a molecule that absorbs light and provides the active species which initiate the polymerization. To date, a large variety of polymeric and hybrid materials, as well as photoinitiators have been used in MPL. These are mostly negative photoresists, in which the light exposed area becomes polymerized or cross-linked to produce the solidified 3D structure, allowing the unexposed resist to be washed away in the development stage. Regardless of the

material being a negative or positive photoresist, it should fulfil the following requirements:

- (i) it should be transparent at the wavelength of the laser beam used for the 3D structuring, to allow the focusing of the laser within the volume of the material,
- (ii) it should possess a fast-curing speed to enable the structuring at a reasonable scanning speed
- (iii) after curing the material should present chemical and mechanical stability to produce robust and well-defined 3D structures.

In general, there are four main classes of materials used as negative photoresists in MPL, namely organic, renewable, hybrid, and functional materials.

2.8.1 Organics

This category is one of the most used and particularly the (methyl)acrylate monomers [30]. This monomeric class draws much attention as there is a great variety available, they are transparent in near- infrared wavelengths, rapidly photo- polymerized with low shrinkage and can be developed under most organic non aggressive solvents. Among the first organic materials used in MPL is SU-8. It is a negative tone photoresist comprising monomer units bearing eight epoxy groups as the bulk building material and a triaryl sulfonium salt as the photoacid generator (PAG) [31]. Another important class of organic materials used in MPL is the one based on hydrophilic monomers or polymers leading to the formation of hydrogels. A hydrogel is defined as a 3D network of hydrophilic polymers that can swell in water retaining a large amount of the solvent (>10%)[32]. Hydrogels possess a network structure with flexibility very similar to that of natural tissues, property that renders them particularly attractive for biomedical applications [33]. Among the most extensively studied hydrophilic polymers is poly(ethylene glycol) (PEG).

2.8.2 Hybrid materials

These hybrid organic-inorganic materials constitute an important class of materials in which both inorganic and organic structural elements co-exist in atomic or nanoscale dimensions. The inorganic part enhances the mechanical and thermal stability of the hybrid, modulates its refractive index, and contributes specific electronic, redox, electrochemical or chemical properties. On the other hand, the organic part provides the possibility to tune the mechanical properties, control the porosity and connectivity of the network, and confers specific chemical, physical or biological properties. Typical and most widely used hybrid materials for MPL are ORMOCER[®], OrmoComp[®], and SZ2080[™]. More precisely,

ORMOCERs (Organic Modified Ceramics) and OrmoComp have an inorganic silicon dioxide (SiO₂) backbone functionalized with acrylate or epoxide groups, which can be employed to cross-link the bulk resin material, with the use of a photoinitiator, into the solid 3D structures. On the other hand, SZ2080™ is a Zr based material. Besides those materials, other hybrids have been reported such as Titanium based [34], Vanadium based [35], and Germanium based [36].

2.9 Materials mechanical properties

A material's mechanical qualities determine how it performs when loaded. The elastic modulus of the material dictates how much it deflects under load, while the material's strength determines the stresses that it can sustain before failing. When a material is loaded above its elastic limit, its ductility plays an important part in deciding when it will shatter. Because every mechanical system experiences loads during operation, it is critical to comprehend how the materials that comprise such mechanical systems respond.

A material specimen is subjected to a tension or compression test to assess the connection between stress and strain in a material. A constantly rising axial force is supplied to a test specimen in this test, and the deflection is monitored as the load increases. A load-deflection curve may be drawn using these data. The deflection of the test specimen is determined by both the elastic modulus of the material and the geometry of the specimen (area and length). The stress and strain are given by the equations (11) and (12):

$$\text{Stress: } \sigma = \frac{P}{A_0} \quad (11)$$

$$\text{Strain: } \varepsilon = \frac{L - L_0}{L_0} \quad (12)$$

Where P is the load and A_0 is the cross-section area of the test specimen. In the strain equation, L is the current length of the specimen and L_0 the original length.

2.9.1 Stress- strain curve

The values of stress and strain determined from the tensile test can be plotted as a *stress-strain curve*, as shown in **Figure 8**:

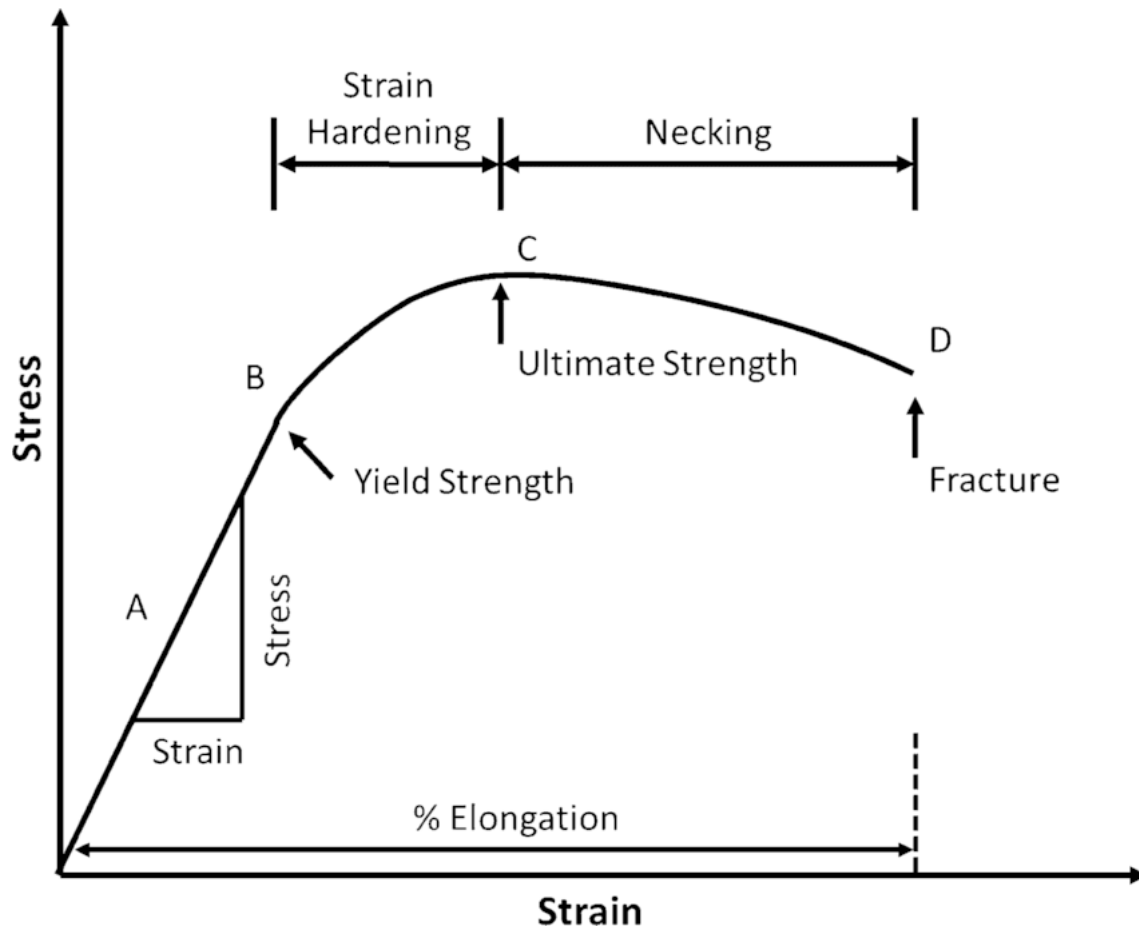


Figure 8. A typical stress- strain diagram of a material undergoing tensile strain testing. Figure used from [37].

As we can see from the diagram, there are several points of interest:

- A: This is the elastic limit, which denotes the greatest stress value for which no permanent set exists. Even if the curve between the proportionality limit and the elastic limit is not linear, the material is still elastic in this region, and removing the load at or below this point causes the specimen to return to its original length.
- B: This is the yield point, which defines the stress value over which the strain begins to quickly grow. The yield strength, S_{ty} , is the stress at the yield point. For materials lacking a well-defined yield point, the 0.2% offset approach is commonly used, in which a line parallel to the linear component of the curve is drawn and meets the x-axis at a strain value of 0.002. The yield point is the point at which the line crosses the stress-strain curve.

- C: On the stress-strain diagram, this point corresponds to the ultimate strength, σ_u , which is the greatest value of stress. Tensile strength is another name for ultimate strength. After achieving the ultimate stress, ductile material specimens will display necking, a reduction in cross-sectional area in a localized portion of the specimen.
- D: This is the fracture point or the break point, which is the point at which the material fails and separates into two pieces.

2.9.2 Hooke's law

The connection between stress and strain is linear below the proportionality limit of the stress-strain curve. The elastic modulus, E , is the slope of this linear part of the stress-strain curve. It is also known as the Young's modulus and the modulus of elasticity. Hooke's law, which is given by the equation (13) expresses the connection between the elastic modulus, stress, and strain in a material inside the linear area:

$$\sigma = E\varepsilon \quad (13)$$

Where σ is the value of stress and ε is the value of strain. Moreover, Hooke's law may be changed to form a relation between shear stress and strain according to the equation (14):

$$\tau = G\gamma \quad (14)$$

Where τ is the value of shear stress, γ the value of shear strain and G the value of shear modulus or elasticity. The elastic modulus and shear modulus are related by the equation (15):

$$G = \frac{E}{2(1 + \nu)} \quad (15)$$

Where ν is the Poisson's ratio. By definition, the Poisson's ratio of a material is calculated by the equations (16), (17) and (18):

$$\varepsilon_y = \frac{\Delta y}{y_0} \quad (16)$$

$$\varepsilon_x = \frac{\Delta x}{x_0} \quad (17)$$

$$\nu_{yx} = -\left(\frac{\varepsilon_x}{\varepsilon_y}\right) \quad (18)$$

Where ε_y is the axial strain, ε_x is the transverse strain and ν_{yx} is the ratio of those two.

2.10 Metamaterials

Metamaterial (from the Greek word μετά *meta*, meaning "beyond" and the Latin word *materia*, meaning "matter" or "material") is any material engineered to have a property that is not found in naturally occurring materials [38]. They are constructed from numerous pieces composed of composite materials such as metals and polymers. Typically, the materials are organized in repeating patterns at sizes smaller than the wavelengths of the phenomena they control. The characteristics of metamaterials are obtained not from the qualities of the basic materials, but from their uniquely constructed structures and architectures. Their precise shape, geometry, size, orientation and arrangement gives them their smart properties capable of manipulating not only electromagnetic waves but also mechanical properties: by blocking, enhancing, absorbing, or bending waves, to achieve benefits that go beyond what is possible with conventional materials.

One particular kind of metamaterials is mechanical metamaterials. Because of its critical relevance in real-life applications, mechanical characteristics of materials have been one of the most fundamental and frequently investigated fields in materials. For millennia, material development has depended primarily on changes in composition to affect mechanical qualities. The spectrum of available materials has expanded throughout time, allowing us to pick a more appropriate material for various purposes. [39]. However, there are often definite couplings between the inherent properties of these materials, such as the intimate coupling between strength and density, where high strength materials are generally high in density and vice versa.

On the other hand, numerous materials found in nature often exhibit intriguing properties unachievable with conventional materials [40]. These natural materials, particularly cellular materials, evolved over millions of years to establish an optimal design that could span several hierarchies over diverse length scales. [41]. For example, the extremely complex porous architecture of a bone core, which consists of intricately shaped ligaments and density gradients,

allows it to achieve significantly higher structural efficiency than most synthetic cellular materials developed by humans, which have considerably less elaborate architectures and are far from ideal [42]. Another well-known example of architectural exploitation is the comparison between the Great Pyramid of Giza with the Eiffel Tower. Due to its hierarchical and three-dimensional construction, the Eiffel Tower is almost twice as tall as the Great Pyramid of Giza yet has equivalent structural integrity and is nearly three orders of magnitude lighter.

2.11 Auxetic metamaterials

Auxetic mechanical metamaterials have a Negative Poisson Ratio (NPR) and exhibit an unexpected trait of lateral expansion when stretched, as well as equal and opposite densification when compressed. Evans created the term Auxetic in 1991, taken from the Greek word 'Auxetikos' (that which tends to grow) for materials that surpass negative Poisson's Ratio [43].

This particular category, mainly used for mechanical applications, constitute a particular group within the growing family of mechanical metamaterials. Pioneering studies in the field described the feasibility of materials with a negative Poisson ratio, presented examples of auxetic foams and polymers, described varied geometrical design principles, illustrated different design and manufacturing routes for creating auxetics, and proposed potential industrial applications in fields such as robotics, health, and transport [44].

Since research in this field began, auxetics have been considered for different biomedical applications, as some biological tissues have auxetic-like behavior [45], in addition to a lightweight structure and morphing properties, which makes auxetic geometry ideal for interacting with the human body.

2.12 Ultralight, Ultra-stiff mechanical metamaterials

Nature has evolved cellular structures, such as honeycomb[46] (wood, cork) and foamlike structures, such as trabecular bone[47], plant parenchyma[48], and sponge[49], to develop mechanically efficient materials that combine low weight with outstanding mechanical qualities. Lightweight balsa, for example, has a stiffness-to-weight ratio equivalent to steel in the axial stress direction[50]. Human-made lightweight cellular materials created from a diverse variety of solid elements, inspired by these naturally occurring cellular structures, are attractive for a wide range of applications, including structural components[51], [52], and biomaterials [53], [54].

However, the degradation in mechanical properties can be radical as density decreases [55]. A number of examples among recently reported low-density materials include graphene elastomers [56], metallic microlattices [57], [58], carbon nanotube foams [59], and silica aerogels [60]. For instance, the Young's modulus of low-density silica aerogels decreases to 10 kPa (0.00001% of bulk) at a density of less than 10 mg/cm³ (<0.5% of bulk).

Most natural and artificial cellular solids with irregular porosity, particularly at relative densities less than 0.1%, demonstrate a quadratic or greater scaling connection between Young's modulus and density, as well as between strength and density. $E/E_s (\rho/\rho_s)^n$ and $y/y_s (\rho/\rho_s)^n$, where E represents Young's modulus, density, yield strength, and s is the relevant bulk value of the solid constituent material property. The power n of the scaling relationship between relative material density and relative mechanical property is determined by the microarchitecture of the material. The cell walls and struts of conventional cellular foam materials with stochastic porosity are known to flex and deform primarily. With $n = 2$ or 3 , this sort of deformation leads in relative stiffness scaling. Several ways have been developed in recent years to minimize the connection between mechanical characteristics and mass density. [61], [62].

Few manufacturing techniques can create arbitrary three-dimensional microarchitectures with regulated micro- and nanostructures across a wide range of mass density and material components. The octet truss and the tetrakaidekahedron, commonly known as Kelvin foam, are two of the most well-known lightweight metamaterials. Both structures are hierarchical and are generated from a unit cell that is repeated in three dimensions to create the lattices [63].

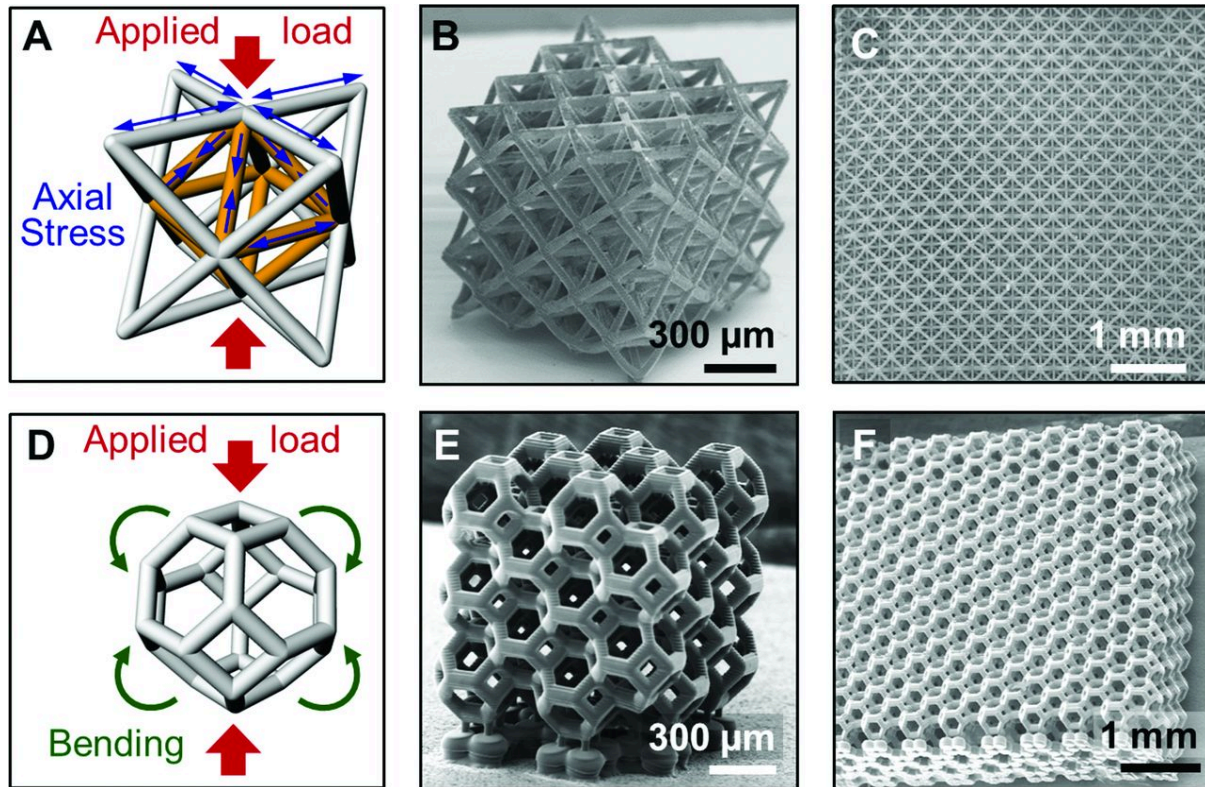


Figure 9. Architecture of octet truss and Kelvin foam. (A) Mechanical response to compressive loading of a stretch-dominated octet-truss unit cell. (B) Octet-truss unit cells packed into a cubic micro lattice. (C) SEM image of a stretch-dominated lattice material composed of a network of octet-truss unit cells. (D) Mechanical response to compressive loading of a bend-dominated tetrakaidecahedron unit cell. (E) Tetrakaidecahedron unit cell packed into a cubic bend-dominated lattice (Kelvin foam). (F) SEM image of a bend-dominated lattice composed of a network of tetrakaidecahedron unit cells. Figure used with permission from [63].

2.13 Tissue Engineering

The goal of tissue engineering is to generate tissue and organ replacements that can preserve, restore, or increase the functions of wounded or sick counterparts of the organism in vivo. However, there are numerous limitations, including a scarcity of immunologically compatible renewable sources of functional cells, an absence of appropriate biomaterials with desired mechanical, chemical, and biological properties, and an inability to generate significant, vascularized tissues with the architectural complexity of native tissues. Nevertheless, the area of tissue engineering has made considerable progress in addressing these problems due to our enhanced understanding of biology, materials science, chemistry, and engineering methodologies, as well as the merging of these fields. Moreover, the mechanical properties of materials and the size of the pore size of the fabricated scaffolds are two extremely important aspects [64], [65].

2.13.1 Biomaterials

All living organisms poses the ability of regeneration mediated by molecular processes, which are guided by the gene-expression that controls renewal, restoration and growth. The methodology of using the body's regenerative capabilities, in combination with engineered biomaterials, is recognized as in situ tissue regeneration and it was first introduced by Langer and Vacanti in 1993 [66]. In order to optimize the cell growth innovative protocols were developed to isolate and culture cells *in vitro*, populate a synthetic scaffold and then be implanted again into the body.

There are two fundamental techniques to tissue regeneration: *ex vivo* and *in situ*. A scaffold is employed in the *ex vivo* technique to introduce the cells and biomolecules that will eventually be transplanted into the body (**Figure 10**). However, this technique has several disadvantages, including difficult culture conditions, limited engraftment effectiveness, donor site morbidity, and, most critically, a high risk of immunological response. The *in-situ* technique, on the other hand, leverages the body's natural regenerative capability, removing the requirement for *ex vivo* cell exploitation but is ineffective for tissues with limited endogenous progenitor cells and is very difficult to monitor the regeneration process.

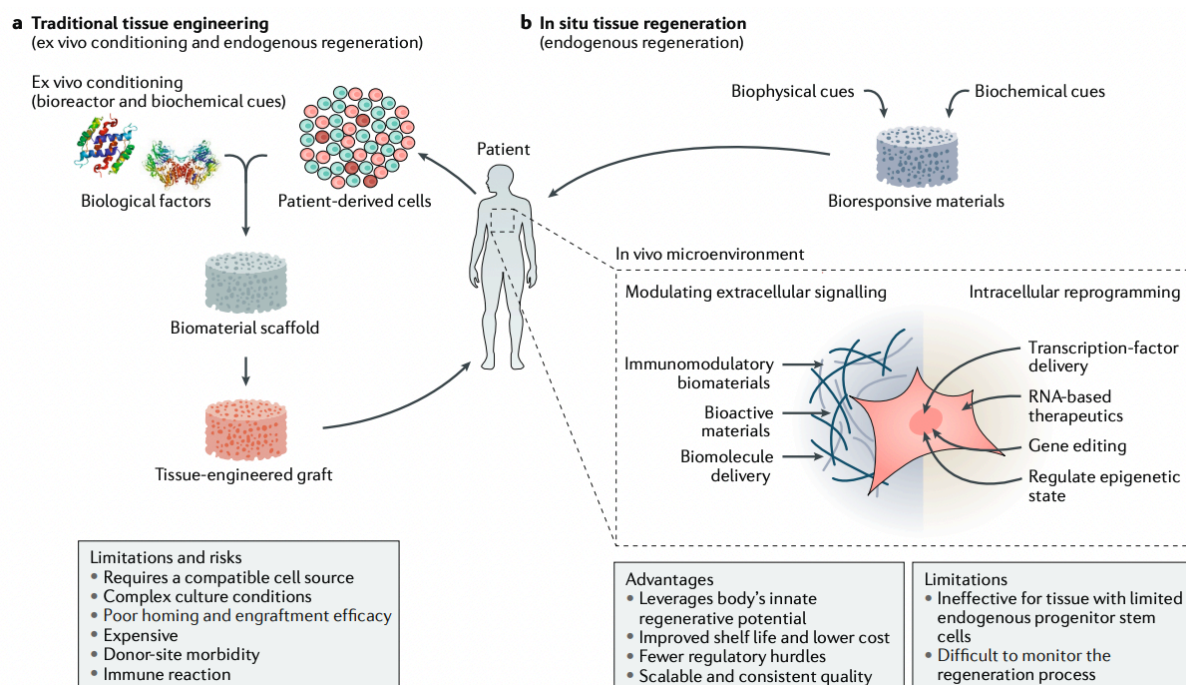


Figure 10. The two different approaches of regenerative medicine. a) *Ex vivo* method where the cells of the patient are culture with the scaffolds *ex vivo* and then are inserted into the body. B) *In situ* approach where a bio responsive material is inserted into the body where it can

modulate several extracellular signaling as well as intracellular. Figure used with permission from [67].

The range of scaffolds used for *in situ* tissue regeneration includes monolithic, microporous, nanoparticles, fibrous, hydrogels and 3D-printed scaffolds. Biomaterials used for fabrication of scaffolds can be polymers, ceramics, metals and composites. The biophysical characteristics of biomaterials, such as stiffness, structure, topography and degradation, can alter the local tissue microenvironments through intracellular and intercellular signaling. The **biophysical characteristics** of biomaterials, such as stiffness, structure, topography and degradation, can alter the local tissue microenvironments through intracellular and intercellular signaling (**Figure 11.a,b**). These variations in tissue microenvironment include fluctuating the temperature or pH, and controlling the presence of enzymes, ions or radical species and cells. The matrix stiffness orders the adhesion, dispersion and fate of stem cells [68], [69]. For example, bone marrow cells adhere and spread on stiffer surfaces, which direct stem cells fate towards osteogenic lineage, whereas a softer matrix addresses the cells to change their morphology into a more round-shaped type promoting chondrogenic differentiation. The porosity of the scaffold is another important aspect, as it can dictate cellular infiltration, as interconnected pore networks can accelerate the transport of waste products, oxygen and nutrients. Porosity was also shown to promote vascularization of scaffolds by aiding angiogenesis [70]. Likewise, topological structures, such as the presence of patterned surfaces, can promote or suppress cell adhesion and cell fate [71]. Most of the times, *in situ* degradation of biomaterials is preferred for tissue regeneration while the degradation rate should be close to the rate of tissue generation to have the optimal tissue growth. Many biomaterials can be degraded through cell enzymes like collagen or gelatin to remodel and deposit the newly synthesized tissue. Finally, it is extremely important for the biophysical cues of the scaffold to match those of the native tissue as mismatch may lead to suboptimal healing and may result in poor functionality of regenerated tissue, implant loosening and tissue loss.

The **biochemical characteristics** of biomaterials include the release of signalling biomolecules, such as small molecules or proteins in the form of drugs, as well as degradation of the scaffold (**Figure 11.c**). Biochemical cues are very important as they can be used to activate various signalling pathways or a set of genes to direct and regulate favourable cellular responses. For example, signalling factors released from responsive biomaterials can activate cell-receptor proteins, which control processes such as protein transport into the cell and other signalling pathways. It has been shown that by sequestering pro-angiogenic factors within the scaffolds angiogenesis *in vivo* can be stimulated [72]–[74]. This is really important as binding

molecules to the scaffolds can result in continuous activation of cell-scaffold receptors in a more sufficient manner than delivering growth factors [75]. In a different study, degradation of biomaterials can lead to the release of signalling ions that can modify the local micro-environment like calcium, which can trigger calcium-sensing receptors, proteins important for pathways concerning cell proliferation, differentiation and chemotaxis [76]. Moreover, other studies showed that release of ions from calcium-phosphate-based biomaterials can activate the differentiation of stem cells towards bone lineages [77], [78]. In conclusion, sequestering growth factors or releasing mineral ions from biomaterials can have a huge impact in the tissue microenvironment, further moderating regenerative procedures.

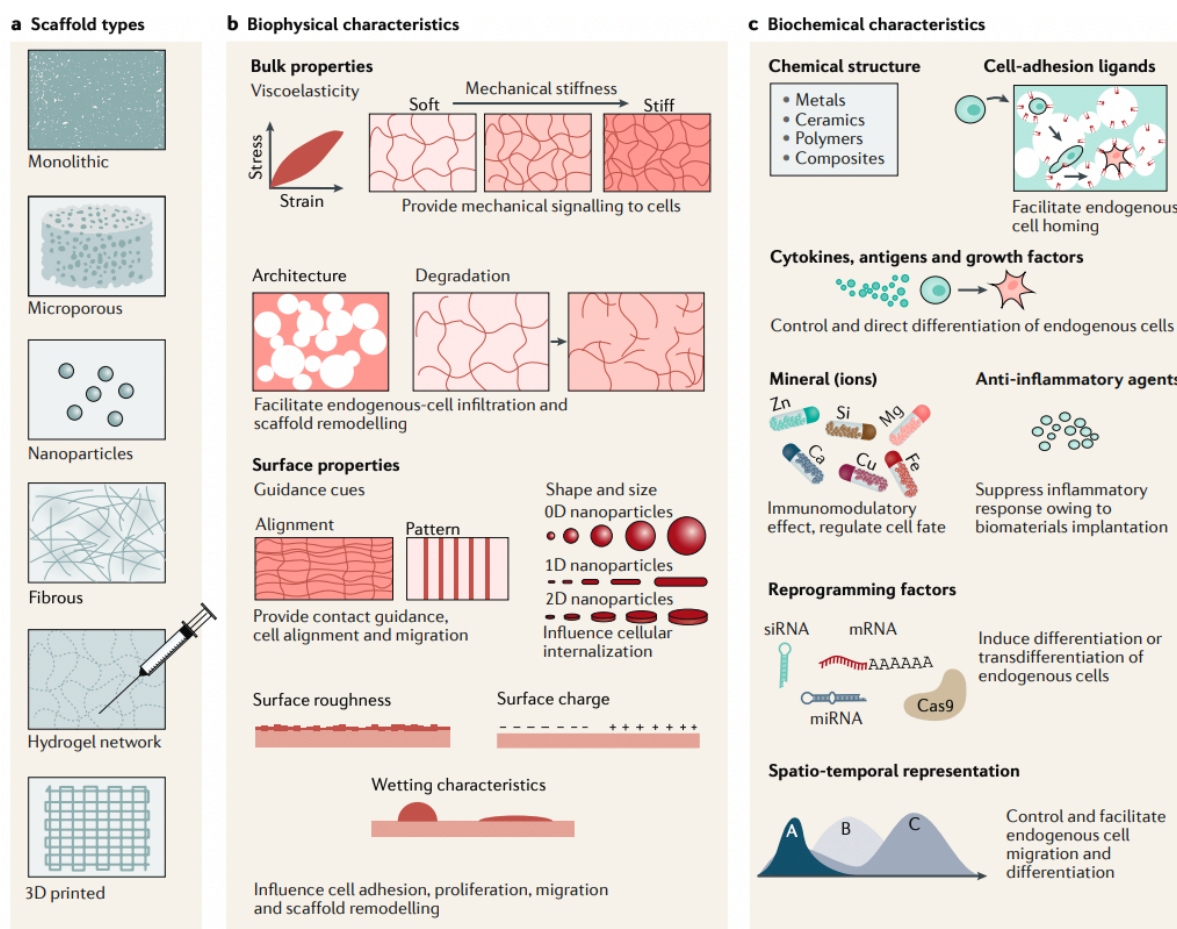


Figure 11. Approaches to engineered biomaterials for tissue regeneration. **a)** There are different kinds of scaffolds like monolithic, microporous, nanoparticles, fibrous hydrogel network and 3D printed that are developed to mimic the native characteristics of the different tissues. **b)** according to their biophysical characteristics, scaffolds can affect many different cell responses like adhesion, migration, proliferation and differentiation. **c)** Biochemical characteristics include the chemical structure of biomaterials, as well as the presence of signalling biomolecules, such as proteins, minerals, small-molecule drugs and reprogramming factors. Image used with permission from [67].

2.14 Mechanical Stress types cells experience

Stresses, such as shear, compression, and stretch (tension), are mechanical cues experienced by cells in a plethora of tissues throughout the body, while the mode and degree are different with time and position. For instance, Endothelial Cells in blood vessels experience constantly the pulsatile shear force of blood fluid [79] and chondrocytes in cartilage are under dynamic compression loads whereas tendon and ligament cells experience primarily tensile forces to properly function [80] (**Figure 12**). Therefore, cells in our body (i.e. myoblasts, chondrocytes, fibroblasts, adipocytes, neurons, and osteoblasts) are constantly adapt to physical forces of the ECM to preserve the mechanical and biological functions of the tissues they comprise [81].

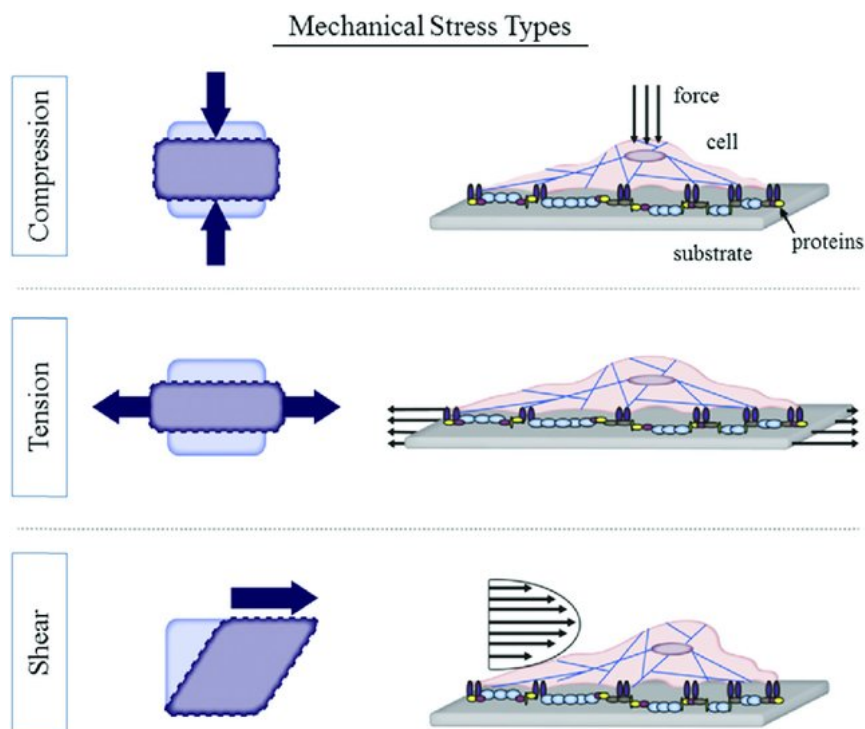


Figure 12. Different forces that cells experience through the organism. Figure used from [81].

2.15 Cell Mechano-sensing and Mechano-transduction

The cells have multiple distinct ways of sensing chemical or mechanical cues in their environment, both of which are very important for their fate. In general, the extracellular micro-environment (the ECM) consists of several biophysical, chemical and cellular cues that can lead to various cell responses. Thus, the ECM plays a crucial role in providing cellular scaffolding and sequestration of bioactive factors, thus influencing cell shape, proliferation, migration, and differentiation such that cells favor lineages that tension match the elasticity of

the substrate (e.g., stem cells on soft substrates favor neurogenic lineages, while stem cells on rigid substrates favor osteogenic lineages) [82].

The intracellular processes that transfer mechanical stimuli into transcriptional outputs are less well known. In general, mechanical signals are first detected by membrane-embedded proteins that operate as "stiffness sensors," such as integrins, G-protein coupled receptors (GPCR), FA, cadherins, and ion channels. [83]. This activates Rho-ROCK, FAK and integrin-mediated signaling pathways and, subsequently, the cytoskeleton reacts by changing its structure to alter the cellular contractility. Ultimately, these cytoskeletal changes activate downstream signaling pathways, such as YAP/TAZ signaling, leading to changes in cell morphology and fate.

2.15.1 Focal Adhesion Kinase (FAK)

Integrins are transmembrane receptors composed of non-covalently linked α and β subunits at the cell membrane that bind the cytoskeleton to the ECM directly. These transmembrane sensors detect several changes in the mechanical characteristics of the ECM. For example, increasing the stiffness of the ECM is sensed by integrin receptors on the cell surface. These integrin receptors are linked to the actin cytoskeleton via the "integrin adhesome," which is made up of multiple proteins [84] and is in charge of transmitting changes in the cellular microenvironment to the cytoskeleton [85]. To counteract the stresses exerted by the ECM, the cell reorganizes its actin cytoskeleton and strengthens its stress fibers in stiff microenvironments. This maintains a tensional balance between the cell and its surrounding milieu, since changes in cytoskeletal tension caused by stiffness are sent back to the ECM via FA and integrin receptors, allowing cells to adjust their surrounding matrix. [85].

Figure 13 shows a schematic representation of the focal adhesion kinase signaling where 3 layers of transduction are visible: integrin signaling layer, force transduction layer and actin regulatory layer. More specifically, when a change on the stiffness of the ECM is detected, then FAKs are recruited to integrin clusters and a Focal adhesion complex is created by recruitment of different proteins such as TLN, VCL and CAS which transduce the mechanical change of the environment into cellular cytoskeleton. Then, VASP, ZYX and α -actin are directing the formation of F-actin filaments.

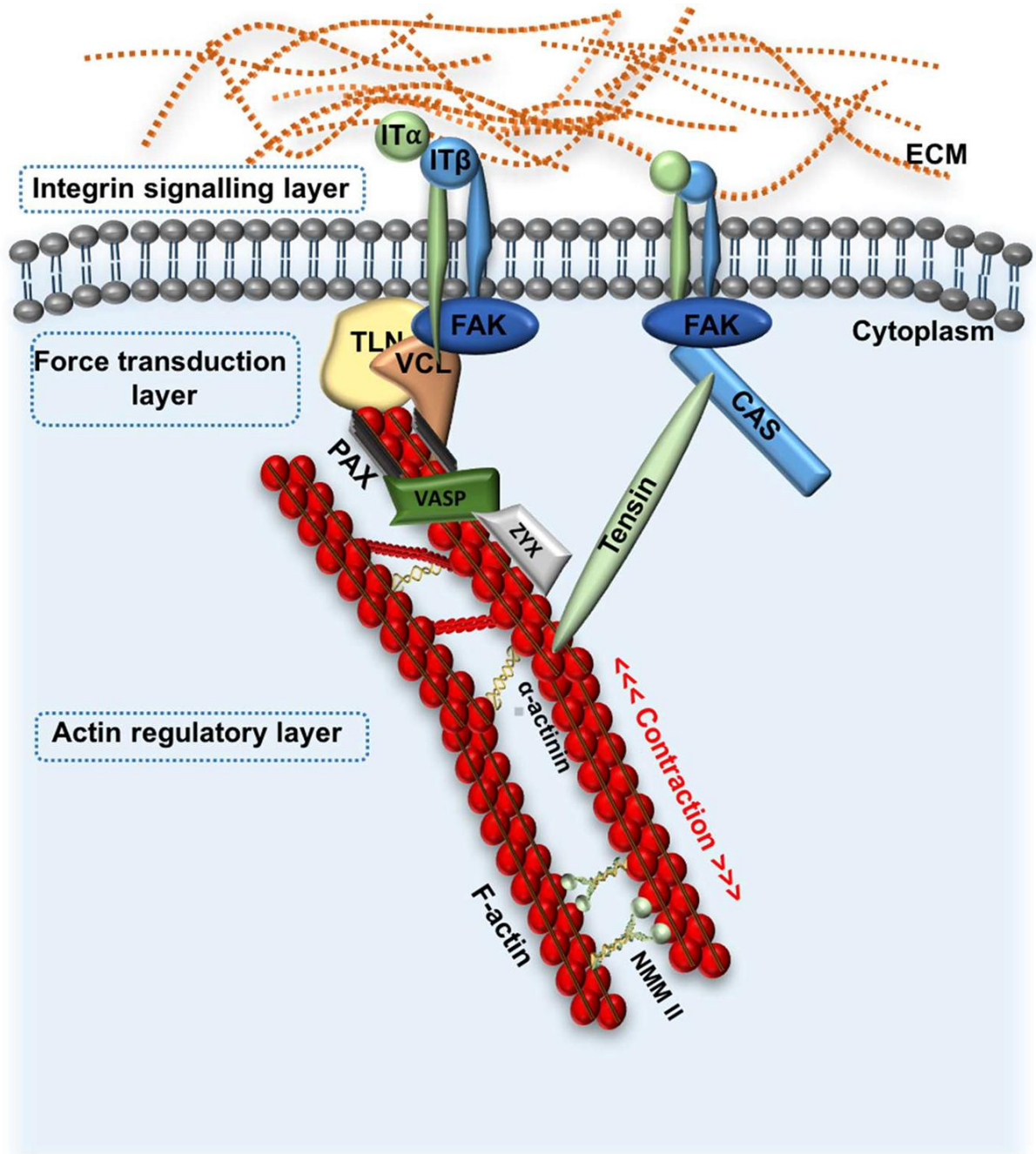


Figure 13. Schematic representation of the focal adhesion kinase signaling. FA, focal adhesion; ECM, extracellular matrix; IT α ;IT β , integrin subunit α and β ; FAK, focal adhesion kinase; TLN, talin; VCL, vinculin; Zyz, zyxin; NMM II, non-muscle myosin II; VASP, vasodilator-stimulated phosphoprotein. Figure used from [86].

2.15.2 Hippo pathway

Cell–ECM transduction initiates with transmembrane integrins binding to ECM proteins, which then transmits force across the plasma membrane of the cell to the focal adhesion complex (FAC). Multiple anchoring proteins are involved in coordinating the binding

of cytoskeletal actin to integrin subunits and are incorporated within the FAC59 such as the protein *talin* which is an anchoring protein necessary for actin- integrin linkage. Recent work also demonstrated that mechanotransductory cues from the ECM act on the downstream regulators Yes-associated protein (YAP) and transcriptional co-activator with PDZ binding motif (TAZ) of the Hippo signaling pathway [87]. **Figure 14** summarizes the two states that the Hippo pathway can be found. When the it is ON, MST1/2 phosphorylate SAV1 and together they phosphorylate and activate MOB1A/B and LATS1/2, which then phosphorylate YAP and TAZ. Phosphorylated YAP and TAZ are sequestered in the cytoplasm by the 14-3-3 phosphopeptide binding proteins and shunted for proteasomal degradation. As a result, the TEAD transcription factors associate with VGL4 and suppress target gene expression. On the other hand, when the Hippo pathway is OFF, the MST1/2 and LATS1/2 kinases are inactive, YAP and TAZ are not phosphorylated and accumulate in the nucleus where they displace VGL4 and complex with TEADs. YAP and TAZ are transcriptional co-activators and in complex with TEADs promote the transcription of target genes [88].

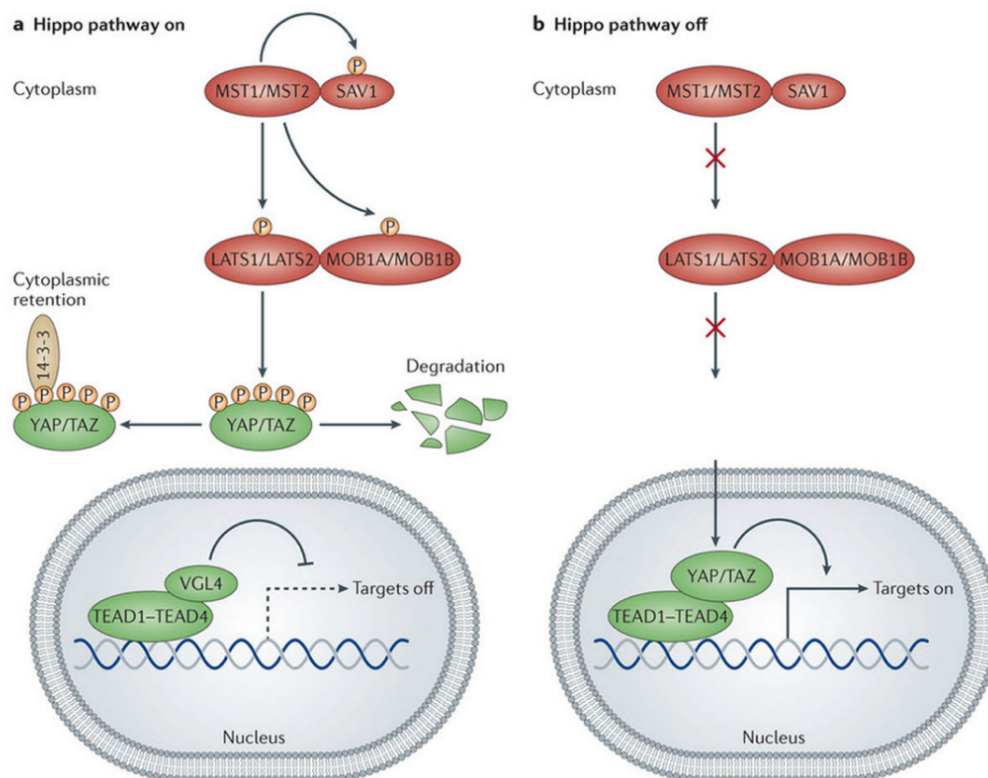


Figure 14. Schematic representation of the core of the Hippo signaling pathway and its modes of action. Figure used from [88].

2.15.3 YAP/TAZ complex

The Hippo pathway that was analyzed before transduces the nuclear relocation of the YAP/TAZ complex [89]. More specifically, in many organisms the phosphorylation of this complex due to the activation of the Hippo pathway leads to its degradation in proteasomes. Although it has been proven that the Hippo cascade is not responsible for the YAP/TAZ inhibition as mechanical cues and Hippo signaling represent two parallel inputs converging on YAP/TAZ regulation [90]. This pioneering work by Dupont et al. categorised YAP and TAZ as “mechano-sensors.” They identified that in MSC, the localisation of YAP/TAZ changes in response to mechanical cues such as shape, density, ECM stiffness and cytoskeletal tension [90]. Small micro-patterned islands with low ECM stiffness, high cell density, and a rounded form, in particular, enhanced cytoplasmic retention of YAP/TAZ, whereas bigger islands with high matrix stiffness, sparse cell density, and spreading favored nuclear accumulation of YAP/TAZ. Furthermore, YAP/TAZ location influenced MSC destiny. Nuclear YAP was discovered to enhance osteogenesis, whereas cytoplasmic YAP was shown to promote adipogenesis. Importantly, in vitro YAP/TAZ overexpression increases osteogenic differentiation and cell proliferation in cells on soft ECM, which is sufficient to "fool" cells into behaving as they would on a stiff matrix. In a nutshell, YAP/TAZ detect mechanical signals and mediate the cellular response to mechanical stimulation. The other aspect that regulates this complex is interestingly the Rho activity and the actomyosin cytoskeleton. More specifically, YAP/TAZ activity requires stress fibers and cytoskeletal tension induced by ECM stiffness and cell spreading, but is not directly regulated by G-actin levels.

2.16 Bone regeneration

Some of the most elusive works in clinical practice are tumors, severe infection, osteoporosis, osteonecrosis, and some congenital malformations that can cause large bone defects [91]. Various causes can induce those bone defects, and are currently one of the most important causes of morbidity and disability, a fact that dramatically reduces the quality of life [92]. With the rising amount of patients in our aging society, the total direct cost of patients with musculoskeletal disease augmented by 117% between 2009 and 2011. In addition, research and development costs are also expanding year by year. According to Food and Drug Administration data, the clinical development cost of products in phases I–III increased over \$14.0 billion in 2020. Moreover, the market for bone replacements was assessed at \$2.3 billion dollars in 2015, and this cost was expected to exceed \$3.6 billion from 2016 to 2022 [93].

Those amounts are invested into the research of bone regeneration as existing treatments, including autologous and allogenic grafts have many disadvantages such as the risk of infectious disease, limited resources, secondary injury and most commonly immunological rejection [94]–[96].

By definition, Bone Tissue Regeneration (BTR) is the field of tissue engineering that has to do with the insertion of an exogenous scaffold into the organism in order to encourage cells to proliferate and grow [97]. These scaffolds require to have specific properties some of which are biocompatibility, osteoconductivity, and suitable mechanical strength matching the one in the native bone tissue [98], [99]. Material science strives to use materials as implantable scaffolds such as metal, bioceramic, biopolymer, and composite implants [100]–[102]. Many issues remain to overcome to have a successful implant such as high cost, the probability of tumorigenesis due to the growth factors and most importantly the inability of the organism cell to incorporate the new implant [103].

2.16.1 Runx2 is affected by YAP

Regarding osteogenic differentiation, Runx2 activates and regulates osteogenesis as the main targeted gene of several signaling pathways, including transforming growth factor-beta 1 (TGF- β 1), BMP, Wingless type (Wnt), Hedgehog (HH), and (Nf1)-like protein type 1 (NELL-1). Direct interaction between YAP and Runx protein parts was documented in a cell-free system [104]. And it was therefore determined whether endogenous Runx2 and YAP interact in osteoblasts. Immunoprecipitation assay showed that those two proteins are able to form a complex *in vivo* in osteoblastic ROS 17/2.8 cells.

Src/Yes tyrosine kinase signalling pathway is responsible for regulating bone homeostasis and inhibition of osteoblast activity. It was shown that YAP protein, a mediator of Src/Yes signalling, interacts with the cellular Runx2 protein, which is the main osteoblast-related transcription factor, and suppresses its transcriptional activity. Moreover, Runx2 recruits YAP to subnuclear domains *in situ* and to the osteocalcin (OC) gene promoter *in vivo*. Inhibition of Src/Yes kinase blocks tyrosine phosphorylation of YAP and dissociates endogenous Runx2–YAP complexes. Consequently, recruitment of the YAP co-repressor to subnuclear domains is repealed and expression of the endogenous osteocalcin gene is induced leading to bone formation [105]. However, the role of YAP in bone homeostasis remains controversial, as in another study YAP function is promoting osteogenesis and suppressing adipogenesis [106].

References

- [1] M. Göppert-Mayer, “Über Elementarakte mit zwei Quantensprüngen,” *Ann Phys*, vol. 401, no. 3, pp. 273–294, Jan. 1931, doi: 10.1002/ANDP.19314010303.
- [2] E. J. Botcherby *et al.*, “Aberration-free three-dimensional multiphoton imaging of neuronal activity at kHz rates,” *Proc Natl Acad Sci U S A*, vol. 109, no. 8, pp. 2919–2924, Feb. 2012, doi: 10.1073/PNAS.1111662109.
- [3] K. S. Lee, D. Y. Yang, S. H. Park, and R. H. Kim, “Recent developments in the use of two-photon polymerization in precise 2D and 3D microfabrications,” *Polym Adv Technol*, vol. 17, no. 2, pp. 72–82, Feb. 2006, doi: 10.1002/PAT.664.
- [4] W. R. Zipfel, R. M. Williams, and W. W. Webb, “Nonlinear magic: multiphoton microscopy in the biosciences,” *Nature Biotechnology* 2003 21:11, vol. 21, no. 11, pp. 1369–1377, Oct. 2003, doi: 10.1038/nbt899.
- [5] B. G. Wang, K. König, and K. J. Halbhauer, “Two-photon microscopy of deep intravital tissues and its merits in clinical research,” *J Microsc*, vol. 238, no. 1, pp. 1–20, Apr. 2010, doi: 10.1111/J.1365-2818.2009.03330.X.
- [6] X. Wang *et al.*, “A chemically labeled cytotoxic agent: Two-photon fluorophore for optical tracking of cellular pathway in chemotherapy,” *Proc Natl Acad Sci U S A*, vol. 96, no. 20, pp. 11081–11084, Sep. 1999, doi: 10.1073/PNAS.96.20.11081/ASSET/7043BB2D-AB11-4DD5-8B5C-645D8D6F6166/ASSETS/GRAPHIC/PQ2093313005.JPEG.
- [7] S. B. Brown, E. A. Brown, and I. Walker, “The present and future role of photodynamic therapy in cancer treatment,” *Lancet Oncol*, vol. 5, no. 8, pp. 497–508, Aug. 2004, doi: 10.1016/S1470-2045(04)01529-3.
- [8] E. Walker and P. M. Rentzepis, “A new dimension,” *Nature Photonics* 2008 2:7, vol. 2, no. 7, pp. 406–408, Jul. 2008, doi: 10.1038/nphoton.2008.121.
- [9] M. Hunt *et al.*, “Harnessing Multi-Photon Absorption to Produce Three-Dimensional Magnetic Structures at the Nanoscale,” *Materials* 2020, Vol. 13, Page 761, vol. 13, no. 3, p. 761, Feb. 2020, doi: 10.3390/MA13030761.
- [10] W. R. Zipfel, R. M. Williams, and W. W. Webb, “Nonlinear magic: Multiphoton microscopy in the biosciences,” *Nat Biotechnol*, vol. 21, no. 11, pp. 1369–1377, Nov. 2003, doi: 10.1038/NBT899.
- [11] T. Frenzel, M. Kadic, and M. Wegener, “Three-dimensional mechanical metamaterials with a twist,” *Science* (1979), vol. 358, no. 6366, pp. 1072–1074, Nov. 2017, doi: 10.1126/science.aao4640.

- [12] P. Mueller, M. Thiel, and M. Wegener, “3D direct laser writing using a 405 nm diode laser,” *Opt Lett*, vol. 39, no. 24, p. 6847, Dec. 2014, doi: 10.1364/OL.39.006847.
- [13] P. F. (Paul F. Jacobs, *Stereolithography and other RP & M technologies : from rapid prototyping to rapid tooling*. Dearborn Mich. New York: Society of Manufacturing Engineers in cooperation with the Rapid Prototyping Association of SME ; ASME Press, 1996.
- [14] A. Egbert *et al.*, “Femtosecond laser-induced two-photon polymerization of inorganic–organic hybrid materials for applications in photonics,” *Optics Letters*, Vol. 28, Issue 5, pp. 301–303, vol. 28, no. 5, pp. 301–303, Mar. 2003, doi: 10.1364/OL.28.000301.
- [15] M. Farsari, M. Vamvakaki, and B. N. Chichkov, “Multiphoton polymerization of hybrid materials,” *Journal of Optics*, vol. 12, no. 12, 2010, doi: 10.1088/2040-8978/12/12/124001.
- [16] E. Skliutas *et al.*, “Polymerization mechanisms initiated by spatio-temporally confined light,” *Nanophotonics*, vol. 10, no. 2, pp. 1211–1242, Jan. 2021, doi: 10.1515/NANOPH-2020-0551/ASSET/GRAPHIC/J_NANOPH-2020-0551_FIG_006.JPG.
- [17] V. Hahn *et al.*, “Two-step absorption instead of two-photon absorption in 3D nanoprinting,” *Nature Photonics* 2021 15:12, vol. 15, no. 12, pp. 932–938, Nov. 2021, doi: 10.1038/s41566-021-00906-8.
- [18] M. Hippler *et al.*, “3D Scaffolds to Study Basic Cell Biology,” 2019, doi: 10.1002/adma.201808110.
- [19] B. Richter *et al.*, “Guiding Cell Attachment in 3D Microscaffolds Selectively Functionalized with Two Distinct Adhesion Proteins,” pp. 1–6, 2016, doi: 10.1002/adma.201604342.
- [20] V. Hahn *et al.*, “Rapid Assembly of Small Materials Building Blocks (Voxels) into Large Functional 3D Metamaterials,” *Adv Funct Mater*, vol. 30, no. 26, p. 1907795, Jun. 2020, doi: 10.1002/ADFM.201907795.
- [21] C. Darkes-Burkey and R. F. Shepherd, “High-resolution 3D printing in seconds,” *Nature* 2021 588:7839, vol. 588, no. 7839, pp. 594–595, Dec. 2020, doi: 10.1038/d41586-020-03543-3.
- [22] Y. Zhang *et al.*, “Continuous 3D printing from one single droplet,” *Nature Communications* 2020 11:1, vol. 11, no. 1, pp. 1–10, Sep. 2020, doi: 10.1038/s41467-020-18518-1.
- [23] A. J. Capel, R. P. Rimington, M. P. Lewis, and S. D. R. Christie, “3D printing for chemical, pharmaceutical and biological applications,” *Nat Rev Chem*, vol. 2, no. 12, pp. 422–436, 2018, doi: 10.1038/s41570-018-0058-y.
- [24] P. Zhang *et al.*, “Lightweight 3D bioprinting with point by point photocuring,” *Bioact Mater*, vol. 6, no. 5, pp. 1402–1412, 2021, doi: 10.1016/j.bioactmat.2020.10.023.

- [25] L. Breideband *et al.*, “Upgrading a Consumer Stereolithographic 3D Printer to Produce a Physiologically Relevant Model with Human Liver Cancer Organoids,” *Adv Mater Technol*, p. 2200029, May 2022, doi: 10.1002/ADMT.202200029.
- [26] B. G. Compton and J. A. Lewis, “3D-printing of lightweight cellular composites,” *Advanced Materials*, vol. 26, no. 34, pp. 5930–5935, 2014, doi: 10.1002/adma.201401804.
- [27] L. X. Deng, N. K. Liu, R. Wen, S. N. Yang, X. Wen, and X. M. Xu, “Laminin-coated multifilament entubulation, combined with Schwann cells and glial cell line-derived neurotrophic factor, promotes unidirectional axonal regeneration in a rat model of thoracic spinal cord hemisection,” *Neural Regen Res*, vol. 16, no. 1, pp. 186–191, 2021, doi: 10.4103/1673-5374.289436.
- [28] G. Battafarano *et al.*, “Strategies for bone regeneration: From graft to tissue engineering,” *Int J Mol Sci*, vol. 22, no. 3, pp. 1–22, 2021, doi: 10.3390/ijms22031128.
- [29] A. W. Feinberg, “Engineered tissue grafts: Opportunities and challenges in regenerative medicine,” *Wiley Interdiscip Rev Syst Biol Med*, vol. 4, no. 2, pp. 207–220, 2012, doi: 10.1002/wsbm.164.
- [30] S. Maruo and S. Kawata, “Two-photon-absorbed near-infrared photopolymerization for three-dimensional microfabrication,” *Journal of Microelectromechanical Systems*, vol. 7, no. 4, pp. 411–415, Dec. 1998, doi: 10.1109/84.735349.
- [31] K. K. Seet, S. Juodkazis, V. Jarutis, and H. Misawa, “Feature-size reduction of photopolymerized structures by femtosecond optical curing of SU-8,” *Appl Phys Lett*, vol. 89, no. 2, p. 024106, Jul. 2006, doi: 10.1063/1.2221499.
- [32] J. Kopeček, “Hydrogel biomaterials: A smart future?,” *Biomaterials*, vol. 28, no. 34, pp. 5185–5192, Dec. 2007, doi: 10.1016/J.BIOMATERIALS.2007.07.044.
- [33] S. R. Caliari and J. A. Burdick, “A practical guide to hydrogels for cell culture,” *Nature Methods 2016 13:5*, vol. 13, no. 5, pp. 405–414, Apr. 2016, doi: 10.1038/nmeth.3839.
- [34] I. Sakellari *et al.*, “Two-photon polymerization of titanium-containing sol–gel composites for three-dimensional structure fabrication,” *Applied Physics A 2010 100:2*, vol. 100, no. 2, pp. 359–364, Jul. 2010, doi: 10.1007/S00339-010-5864-0.
- [35] E. Kabouraki, A. N. Giakoumaki, P. Danilevicius, D. Gray, M. Vamvakaki, and M. Farsari, “Redox multiphoton polymerization for 3D nanofabrication,” *Nano Lett*, vol. 13, no. 8, pp. 3831–3835, Aug. 2013, doi: 10.1021/NL401853K/ASSET/IMAGES/MEDIUM/NL-2013-01853K_0005.GIF.

- [36] M. Malinauskas *et al.*, “Direct laser writing of microoptical structures using a Ge-containing hybrid material,” *Metamaterials*, vol. 5, no. 2–3, pp. 135–140, Jun. 2011, doi: 10.1016/J.METMAT.2011.04.002.
- [37] H. Lim and S. W. Hoag, “Plasticizer effects on physical-mechanical properties of solvent cast Soluplus® films,” *AAPS PharmSciTech*, vol. 14, no. 3, pp. 903–910, Sep. 2013, doi: 10.1208/S12249-013-9971-Z.
- [38] R. S. Kshetrimayum, “A brief intro to metamaterials,” *IEEE Potentials*, vol. 23, no. 5, pp. 44–46, Dec. 2004, doi: 10.1109/MP.2005.1368916.
- [39] N. A. Fleck, V. S. Deshpande, and M. F. Ashby, “Micro-architected materials: past, present and future,” *Proceedings of the Royal Society A: Mathematical, Physical and Engineering Sciences*, vol. 466, no. 2121, pp. 2495–2516, Sep. 2010, doi: 10.1098/RSPA.2010.0215.
- [40] U. G. K. Wegst, H. Bai, E. Saiz, A. P. Tomsia, and R. O. Ritchie, “Bioinspired structural materials,” *Nature Materials* 2014 14:1, vol. 14, no. 1, pp. 23–36, Oct. 2014, doi: 10.1038/nmat4089.
- [41] F. Libonati and M. J. Buehler, “Advanced Structural Materials by Bioinspiration,” *Adv Eng Mater*, vol. 19, no. 5, p. 1600787, May 2017, doi: 10.1002/ADEM.201600787.
- [42] R. Lakes, “Materials with structural hierarchy,” *Nature* 1993 361:6412, vol. 361, no. 6412, pp. 511–515, 1993, doi: 10.1038/361511a0.
- [43] K. E. Evans, “Auxetic polymers: a new range of materials,” *Endeavour*, vol. 15, no. 4, pp. 170–174, Jan. 1991, doi: 10.1016/0160-9327(91)90123-S.
- [44] R. Lakes, “Foam Structures with a Negative Poisson’s Ratio,” *Science (1979)*, vol. 235, no. 4792, pp. 1038–1040, Feb. 1987, doi: 10.1126/SCIENCE.235.4792.1038.
- [45] V. A. Lvov, F. S. Senatov, A. A. Veveris, V. A. Skrybykina, and A. D. Lantada, “Auxetic Metamaterials for Biomedical Devices: Current Situation, Main Challenges, and Research Trends,” *Materials* 2022, Vol. 15, Page 1439, vol. 15, no. 4, p. 1439, Feb. 2022, doi: 10.3390/MA15041439.
- [46] K. Ando and H. Onda, “Mechanism for deformation of wood as a honeycomb structure I: Effect of anatomy on the initial deformation process during radial compression,” *Journal of Wood Science*, vol. 45, no. 2, pp. 120–126, 1999, doi: 10.1007/BF01192328.
- [47] T. M. Ryan and C. N. Shaw, “Trabecular bone microstructure scales allometrically in the primate humerus and femur,” *Proceedings of the Royal Society B: Biological Sciences*, vol. 280, no. 1758, May 2013, doi: 10.1098/RSPB.2013.0172.

- [48] P. van Liedekerke *et al.*, “A particle-based model to simulate the micromechanics of single-plant parenchyma cells and aggregates,” *Phys Biol*, vol. 7, no. 2, 2010, doi: 10.1088/1478-3975/7/2/026006.
- [49] J. Shen, Y. M. Xie, X. Huang, S. W. Zhou, and D. Ruan, “Compressive behavior of luffa sponge material at high strain rate,” *Key Eng Mater*, vol. 535–536, pp. 465–468, 2013, doi: 10.4028/WWW.SCIENTIFIC.NET/KEM.535-536.465.
- [50] J. A. Kepler, “Simple stiffness tailoring of balsa sandwich core material,” *Compos Sci Technol*, vol. 71, no. 1, pp. 46–51, Jan. 2011, doi: 10.1016/J.COMPSCITECH.2010.10.002.
- [51] N. Lyu, B. Lee, and K. Saitou, “Optimal subassembly partitioning of space frame structures for in-process dimensional adjustability and stiffness,” *Journal of Mechanical Design, Transactions of the ASME*, vol. 128, no. 3, pp. 527–535, May 2006, doi: 10.1115/1.2181599.
- [52] L. Valdevit, A. J. Jacobsen, J. R. Greer, and W. B. Carter, “Protocols for the optimal design of multi-functional cellular structures: From hypersonics to micro-architected materials,” *Journal of the American Ceramic Society*, vol. 94, no. SUPPL. 1, pp. s15–s34, 2011, doi: 10.1111/J.1551-2916.2011.04599.X.
- [53] S. Baudis *et al.*, “Elastomeric degradable biomaterials by photopolymerization-based CAD-CAM for vascular tissue engineering,” *Biomedical Materials*, vol. 6, no. 5, 2011, doi: 10.1088/1748-6041/6/5/055003.
- [54] K. Arcaute, B. K. Mann, and R. B. Wicker, “Fabrication of off-the-shelf multilumen poly(Ethylene glycol) nerve guidance conduits using stereolithography,” *Tissue Eng Part C Methods*, vol. 17, no. 1, pp. 27–38, Aug. 2010, doi: 10.1089/TEN.TEC.2010.0011.
- [55] H. Fan *et al.*, “Modulus-density scaling behaviour and framework architecture of nanoporous self-assembled silicas,” *Nat Mater*, vol. 6, no. 6, pp. 418–423, 2007, doi: 10.1038/NMAT1913.
- [56] L. J. Gibson, “Cellular solids,” *MRS Bull*, vol. 28, no. 4, pp. 270–274, 2003, doi: 10.1557/MRS2003.79.
- [57] A. Torrents, T. A. Schaedler, A. J. Jacobsen, W. B. Carter, and L. Valdevit, “Characterization of nickel-based microlattice materials with structural hierarchy from the nanometer to the millimeter scale,” *Acta Mater*, vol. 60, no. 8, pp. 3511–3523, May 2012, doi: 10.1016/J.ACTAMAT.2012.03.007.
- [58] C. Q. Dam, R. Brezny, and D. J. Green, “Compressive Behavior and Deformation-Mode Map of an Open Cell Alumina,” *J Mater Res*, vol. 5, no. 1, pp. 163–171, 1990, doi: 10.1557/JMR.1990.0163.
- [59] D. Rayneau-Kirkhope, Y. Mao, and R. Farr, “Ultralight fractal structures from hollow tubes,” *Phys Rev Lett*, vol. 109, no. 20, Nov. 2012, doi: 10.1103/PHYSREVLETT.109.204301.

- [60] T. M. Tillotson and L. W. Hrubesh, “Transparent ultralow-density silica aerogels prepared by a two-step sol-gel process,” *J Non Cryst Solids*, vol. 145, no. C, pp. 44–50, 1992, doi: 10.1016/S0022-3093(05)80427-2.
- [61] Z. Vangelatos *et al.*, “Strength through defects: A novel Bayesian approach for the optimization of architected materials,” *Sci Adv*, vol. 7, no. 41, Oct. 2021, doi: 10.1126/SCIADV.ABK2218.
- [62] S. Shi, Y. Li, B. N. Ngo-Dinh, J. Markmann, and J. Weissmüller, “Scaling behavior of stiffness and strength of hierarchical network nanomaterials,” *Science (1979)*, vol. 371, no. 6533, pp. 1026–1033, Mar. 2021, doi: 10.1126/SCIENCE.ABD9391.
- [63] X. Zheng *et al.*, “Ultralight, ultrastiff mechanical metamaterials,” *Science (1979)*, vol. 344, no. 6190, pp. 1373–1377, Jun. 2014, doi: 10.1126/SCIENCE.1252291/SUPPL_FILE/ZHENG.SM.PDF.
- [64] H. Ahmadzadeh *et al.*, “Modeling the two-way feedback between contractility and matrix realignment reveals a nonlinear mode of cancer cell invasion,” *Proc Natl Acad Sci U S A*, vol. 114, no. 9, pp. E1617–E1626, Feb. 2017, doi: 10.1073/PNAS.1617037114.
- [65] L. Wullkopf *et al.*, “Cancer cells’ ability to mechanically adjust to extracellular matrix stiffness correlates with their invasive potential,” *Mol Biol Cell*, vol. 29, no. 20, pp. 2378–2385, Oct. 2018, doi: 10.1091/MBC.E18-05-0319.
- [66] J. V. R Langer, “Tissue engineering,” *Science (1979)*, vol. 260, pp. 920–926, 1993.
- [67] A. K. Gaharwar, I. Singh, and A. Khademhosseini, “Engineered biomaterials for in situ tissue regeneration,” *Nature Reviews Materials 2020 5:9*, vol. 5, no. 9, pp. 686–705, Jul. 2020, doi: 10.1038/s41578-020-0209-x.
- [68] S. S. H. S. D. D. AJ Engler, “Matrix elasticity directs stem cell lineage specification,” *Cell*, vol. 126, pp. 677–689, 2006.
- [69] A. E. GC Reilly, “Intrinsic extracellular matrix properties regulate stem cell differentiation,” *J. Biomech.*, vol. 43, pp. 55–62, 2010.
- [70] W. W. P. S. D. C. T. S. DR Griffin, “Accelerated wound healing by injectable microporous gel scaffolds assembled from annealed building blocks,” *Nat. Mater.*, vol. 14, pp. 737–744, 2015.
- [71] P. Viswanathan, “3D surface topology guides stem cell adhesion and differentiation,” *Biomaterials*, vol. 52, pp. 140–147, 2015.
- [72] L. C. M. M. F. G. J. H. PS Briquez, “Design principles for therapeutic angiogenic materials,” *Nat. Rev. Mater.*, vol. 1, p. 15006, 2016.
- [73] J. K. X. Y. G. A. R. O. JI Dawson, “Clay gels for the delivery of regenerative microenvironments,” *Adv. Mater.*, vol. 23, pp. 3304–3308, 2011.

- [74] S. G. S. C. T. S. LR Nih, “Dual-function injectable angiogenic biomaterial for the repair of brain tissue following stroke,” *Nat. Mater.*, vol. 17, pp. 642–651, 2018.
- [75] H.-P. G. J. L. N Ferrara, “The biology of VEGF and its receptors,” *Nat. Med.*, vol. 9, pp. 669–676, 2003.
- [76] E. B. AM Hofer, “Extracellular calcium sensing and signalling,” *Nat. Rev. Mol. Cell Biol.*, vol. 4, pp. 530–538, 2003.
- [77] X. Y. C. B. W. M. T. M. Y Wang, “Mineral particles modulate osteo-chondrogenic differentiation of embryonic stem cell aggregates,” *Acta Biomater.*, vol. 29, pp. 42–51, 2016.
- [78] K. L. J. C. J. S. C Wang, “Osteogenesis and angiogenesis induced by porous β -CaSiO₃/PDLGA composite scaffold via activation of AMPK/ERK1/2 and PI3K/Akt pathways,” *Biomaterials*, vol. 34, pp. 64–77, 2013.
- [79] E. Dejana, K. K. Hirschi, and M. Simons, “The molecular basis of endothelial cell plasticity,” *Nature Communications 2017 8:1*, vol. 8, no. 1, pp. 1–11, Feb. 2017, doi: 10.1038/ncomms14361.
- [80] K. H. Vining and D. J. Mooney, “Mechanical forces direct stem cell behaviour in development and regeneration,” *Nature Reviews Molecular Cell Biology 2017 18:12*, vol. 18, no. 12, pp. 728–742, Nov. 2017, doi: 10.1038/nrm.2017.108.
- [81] L. Wang, S. Wu, G. Cao, Y. Fan, N. Dunne, and X. Li, “Biomechanical studies on biomaterial degradation and co-cultured cells: mechanisms, potential applications, challenges and prospects,” *J Mater Chem B*, vol. 7, no. 47, pp. 7439–7459, 2019, doi: 10.1039/C9TB01539F.
- [82] A. J. Engler, S. Sen, H. L. Sweeney, and D. E. Discher, “Matrix elasticity directs stem cell lineage specification,” *Cell*, vol. 126, no. 4, pp. 677–689, Aug. 2006, doi: 10.1016/J.CELL.2006.06.044.
- [83] M. Aragona *et al.*, “A mechanical checkpoint controls multicellular growth through YAP/TAZ regulation by actin-processing factors,” *Cell*, vol. 154, no. 5, pp. 1047–1059, Aug. 2013, doi: 10.1016/J.CELL.2013.07.042.
- [84] S. E. Winograd-Katz, R. Fässler, B. Geiger, and K. R. Legate, “The integrin adhesome: from genes and proteins to human disease,” *Nat Rev Mol Cell Biol*, vol. 15, no. 4, pp. 273–288, 2014, doi: 10.1038/NRM3769.
- [85] D. E. Ingber, “Cellular mechanotransduction: putting all the pieces together again,” *FASEB J*, vol. 20, no. 7, pp. 811–827, May 2006, doi: 10.1096/FJ.05-5424REV.
- [86] J. Petzold and E. Gentleman, “Intrinsic Mechanical Cues and Their Impact on Stem Cells and Embryogenesis,” *Front Cell Dev Biol*, vol. 9, p. 3112, Nov. 2021, doi: 10.3389/FCELL.2021.761871/XML/NLM.

- [87] F. Calvo *et al.*, “Mechano-transduction and YAP-dependent matrix remodelling is required for the generation and maintenance of cancer associated fibroblasts”, doi: 10.1038/ncb2756.
- [88] R. Johnson and G. Halder, “The two faces of Hippo: targeting the Hippo pathway for regenerative medicine and cancer treatment,” *Nat Rev Drug Discov*, vol. 13, no. 1, pp. 63–79, 2014, doi: 10.1038/nrd4161.
- [89] D. Pan, “The hippo signaling pathway in development and cancer,” *Dev Cell*, vol. 19, no. 4, pp. 491–505, Oct. 2010, doi: 10.1016/J.DEVCEL.2010.09.011.
- [90] S. Dupont *et al.*, “Role of YAP/TAZ in mechanotransduction,” *Nature*, vol. 474, no. 7350, pp. 179–184, Jun. 2011, doi: 10.1038/NATURE10137.
- [91] Y. Zhang, “Advancements in hydrogel-based drug sustained release systems for bone tissue engineering,” *Front. Pharmacol.*, vol. 11, p. 622, 2020.
- [92] P. Wang, “Bone tissue engineering via nanostructured calcium phosphate biomaterials and stem cells,” *Bone Res.*, vol. 2, p. 14017, 2014.
- [93] L. S. X. N. Y. F. P. M. M Dang, “Biomimetic delivery of signals for bone tissue engineering,” *Bone Res.*, vol. 6, p. 25, 2018.
- [94] G. Turnbull, “3D bioactive composite scaffolds for bone tissue engineering,” *Bioact. Mater.*, vol. 3, pp. 278–314, 2018.
- [95] W. Sun, “Injectable nano-structured silicon-containing hydroxyapatite microspheres with enhanced osteogenic differentiation and angiogenic factor expression,” *Ceram. Int.*, vol. 44, pp. 20457–20464, 2018.
- [96] F. Shang, “Advancing application of mesenchymal stem cell-based bone tissue regeneration,” *Bioact. Mater.*, vol. 6, pp. 666–683, 2021.
- [97] M. C. MP Nikolova, “Recent advances in biomaterials for 3D scaffolds: a review,” *Bioact. Mater.*, vol. 4, pp. 271–292, 2019.
- [98] C. Wang, “3D printing of bone tissue engineering scaffolds,” *Bioact. Mater.*, vol. 5, pp. 82–91, 2020.
- [99] M. S. S. B. M. N. S. T. R. MM Islam, “Chitosan based bioactive materials in tissue engineering applications—a review,” *Bioact. Mater.*, vol. 5, pp. 164–183, 2020.
- [100] K. Lin, “Enhanced osteoporotic bone regeneration by strontium-substituted calcium silicate bioactive ceramics,” *Biomaterials*, vol. 34, pp. 10028–10042, 2013.
- [101] C. Wang, “Strontium released bi-lineage scaffolds with immunomodulatory properties induce a pro-regenerative environment for osteochondral regeneration,” *Mat. Sci. Eng. C.*, vol. 103, p. 109833, 2019.

- [102] M. G. JM Sadowska, “Inflammation and biomaterials: role of the immune response in bone regeneration by synthetic bone grafts,” *J. Mater. Chem. B*, vol. 8, pp. 9404–9427, 2020.
- [103] F. U. R. C. Z. B. L. N. H. H Yi, “Recent advances in nano scaffolds for bone repair,” *Bone Res.*, vol. 4, p. 16050, 2016.
- [104] R. Yagi, L. F. Chen, K. Shigesada, Y. Murakami, and Y. Ito, “A WW domain-containing yes-associated protein (YAP) is a novel transcriptional co-activator,” *EMBO J*, vol. 18, no. 9, pp. 2551–2562, May 1999, doi: 10.1093/EMBOJ/18.9.2551.
- [105] S. K. Zaidi *et al.*, “Tyrosine phosphorylation controls Runx2-mediated subnuclear targeting of YAP to repress transcription,” *EMBO Journal*, vol. 23, no. 4, pp. 790–799, Feb. 2004, doi: 10.1038/SJ.EMBOJ.7600073.
- [106] J. X. Pan *et al.*, “YAP promotes osteogenesis and suppresses adipogenic differentiation by regulating β -catenin signaling,” *Bone Research 2018 6:1*, vol. 6, no. 1, pp. 1–12, Jun. 2018, doi: 10.1038/s41413-018-0018-7.

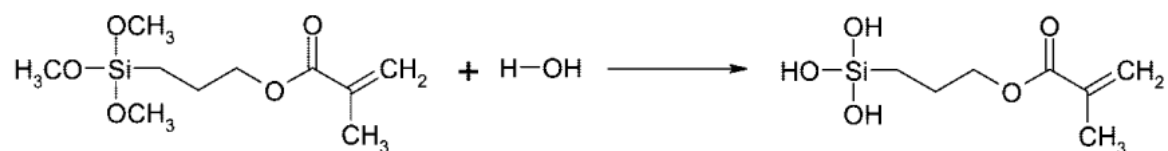
Chapter 3

3 Materials and Methods

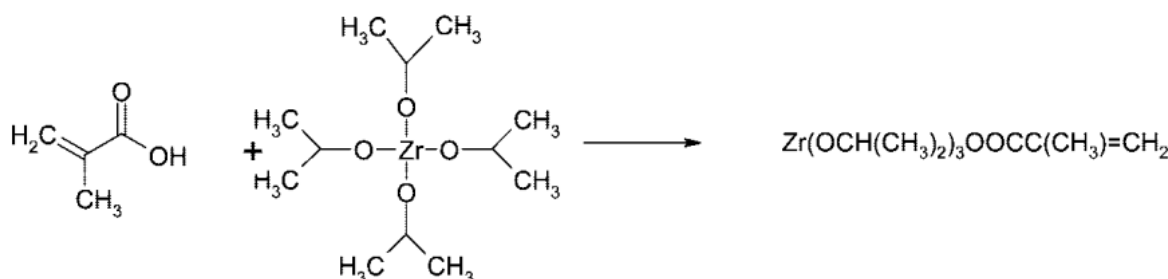
3.1 Material formulation

In this work, the hybrid organic-inorganic photoresist material was synthesized and used called SZ2080TM [1]. The formulation process of this material is called sol-gel and is summarized in **Figure 15**. The critical components of the material are the methacryloxypropyl trimethoxysilane (MAPTMS) and the ZPO, which by varying the molar ratio, gives the material different properties such as different refractive index or mechanical properties. In more detail, the first reaction step is hydrolysis, where the MAPTMS is hydrolyzed, and hydroxyls replace the three methyl groups of the silicate molecule. Then, in another reaction, the ZPO creates a complex with the Methacrylic Acid (MAA) and is hydrolyzed. Afterward, the two reagents are mixed, and through a condensation step, the organic-inorganic network is created where the silicate organic part is altered with the Zirconium inorganic part. Finally, a photoinitiator molecule is added, which is responsible for absorbing photons, and gives rise to free radicals to start the free radical polymerization (FRP), a well-defined mechanism [2].

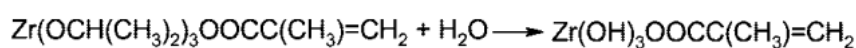
In brief, methacryloxypropyl trimethoxysilane (MAPTMS, 99%, Polysciences Inc.) was hydrolyzed with dilute HCl. Separately, methacrylic acid (MAA, 98%, Sigma-Aldrich) and zirconium n-propoxide (ZPO, 70% in propanol, Sigma -Aldrich) were combined in a molar ratio of 1:1 and stirred for 30 min; then the second composite was slowly added to the first. Two photoinitiators were used in this study: SBB (Sigma-Aldrich 0.04% with respect to the monomers), for the fabrication of low autofluorescence 3D structures, and 4,4'-bis(diethylamino) benzophenone (Michler's ketone, Sigma-Aldrich, 1% with respect to the monomers), as a control. It should be noted that Michler's ketone was directly incorporated inside the material, while SBB was firstly mixed with isopropanol in a concentration of 0.3% w/v, and then through a 1:10 dilution was added to the material (final concentration of 0.04% with respect to the monomers). After adding the photoinitiator, all materials were filtered using a 0.2 μ m pore filter.



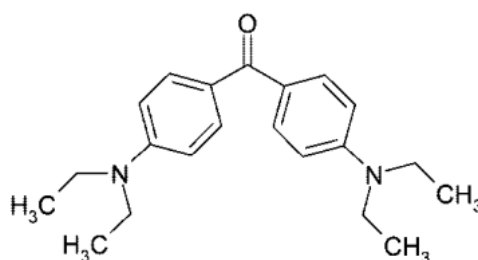
(a) MAPTMS hydrolysis



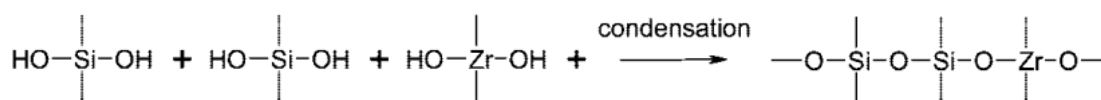
(b) MAA-ZPO complexation



(c) ZPO hydrolysis



(d) 4,4'-bis(diethylamino)benzophenone



(e) condensation

Figure 15. Chemical structure of the components of the sol gel method leading to the synthesis of the organic inorganic resin SZ2080. Figure used from [3]

3.2 Scaffold fabrication using Multiphoton Lithography

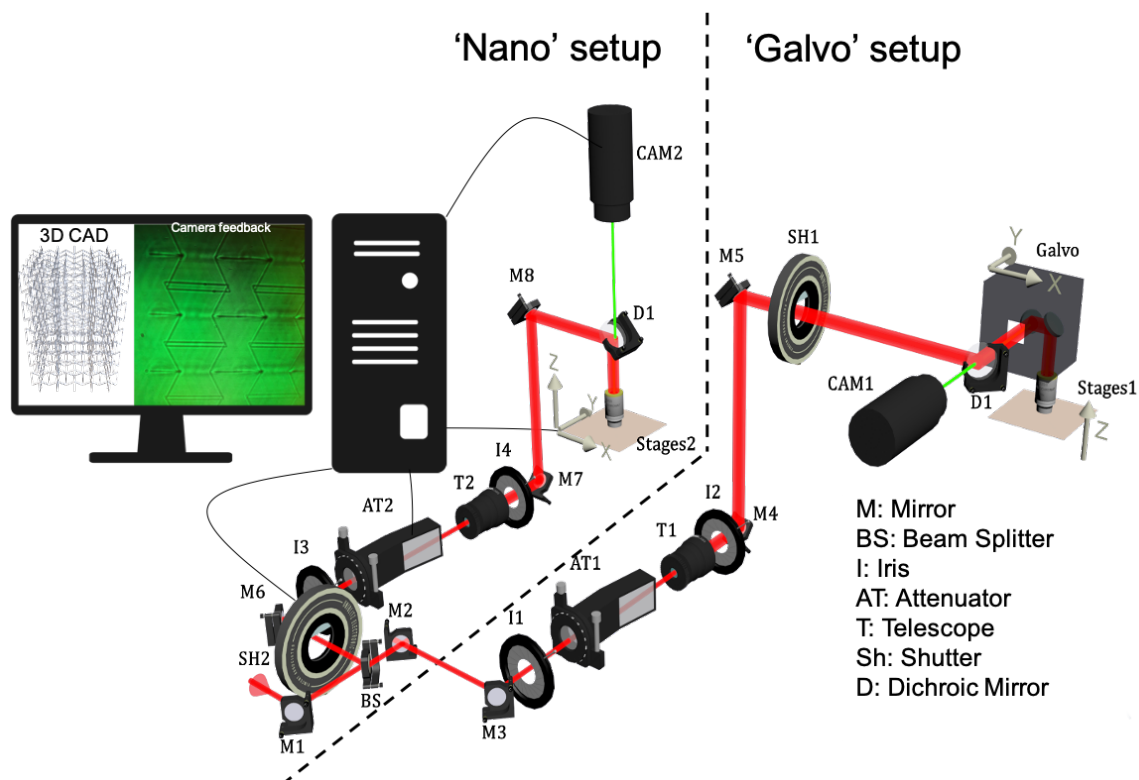
The experimental setup used in this work is shown in **Figure 16**. It consists of two scanning systems, which have been described in detail. Both systems use the same irradiation source: a fiber fs laser operating at 780 nm (totpica, pulse duration 120 fs, repetition rate 80 MHz).

The initial setup (referred to as nano setup) employs piezo- electric stages for the xyz movement (Physik Instrumente M-110.1DG). In this case, a second, oil-immersed, focusing microscope objective lens is also used (100x, NA = 1.4, Zeiss, Plan Apochromat). All the

auxetic scaffolds were made using this setup, with a laser fluence of 106 mJ.cm^{-2} and $80 \text{ }\mu\text{m.s}^{-1}$ scanning speed.

The second setup uses a galvanometric mirror system (Scan-labs Hurriscan II) to scan the laser beam inside the material on the xy-plane, while a linear translation stage moves the sample in the z-direction (Physik Instrumente M-500). The galvanometer was adapted to house a microscope objective lens. This setup was used to fabricate the structures for the mechanical characterization of the material.

The galvo setup was later updated to house a 4f system which is an important element for taking advantage of the whole aperture of the objective lens and fabricate as large scaffolds as possible. Also, an acousto-optic modulator was introduced that acted as a shutter. This element enabled us to fabricate the structure much faster due to the almost instantaneous respond of the element to block the beam in comparison with a mechanical shutter that takes several milliseconds to completely close and open. The updated setup is illustrated in **Figure 16 b**. All the parameneters used fro the fabrication of the scaffolds and structures are summarized in **Table 4**.



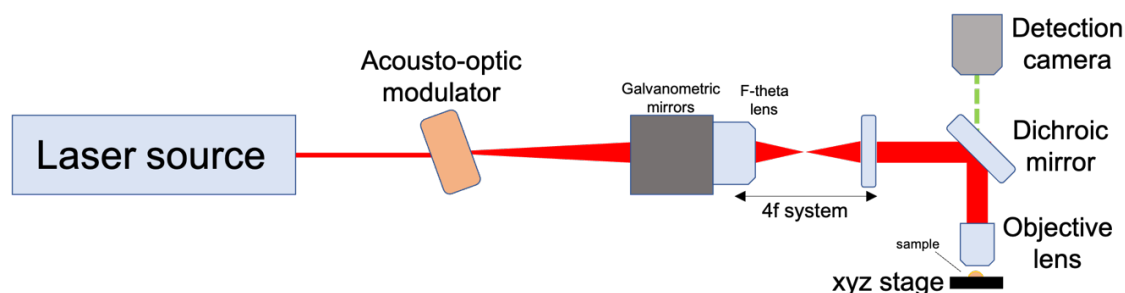


Figure 16. Multiphoton lithography setup (made using 3ds MAX 2020). All the scaffolds were 3D printed using the “nano” setup which is able to make very accurate and detailed structures up to few nanometers. A 3D computer-aided design (CAD) of the design is inserted into the computer and the movement of the stages, attenuator, and shutter are orchestrated by 3Dpoli software. b) The updated ‘GALVO’ v.2 setup where a 4f system is introduced after the galvanometric mirror scanner system.

Table 4. Condition of the fabricated structures.

Structure	Objective lens	System	Scanning speed ($\mu\text{m.s}^{-1}$)	Power (mW)	Hatching distance (μm)	Slicing distance (μm)
Vertical Auxetic	100X	NANO	variable	variable	-	-
Horizontal						
Auxetic (small pore)	100X	NANO	80	15	-	-
Horizontal						
Auxetic (large pore)	100X	NANO	80	15	4 X $0.5\mu\text{m}$	-
Woodpiles (SBB)	20X	GALVO v.1	50,000	200	0.5	5
Kelvin foam v.1	20X	NANO	100	30	-	-
Auxetic v.1	40X	NANO	100	25	-	-
Auxetic v.2	20X	GALVO v.2	50,000	230	1	2

3.3 3D printer and resin

In this study, an LCD SLA 3D printing system by Anycubic (4k photon mono) was used along with UV-sensitive resin from the same company, which is a mixture of polyurethane acrylate (30-60%), isooctyl-acrylate (10-40%) and the photoinitiator Irgacure 127 (2-hydroxy-1-(4-(4-(2-hydroxy-2-methylpropionyl) benzyl) phenyl)-2-methylpropan-1-one) in 5% concentration called clear. The 3D printing system contains an LCD screen for projecting sliced images, a vat with non-adhesive treatment to deposit uncured resins and a motorized metal

building plate for the printed samples to be attached to. The LCD-SLA printing is a bottom-up 3D printing method and requires smaller volumes of resin during fabrication and can achieve a high vertical resolution and shorter curing time than other techniques, since the bottom of the resin is sealed from the oxygen-rich environment which inhibits the photocuring process.

3.4 3D printer scaffold preparation

After 3D printing, the scaffolds were immersed in bulk ethanol and placed inside an ultrasonic bath for 15min. Then, the ethanol was replaced by dH₂O and sonicated for another 15mins. This procedure was repeated several times until all the unpolymerized resin was completely removed followed by a UV curing step of 30mins. Finally, all the structure were kept in dH₂O until seeding. Due to high hydrophobicity the structures never let dry as no cells would be able to penetrate the pores during the initial seeding.

3.5 Nano dynamic Mechanical Measurement and Analysis (Nano-DMA)

The nanoscale mechanical measurements were carried out using Bruker's TI 950 TriboIndenter to conduct nano-DMA experiments, a dynamic testing technique equipped with Continuous Measurement of X (CMX) control algorithms that provides a continuous measurement of mechanical properties as a function of indentation depth, where X can be *hardness H*, *storage modulus E'*, *loss modulus E''*, *complex modulus E**, and the mechanical damping $\tan\delta$. The technique can be applied from ultrasoft hydrogels to hard coatings, with a greatly improved signal to noise ratio. Dynamic testing can be performed in a range of frequencies between 0.1 and 300 Hz. A quasi-static force, up to 10mN, is applied to the indentation probe while superimposing a small oscillatory force of 5mN maximum. A lock-in amplifier measures phase and amplitudes changes in the resulting force–displacement signal. To obtain the viscoelastic properties the material is modeled as two Kelvin–Voigt systems in parallel, with one end fixed and applying the indenters force to the other. This model requires four viscoelastic parameters to calculate the moduli of the material, providing highly accurate results compared to the simple Maxwell model or even the Standard Linear Solid.

3.6 Cell culturing

Different cell lines were used for seeding on the various scaffolds. Initially, mouse fibroblast cell line NIH-3T3 was used, which was maintained in a 5% CO₂ incubator at 37°C in standard Dulbecco's modified eagle's medium (DMEM) supplemented with 10% fetal

bovine serum (FBS) and 1% penicillin/streptomycin (p/s). For sterilization, the scaffolds fabricated on the coverslips were immersed for 30 min in 70% ethanol and then left to dry inside a UV chamber for 1h. Finally, they were placed in a 24-well plate and seeded with cells.

Furthermore, Mouse Bone Marrow Mesenchymal Stem Cells (BM- MSCs, Cyagen, California, USA) were used because they are of particular interest to doctors and researchers due to their potential to improve tissue engineering. Their attractiveness stems from their ease of isolation, manipulability, and potential for differentiation. It has been shown that these multipotent cells can differentiate into several cell types such as cartilage, bone, fat, muscle, tendon, skin, hematopoietic-supporting stroma, and nerve cells. In vivo, they are found in bone marrow, adipose tissue, periosteum, synovium, skeletal muscle, dermis, pericytes, blood, trabecular bone, human umbilical cord, lung, tooth pulp, and periodontal ligament [4]. The cells were incubated at 37°C in an atmosphere of 5% CO₂, in Low-glucose Dulbecco's Modified Eagle's Medium (LG- DMEM, Gibco, Invitrogen, Karlsruhe, Germany) supplemented with 10% heat inactivated Fetal Bovine Serum (FBS, Gibco, Invitrogen, Karlsruhe, Germany) and 1% penicillin/streptomycin (Gibco, Invitrogen, Karlsruhe, Germany). The 3D scaffolds were sterilized by immersing the coverslips in 70% ethanol and then drying under UV light for 1h. The sterilized scaffolds were placed in a 24-well plate (Sarstedt, Numbrecht, Germany), seeded with $5 \cdot 10^4$ cells/mL in a total volume of 1mL (p.3–4) and incubated at 37°C for 3 days in the same medium described above. Seeding took place after a confluent flask of 90%.

Lastly, murine Macrophages RAW 264.7 were used to seed the scaffolds fabricated with the Anycubic 3D printer. As an important cell type during both optimum tissue-implant integration and the pathologic process of implant failure, macrophages play a vital role in the host response to biomaterials [5]. The cells were incubated at 37°C in an atmosphere of 5% CO₂, in High-glucose Dulbecco's Modified Eagle's Medium (HG- DMEM, Gibco, Invitrogen, Karlsruhe, Germany) supplemented with 10% heat inactivated Fetal Bovine Serum (FBS, Gibco, Invitrogen, Karlsruhe, Germany) and 1% penicillin/streptomycin (Gibco, Invitrogen, Karlsruhe, Germany).

3.7 SBB treatment

By taking advantage of 2PA, two photon polymerization can occur when light is focused inside a photosensitive material and polymerizes it. One of those photoresins is SZ2080™ which, enables the fabrication of complicated structures with very little to no shrinkage after

development. The good mechanical properties are due to the dual organic-inorganic nature of this material and to the use of Michler's ketone (4,4'-bis(diethylamino)benzophenone), an excellent photoinitiator with a significant drawback: the high amount of autofluorescence. To address this significant drawback, alternatives have been used, such as the photobleaching of polymers (a temporary solution, as autofluorescence recovers after some hours of treatment) [6]; image processing, which includes artificially reducing the fluorescence background, reducing the same time the actual signal of the sample [7] and the use of infrared fluorophores which are not convenient due to the low number of machines able to detect the IR spectrum. A promising solution was photoinitiator free resins, but the main issue was extremely high fabrication time due to limited creation of free radicals and poor mechanical stability [8], [9]. Very recent work showed the reduction of autofluorescence by almost 80% by curing the polymeric scaffolds under a UV lamp for 2h [10].

Sudan Black B (SBB) [11] is an azobenzene-based dye widely used for the staining of lipids such as phospholipids, sterols and neutral triglycerides [12]. It has been shown elsewhere that SBB may initiate the MPL process [13], and that treating thin films with it may improve fluorescence imaging of biological samples, without affecting cell responses [14]. The molecular structure of SBB is comprised of 5 aromatic rings which are excellent molecular structures for photon absorption and 2 double covalent bonds between Nitrogen atoms. The energy from the absorbed photons is transferred to that bond, and similarly to the AIBN mechanism, gas form N_2 is created alongside with two radicals. The way that SBB may decrease the autofluorescence of polymers as suggested by Jaafar et al. [11] is either by absorbing the light emitted by the structures due to the molecule's high light absorption capacity, or by changing the refractive index of the material.

To eliminate any remaining autofluorescence, all structures and thin films were treated with SBB. More precisely, the samples were immersed in freshly made solution of 0.3% w/v SBB in 70% EtOH for 2h followed by several washings with EtOH until no remaining dye observed.

3.8 Live/Dead assay

To investigate the effect of SBB as a PI and as a treatment (0.3% w/v in EtOH) on cell viability, a live/dead assay was performed on an MSC culture (p.3–4), seeded on SBB treated thin films of the SBB-C composite. A total number of $10 \cdot 10^4$ cells were initially seeded on the films and cultured inside an incubator (5% CO_2 at $37^\circ C$) for 2 days. Cell viability was

examined by labeling live and dead cells using Live/Dead kit (Life Technologies, Carlsbad, CA, USA). Briefly, cells were incubated in PBS with ethidium homodimer-1 (EthD-1, 4 μ M) and calcein AM (2 μ M) for 40 min following the manufacturer's instructions. Live cells were labeled with calcein AM (green) and dead cells were labeled with ethidium homodimer-1 (red) and observed under an epifluorescence microscope (Carl Zeiss, Axioscope 2 Plus).

3.9 Scanning Electron Microscopy

The SEM is a microscope that creates images using electrons rather than light. Scanning electron microscopes have opened up new avenues of research in the medical and physical sciences since their introduction in the early 1950s by enabling researchers to analyze a wider range of specimens. SEM outperforms ordinary microscopes in many ways. The SEM has a wide depth of field, allowing for more of a specimen to be in focus at once. The SEM also offers significantly greater resolution, allowing for much higher magnification of closely spaced specimens. Because the SEM use electromagnets rather than lenses, the researcher has far greater control over the magnification level. All of these benefits, together with the very clear pictures, make SEM one of the most helpful research tools available today.

For the SEM to operate, an electron cannon produces an electron beam at the top of the microscope. The electron beam travels in a vertical route through the vacuum-sealed microscope. The beam is focused down toward the sample by passing through electromagnetic fields and lenses. When the beam contacts the sample, electrons and X-rays are emitted. These X-rays, backscattered electrons, and secondary electrons are collected by detectors and converted into a signal that is delivered to a screen similar to a television screen. This results in the final picture.

Because the SEM works in vacuum and employs electrons to create images, certain preparations must be made to the sample. Because water vaporizes in a vacuum, all water must be eliminated from the samples. All metals are conductive and do not need to be prepared before usage. All nonmetals must be made conductive by applying a thin coating of conductive material on the sample. This is accomplished by employing a device known as a "sputter coater." An electric field and argon gas are used in the sputter coater. The sample is put in a tiny vacuum-sealed chamber. An electric field and argon gas remove an electron from the argon, making the atoms positively charged. The argon ions are subsequently drawn to a negatively charged gold foil. The argon ions knock gold atoms from the gold foil's surface. These gold atoms descend and settle on the sample's surface, forming a thin gold covering.

To prepare samples for SEM imaging, $3 \cdot 10^4$ cells/well were seeded and cultivated for 5, 8, 12, 19 and 26 days. After the different timepoint, the cells were fixed using the cell fixation/preparation for SEM analysis protocol. In more detail, the culture medium was removed and the cover slips were washed twice with sodium cacodylate buffer 0.1 M (SCB). This buffer is used to ensure that cell membrane remains intact. Then, 4% w/v glutaraldehyde (GDA) in SCB was added followed by two washes with SCB. GDA fixes the cells as it is a dialdehyde and can rapidly react with protein by crosslinking and stabilizing all the amino-acids inside them [15]. Finally, the specimen was dehydrated in graded ethanol solutions (from 30% to 100%) for 5 mins each, underwent a critical point drying process (Baltec CPD 030) and 10 nm gold- sputter coat (Baltec CPD 030).

3.10 Immunofluorescence staining

Upon the end of cultivation time (both 3 and 4 days) the medium was removed and each well was washed three times with 1x Phosphate Buffered Saline (PBS, Gibco, Invitrogen, California, USA) followed by fixation with 4% w/v Paraformaldehyde (PFA, Sigma Aldrich, Missouri, USA) in PBS for 15 min. The cells were then permeabilized with Triton X-100 0.5% v/v (Sigma Aldrich, Missouri, USA) in PBS for 15 min, followed by blocking with 2% w/v Bovine Serum Albumin (BSA, Biofroxx, Einhausen, Germany) in PBS for 1h. Rabbit YAP antibody (Yes Associated Protein, YAP, 1:100 dilution, Cell Signaling Technology, Danvers, USA) was used to dye all the isoforms of YAP protein in 0.5% w/v BSA, 0.1% v/v Triton X-100 in PBS at 4°C overnight. The next day, TRITC- conjugated phalloidin-568 (EMD Millipore, Burlington, USA) (1:1,000 dilution) was used to dye the actin cytoskeleton alongside with CF488 anti-rabbit IgG antibody (Biotium, Fremont, USA, 1:500 dilution) in 0.5% w/v BSA 0.1% v/v Triton X-100 in PBS for 1h. Finally, the coverslips were placed upside down on a glass slide with slow fade mounting medium containing 4',6-diamidino-2-phenylindole (DAPI, Life Technologies, Carlsbad, CA, USA) and kept at 4 °C until observation. It should be noted that between each step the samples were washed thrice with 1x PBS. All steps of the procedure were carried out at RT, unless otherwise stated. An inverted Confocal Microscope (Leica SP8 inverted confocal, Leica Microsystems) was used for observation of all samples.

3.11 Differentiation medium

This medium contains all the reagents needed for the right stimulation of MSCs to differentiate into osteoblasts. More precisely, 49ml of normal LG-DMEM 10% FBS 1% p/s was used with 500 µl dexamethasone (0.01 µM), 500µl b-glycolic acid and 85µl l-ascorbic acid (50 µg/ml).

3.12 DAB staining

On day 0, 10^5 cells were seeded per scaffold in a 24-well plate. The plate was incubated for 7 days at 37°C. On day 7, the medium was removed and the sample was carefully washed once with PBS++ 1x and fixated with 4% Paraformaldehyde (PFA) at room temperature (RT) for 15 minutes. Then, the sample was washed 2-3 times with PBS 1x, treated with 400µl of 0.5% Triton x-100 in PBS 1x, and incubated at room temperature for 15mins. Following that, and after 2-3 washes with PBS 1x, BSA 2% was added and incubated at RT for 30 minutes. After that, the sample was washed 2-3 times with PBS and treated with Vinculin (mouse) in 0.1% BSA- 0.1% Triton at a ratio of 1:5000 and incubated at RT for 1 hour. Then, 0.05% H₂O₂ in PBS 1x was added and incubated in darkness for 10 minutes. The sample was thoroughly washed with PBS 1x and anti-mouse HRP in 0.1% BSA- 0.1% Triton at a ratio of 1:2000 was added and incubated at RT for 1 hour. Following 2-3 washes with PBS 1x, 500µl of Impact NovaRED diluent plus 8µl of Reagent 1, 5µl of Reagent 2, 5µl of Reagent 3 and 8µl of Reagent 4 were added and incubated for approximately 15 minutes, while checking via optical microscopy until signal developed. Then, the sample was washed with water for 5 minutes and incubated at RT for about 45 seconds with 500µl of Haematoxylin. Finally, the sample was rinsed with water until colourless, the mounting media was added and the sample was observed via a light microscope.

3.13 Confocal microscopy

Confocal microscopy, also known as confocal laser scanning microscopy is a powerful imaging optical technique that has a very high optical resolution and contrast by taking advantage of a pinhole that is able to block out- of- focus light. By capturing the 2D images from different depths the reconstitution of 3 dimensional images of the sample is enabled. This technique is very popular within multiple fields such as life sciences, semiconductors and materials sciences.

The principal of the confocal microscope was patented in 1957 by Marvin Minsky and aimed to overcome great limitation of the conventional fluorescence microscopes. In the case of confocal microscope, different lasers of various wavelengths are used. The beam is directed inside a galvanometric mirror system and then inside an objective lens. Then the sample is excited by a specific wavelength, leading to fluorescence in another. The galvanometric mirror then is directing the beam in 2 dimensions and the sample is scanned. Then a detector is placed on the other side of the sample, the emitted light is traced and the image is created. Afterwards, a stage moves the sample in Z axis and another 2D scan is created. By stitching all the different 2D scans, a large 3D reconstitution of the sample is formed with different colors corresponding to the light emitted by the fluorophores used to dye the proteins of interest.

For the confocal image analysis, the ImageJTM software was used. Firstly, the different z scans of the images were thresholded separately until all the cells were clearly visible. For the YAP analysis, the blue channel representing the nucleus was colocalized with the green channel representing the YAP protein through the AND procedure under image calculator. The same task was performed for the cytoplasmic YAP, but instead of AND the SUBTRACT command was used. The purpose of this procedure was to separate the signals coming from nucleus (nuclear YAP) and the cytoplasm (cytoplasmic YAP). Lastly all the intensities of each slice were calculated and graphed using either Microsoft Excel or OriginTM.

On the other hand, Runx2 protein intensities were calculated by thresholding and 3D counting all the intensities as the protein is localized only on the nucleus and not in the cytoplasm. All the intensities were then compared to the glass control and graphed through Microsoft Excel spread sheet program. All confocal experiments were carried out for $n=3$ different biological experiments.

3.14 Real time PCR analysis

One of the most important advantages of qPCR is its capacity to assess gene expression. Gene expression, which translates into mRNA synthesis, is an essential step in protein synthesis. For molecular biologists, gene expression is an active area of study that aids in the understanding of numerous biological pathways and diseases. The researcher uses reverse transcriptase to make complementary DNA (cDNA) copies of the RNA in their sample, and then uses that cDNA to perform qPCR. This is known as reverse-transcription polymerase chain reaction. The resultant measurements offer information regarding the quantity of mRNA present in the original, un-reverse-transcribed sample, which is otherwise impossible to

quantify. The type of data provided by a qPCR run is greatly influenced by the primers and dyes used. Because the dyes used in qPCR are typically nonspecific and will blend many genes into a single reading if numerous primers are used in the same mix, a single qPCR usually captures data on a single gene. However, it is feasible to "multiplex" qPCR to measure multiple DNA targets using fluorescent DNA probes rather of dyes, as long as each target's corresponding probe fluoresces at a separate frequency.

For the PCR experiments, total RNA was isolated from cells grown or differentiated for 1, 3 or 7 days using TRizol according to the manufacturer's instructions. More precisely, 1ml trizol for every sample was used to lyse the cells and extract the nucleic acids. Then, 200µl of chloroform was added and after centrifuging for 15mins, 12,000g at 4°C, the upper aqueous phase was transferred into a new tube. Then, 500µl of isopropanol was added followed by incubation in ice for 10mins and centrifuging for 15mins, 12,000g at 4°C. The supernatant was discarded, and the RNA was washed with 1ml Ethanol 75% and centrifuged again for 5mins, 7,500g at 4°C. Finally, the ethanol was discarded and the sample was let to dry. The RNA was then solubilized in 20µl dH₂O and the concentration was calculated through absorption at A260:280 using nanodrop. Two micrograms of total RNA from each sample were subjected to first-strand cDNA synthesis using the reverse transcription protocol. The PCR program used was: 3min at 95°C, then 35 cycles of 1min at 95°C, 30sec at 53°C, 30sec at 72°C and 10mins at 72°C. For the DNA electrophoresis, an 2.5% agarose gel was synthesized by dissolving 3 gr of agarose in 120 ml of TAE (40 mM Tris-acetate, 1 mM EDTA). Then ethidium bromide (EtBr) was added in a concentration of 0.5 µg/ml. DNA was let run for 30 mins at 100V.

The sequence of primers used are summarized in **Table 5**:

Table 5. Genes with their respective primer sequences.

Gene	Forward primer	Reverse primer
GAPDH	5' - TTAGCCCCCCTGGCCAAGG - 3'	5' - CTTACTCCTTGGAGGCCATG - 3'
RPI13a	5' - AGGGGCAGGTTCTGGTATTG - 3'	5' - TGTTGATGCCTTCACAGCGT - 3'
B2m	5' - CATGGCTCGCTCGGTGAC - 3'	5' - CAGTTCAGTATGTTCCGGCTTCC - 3'
Runx2	5' - GACTGTGGTTACCGTCATGGC - 3'	5' - ACTTGGTTTTTCATAACAGCGGA - 3'

For RT-qPCR, 25ng of cDNA were used for each reaction alongside with SYBR master mix and both primers for each gene. Then, all samples were run in qPCR (BioRad) according to the program: 5mins at 95°C, and then 45 cycles of 30 sec at 95°C and 40 sec at 53°C. All results were analyzed using the $\Delta\Delta C_t$ method.

References

- [1] A. Ovsianikov *et al.*, “Ultra-Low Shrinkage Hybrid Photosensitive Material for Two-Photon Polymerization Microfabrication,” *ACS Nano*, vol. 2, no. 11, pp. 2257–2262, Nov. 2008, doi: 10.1021/nn800451w.
- [2] D. Colombani, “Chain-growth control in free radical polymerization,” *Prog Polym Sci*, vol. 22, no. 8, pp. 1649–1720, Jan. 1997, doi: 10.1016/S0079-6700(97)00022-1.
- [3] A. Ovsianikov *et al.*, “Ultra-low shrinkage hybrid photosensitive material for two-photon polymerization microfabrication,” *ACS Nano*, vol. 2, no. 11, 2008, doi: 10.1021/nn800451w.
- [4] A. J. Rosenbaum, D. A. Grande, and J. S. Dines, “The use of mesenchymal stem cells in tissue engineering: A global assessment,” *Organogenesis*, vol. 4, no. 1, p. 23, 2008, doi: 10.4161/ORG.6048.
- [5] P. Neacsu *et al.*, “Reduced inflammatory activity of RAW 264.7 macrophages on titania nanotube modified Ti surface,” *Int J Biochem Cell Biol*, vol. 55, pp. 187–195, 2014, doi: 10.1016/J.BIOCEL.2014.09.006.
- [6] A. Piruska *et al.*, “The autofluorescence of plastic materials and chips measured under laser irradiation,” *Lab Chip*, vol. 5, no. 12, pp. 1348–1354, 2005, doi: 10.1039/B508288A.
- [7] M. Hintersteiner and M. Auer, “A two-channel detection method for autofluorescence correction and efficient on-bead screening of one-bead one-compound combinatorial libraries using the COPAS fluorescence activated bead sorting system,” *Methods Appl Fluoresc*, vol. 1, p. 17001, Mar. 2013, doi: 10.1088/2050-6120/1/1/017001.
- [8] K. Parkatzidis *et al.*, “Initiator-Free, Multiphoton Polymerization of Gelatin Methacrylamide,” *Macromol Mater Eng*, vol. 303, no. 12, p. 1800458, Dec. 2018, doi: 10.1002/MAME.201800458.
- [9] M. Lebedevaite, J. Ostrauskaite, E. Skliutas, and M. Malinauskas, “Photoinitiator Free Resins Composed of Plant-Derived Monomers for the Optical μ -3D Printing of Thermosets,” *Polymers (Basel)*, vol. 11, no. 1, Jan. 2019, doi: 10.3390/POLYM11010116.
- [10] B. N. L. Costa, R. M. R. Adão, C. Maibohm, A. Accardo, V. F. Cardoso, and J. B. Nieder, “Cellular Interaction of Bone Marrow Mesenchymal Stem Cells with Polymer and Hydrogel 3D Microscaffold Templates,” *ACS Appl Mater Interfaces*, vol. 14, no. 11, pp. 13013–13024, Mar. 2022, doi: 10.1021/ACSAMI.1C23442/ASSET/IMAGES/LARGE/AM1C23442_0005.JPEG.

- [11] I. H. Jaafar, C. E. Leblon, M. T. Wei, D. Ou-Yang, J. P. Coulter, and S. S. Jedlicka, “Improving fluorescence imaging of biological cells on biomedical polymers,” *Acta Biomater*, vol. 7, no. 4, pp. 1588–1598, Apr. 2011, doi: 10.1016/J.ACTBIO.2010.12.007.
- [12] O. B. Bayliss High, “The histochemical versatility of Sudan Black B.,” *Acta Histochem Suppl*, vol. 24, pp. 247–255, 1981.
- [13] A. J. G. Otuka *et al.*, “Three-dimensional structures fabricated after laser-induced free radical generation in azoaromatic compounds,” *Opt Mater Express*, vol. 10, no. 8, pp. 1792–1800, Aug. 2020, doi: 10.1364/OME.397716.
- [14] A. Maggi, H. Li, and J. R. Greer, “Three-dimensional nano-architected scaffolds with tunable stiffness for efficient bone tissue growth,” *Acta Biomater*, vol. 63, pp. 294–305, Nov. 2017, doi: 10.1016/j.actbio.2017.09.007.
- [15] S. al Shehadat, M. O. Gorduysus, S. S. A. Hamid, N. A. Abdullah, A. R. Samsudin, and A. Ahmad, “Optimization of scanning electron microscope technique for amniotic membrane investigation: A preliminary study,” *Eur J Dent*, vol. 12, no. 4, p. 574, Oct. 2018, doi: 10.4103/EJD.EJD_401_17.

Chapter 4

4 Results

The results are organized in a timeline manner beginning from the design and the mechanical simulations of the various structures, the fabrication and characterization of them and in the end all the biological experimental results ranging from simple cytotoxicity to cell differentiation. **Figure 17** depicts the three basic designs used in the studies. Firstly, the *Auxetic bowtie* was created as it is one of the most fundamental negative poison ratio structures widely used. Secondly, the variation of the bowtie scaffold called *Auxetic v.2* was designed to provide a friendlier cellular environment. Lastly, the opposite mechanical environment of the ultra-stiff ultralight structure called *Kelvin foam* was selected as a comparison to the negative poison ratio. The unit cells of each scaffold are represented in black for the reader to distinguish them more straightforwardly.

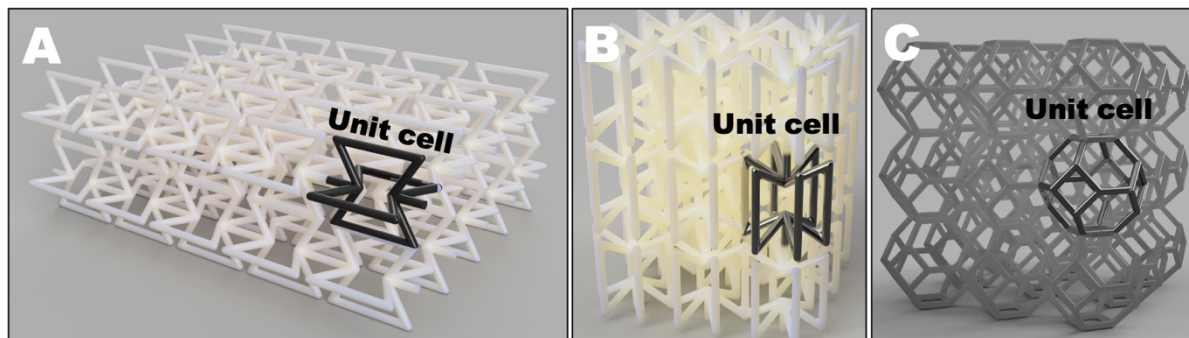


Figure 17. Photorealistic renders of the fabricated scaffolds made with fusion 360. **A)** Auxetic bowtie **B)** Variation of the original bowtie design called Auxetic v.2 **C)** Kelvin foam. The unit cells of each scaffold are represented in black.

4.1 Mechanical simulations

4.1.1 Auxetic bowtie

The auxetic bowtie structure is the first geometry tested and fabricated. It derives from the hexagonal honeycomb design which is found in nature by changing the 4 of the 6 angles to be less than 90° . In that way, the axial force pushes those angles inwards thus buckling the surrounding beams and making the central nod to move inwards. For the needs of the simulation, a $3 \times 3 \times 3$ lattice was made using the fusion 360 software. Epoxy resin was used as the simulation material as its properties were closer to the properties of SZ2080TM resin

(chapter 5, section 2: *Characterization of the mechanical properties of the photoresin SZ2080*). More specifically, this material has a young modulus of 4.64 GPa and a positive poison ration of 0.39, yield strength of 12.4 MPa and Ultimate tensile strength of 24 MPa. An axial force of 100N was applied to the top row of unit cells with a vertical direction pointing downwards as illustrated in **Figure 18** with the blue arrows. The structure in its maximum displacement bended inwards confirming the negative poison's ratio. Moreover, the maximum stress that the structure experienced was 22.85MPa in the Von Mises scale.

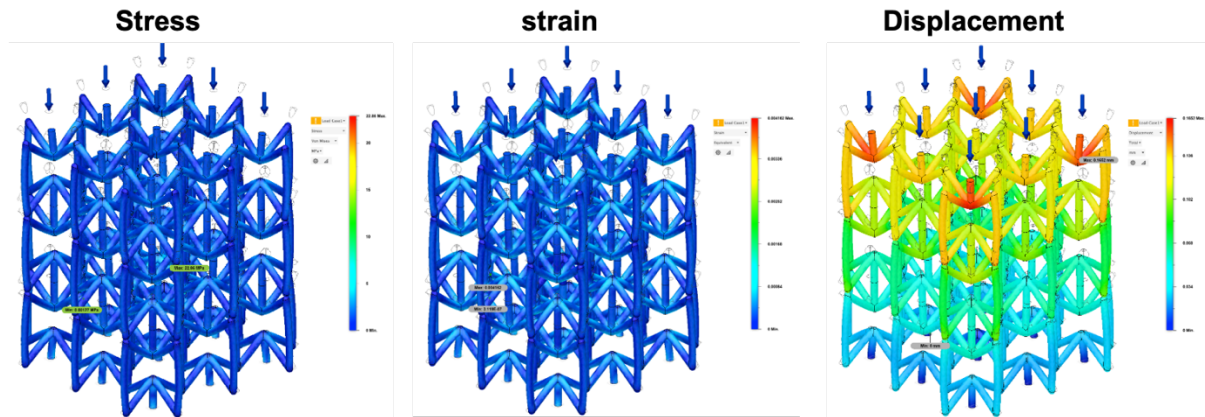


Figure 18. Mechanical simulation of the Auxetic bowtie scaffold showing stress, strain and displacement. The simulation was done on a lattice 3x3x3 with totally 27 unit cells. The bottom was fixed and an axial force facing downward was applied on the top part of the top row of unit cells.

4.1.2 Kelvin foam

The geometry tetrakaidecahedron also known as kelvin foam was fabricated from the basic honeycomb hexagonal which is the simplest 2D foam of bubbles of equal area. As in Auxetic scaffold, the simulation material was chosen to be epoxy resin. **Figure 19** shows the simulation results, where stress, strain and displacement are shown. The same material as before was used as well as the same axial force of 100N. As we can see from the displacement, the structure became thicker due to the force, confirming the positive poison's ratio. Also, being an ultra -stiff structure, it was able to withstand up to 3.10^7 MPa of strain in Von Mises scale.

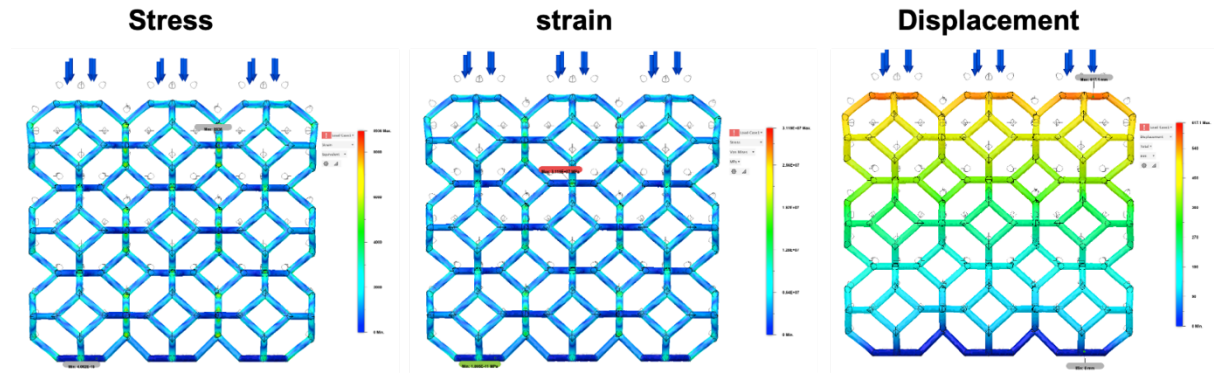


Figure 19. Mechanical simulation of the Kelvin foam structure showing stress, strain and displacement. The simulation was done on a 3x3 lattice with totally 9 unit cells. The bottom was fixed and an axial force facing downward was applied on the top part of the top row of unit cells.

4.1.3 Auxetic v.2 scaffold

After the original design of the Auxetic bowtie v.1 model we moved to the optimization and design of a new architecture called Auxetic v.2. This design features a brand-new geometry that aims to create a much larger contact area of both the cells and the substrate, ensuring max stability and is based on the original designed, rotated 45° in y axis. In that way the unit cells were able to have 2 points of contacts with the substrate thus increasing their stability. Moreover, we introduced an extra horizontal bowtie plane so that more contact points can be created for the cells to attach to. So, it was crucial to prove that the new design keep the auxetic properties by simulating its behavior under a constant axial force (**Figure 20**). The axial force was applied on the top of the scaffold as depicted from the vectors in **Figure 20** and had a magnitude of 100N. This force was chosen to be applied on the top part of the unit cell and not on its bowtie beam as it would more realistically represent the forces applied from the cells in a cell culture. Moreover, the displacement of the scaffold shows the auxicity as it shrunk due to the applied force.

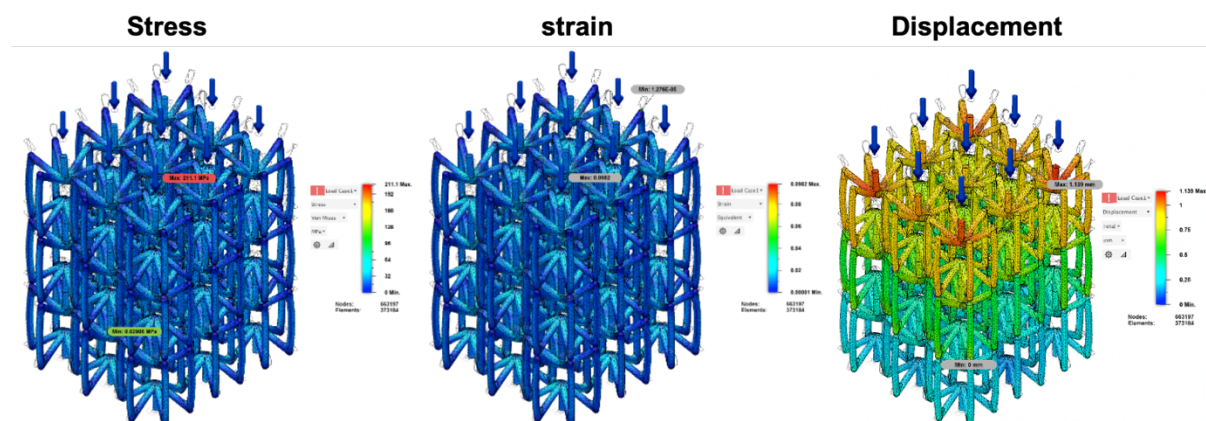


Figure 20. Mechanical simulation of the Auxetic v.2 scaffold showing stress, strain and displacement. The simulation was done on a lattice 3x3x3 with totally 27 unit cells. The bottom was fixed and an axial force facing downward was applied on the top part of the top row of unit cells.

4.2 Characterization of mechanical properties of the photoresin SZ2080

Materials used in MPL are viscoelastic, exhibiting both elastic and viscous behavior when deformed. Elasticity is a result of bond distortion when the material is stressed. Elastic deformation occurs almost instantly and the material returns to its original length when the stress is removed. Viscosity is attributed to larger scale rearrangements of molecules inside the material. These molecular allocations depend on the duration of the stress and are not necessarily reversible. In order to consider both responses, dynamic tests were performed on structures fabricated with MPL, in which sinusoidal stress is applied on them and the resulting strain is recorded. Stress and strain will both oscillate with the same frequency, but with the former displaying a phase delay, the magnitude of which depends on how viscous the material is. It is convenient to handle stress as complex quantity whose real and imaginary parts are, respectively, in and out of phase with the strain. The ratio of in-phase stress to strain is used to define storage modulus E' , which represents the elastic portion of the material's response, while the ratio of out-of-phase stress to strain is the loss modulus E'' , which represents the contribution of viscosity to the material's response. Identifying storage and loss modulus greatly of the bulk material is crucial to accurately model and simulate the mechanical response of architected scaffolds.

Two geometries were considered for the characterization of the material's mechanical properties: rectangular boxes ($40 \times 50 \times 40 \mu\text{m}$) and upright cylinders (radius of $4 \mu\text{m}$ and

height of 80 μm) (**Figure 21**). Arrays of such structures were fabricated with a variable laser fluence ranging from 90 to 150 mJ.cm^{-2} at a constant scanning speed of 10 $\mu\text{m.s}^{-1}$. For each geometry, eight arrays were prepared to consider for statistical errors. The boxes were measured using the nano-DMA to extract the storage and loss modulus, as well as the hardness of the material as a function of laser fluence during fabrication. The nano-DMA oscillation frequency ω was 220 Hz for all measurements. The upright cylinders were used in in situ SEM—microindentation experiments to measure the material's Poisson's ratio. For the nano-DMA, a 50 μm diameter spherical probe was employed, while for the micro-indentation experiments, a 10 μm flat punch was utilized.

The storage modulus E' , loss modulus E'' and hardness H were graphed separately as a function of laser fluence. In the vicinity of 110 mJ.cm^{-2} there appears to be an abrupt jump in all three graphs for their respective y-axes. Especially loss modulus and hardness graphs appear to transition from one constant value to another during this sudden increase. This step-function behavior can be attributed to the polymerization threshold and the polymer writing strategy which was followed: the motors use a line-by-line hatching strategy to write each structure, where the distance between each line is ≈ 200 nm. So, between two parallel lines, the distance between the center of the focus of the laser beam is ≈ 200 nm. At the same time, within the line, as the 80 MHz laser is scanned at a speed of 10 $\mu\text{m.s}^{-1}$, the distance between consecutive laser pulses is in the order of 1 pm. The test samples therefore consist of very densely cross-linked plates, while the material holding together these plates is less dense with its cross-linking density being dependent on the photon flux received. Above a certain laser fluence, which in this case at approximately 110 mJ.cm^{-2} , the cross-linking density reaches a saturation point, after which it can no longer increase.

SZ2080's Poisson's ratio was calculated from its original definition by measuring the cylinders' dimensions before and after deformation and was found to be independent of laser fluence with a constant value of 0.490 ± 0.002 .

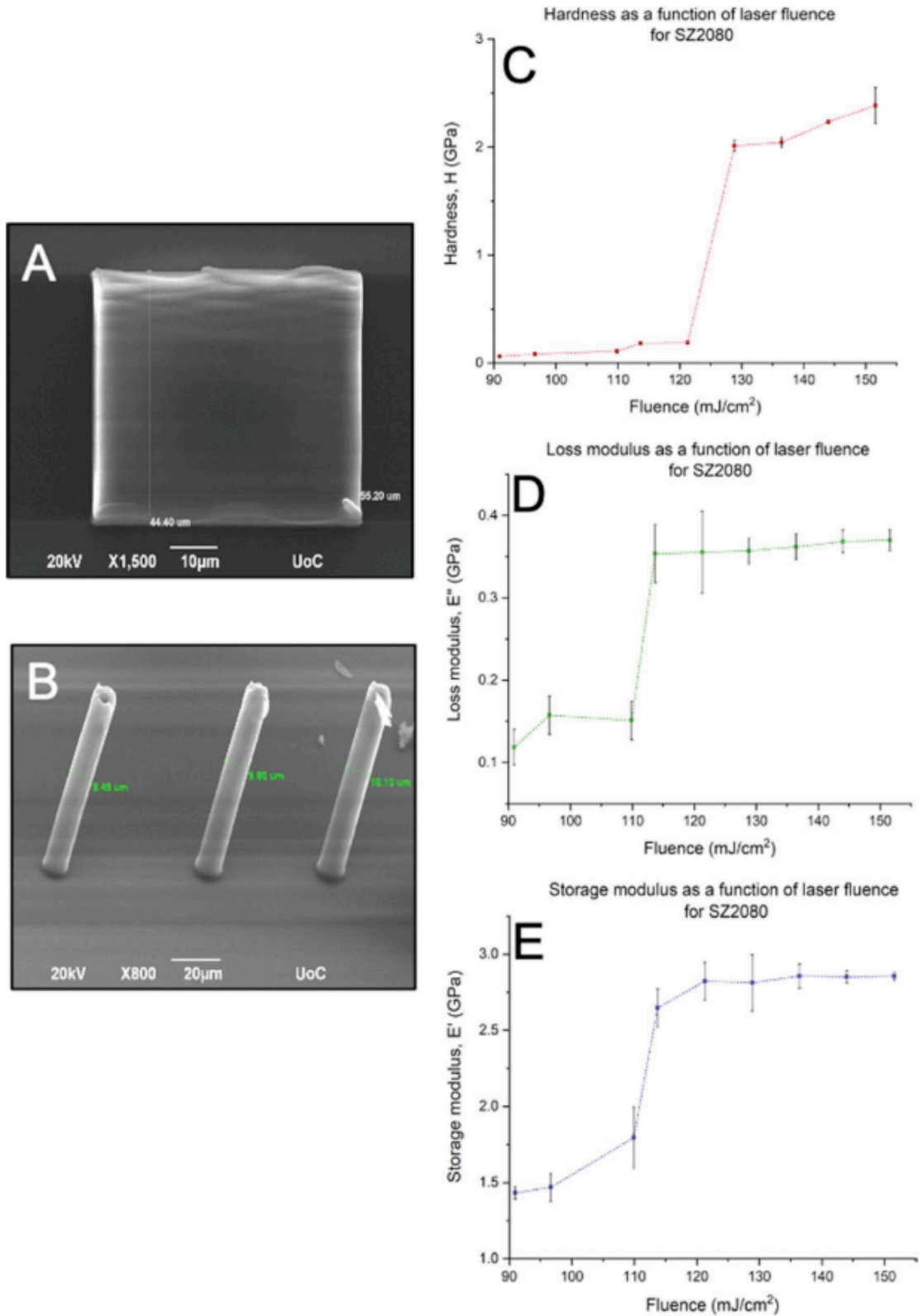


Figure 21. A,B) Scanning electron microscopy (SEM) images of the boxes and the cylinders used for the calculation of the mechanical properties, C) Hardness, D) loss modulus, E) storage modulus as a function of laser fluence. There is an abrupt jump at the vicinity of $\approx 110 \text{ mJ}\cdot\text{cm}^{-2}$ in all three graphs attributed to the polymerization threshold and the writing strategy followed.

4.3 Fabrication of the bowtie Auxetic scaffold

The bowtie is probably the most thoroughly investigated auxetic geometry. It has been widely studied in 2D, to make meshes for stents, as well as for studying auxetics in sports safety equipment. By rotating each angle of the traditional honeycomb hexagonal design, we were able to create the unit cell of the auxetic scaffold. Two orientations may be used: the *vertical* and the *horizontal*. The vertical orientation (**Figure 22**) was used as a reference to standard the condition of the fabrication, whereas the horizontal was chosen for the cell studies, as this is the orientation that cells must have for tissue engineering applications. There were totally 4 scanning speeds used (40, 60, 80 and 100 $\mu\text{m.s}^{-1}$) and 6 energies (11, 12, 13, 14, 15, 16 mW *measured before the objective lens*) creating a 4X6 matrix. 24 structures in total were evaluated for their integrity and resolution via Scanning Electron Microscope observation. The structures that were fabricated with large power but lower scanning speed had the thickest lines, asset that is crucial for a good mechanical scaffold. On the other hand, the structures that were fabricated using lower power and high scanning speed collapsed as the formation of free radicals derived from the photoinitiator weren't sufficient for the polymerization process.

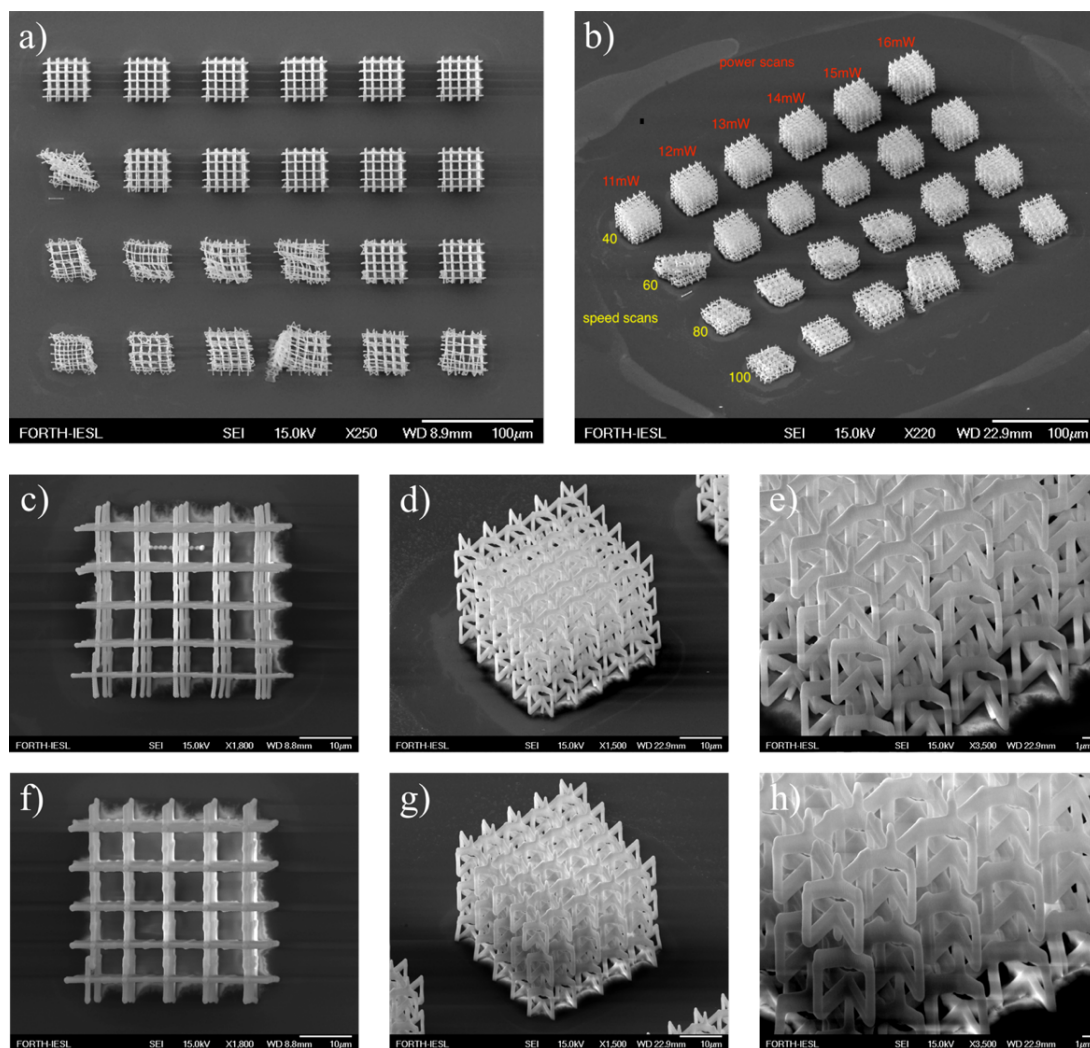


Figure 22. Scan/power matrix map of the vertical orientation bowtie scaffold. Sufficient fluence and low scanning speed result in higher radiation dose leading to mechanically stable structure, while inefficient ones lead to collapse. **A)** top view. **B)** tilted view, **C, D, E)** Structure fabricated with 11mW and 40 $\mu\text{m.s}^{-1}$. **F, G, H)** structure fabricated with 16mW and 40 $\mu\text{m.s}^{-1}$

For the cell studies, we fabricated the horizontal orientation scaffolds with two different unit cell sizes: **8.6 μm** and **40 μm** . Each size corresponds to the length of the top line of the bowtie unit cell as well as the height of it. The 8.6 μm unit cell size (*small pore-size scaffold*) was used for mechanical evaluation and 2D cell cultures, whereas the 40 μm unit cell (*large pore-size scaffold*) for 3D cell cultures. All scaffolds were fabricated using the ‘nano setup’ described below (*materials and methods section*).

The structures used to investigate the mechanical properties of the bowtie scaffold are shown in **Figure 23**, where the computer-aided design (CAD) model of the structure is compared to the SEM images. There is close matching between the experimental structure and the CAD model, since the unit cells are consistent and well-defined. Its auxetic behavior was investigated

using the Hysitron PI 88 SEM PicoIndenter, enabling in situ mechanical testing and observation of the tested samples. Multiple videos of the mechanical tests were recorded to show the deformation of the scaffolds. **Figure 24** shows that under compression, the scaffold shrinks homogeneously, without cracking until 60% deformation, thus demonstrating the auxetic behavior. A representative force displacement curve is presented in **Figure 24G**. While there is no fracture until 60% load, the curve has an undulated profile which is associated with the reconfiguration of the structure due to internal compression, altering the contact between the structure and the indentation tip. This reconfiguration occurs through the whole loading cycle, leading to instability of the structure due to buckling at 26% deformation (e.g. the slope of the curve becomes negative), causing large deformations and fracture at 60% (**Figure 24C**). These results reveal that the structure can sustain large deformations, shrinking during compression, and reconfiguration during loading, elucidating its utility as a bioengineering scaffold. The imaging of the tested samples also confirms the simulation results of 3D model created using the 2020 R1 academic version of ANSYS software, where a virtual axial force was applied on top of the scaffold, compressing it in all directions. The CAD simulation was made using ANSYS Design Modeler and the scaffold had 1350 nodes and 720 elements. The material used for the simulation had a young's modulus of 200GP and Poison's Ratio of 0.3.

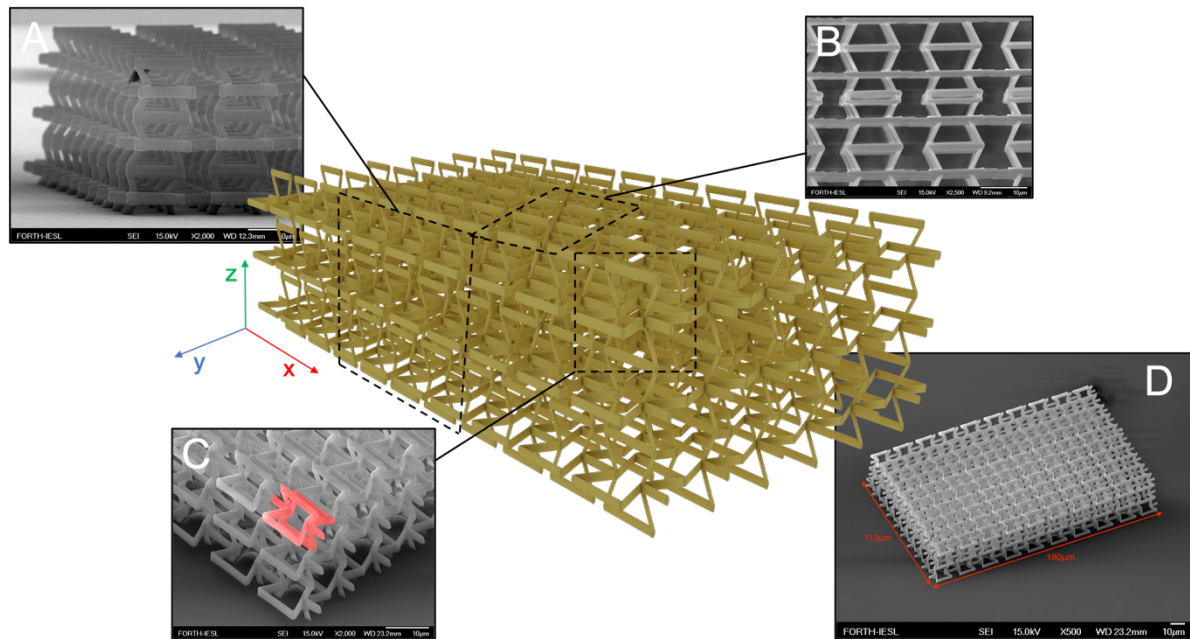


Figure 23. Scanning electron microscopy (SEM) images of the bowtie auxetic scaffold with X axis direction small pore size (8.6 μm) in comparison with the computer-aided design (CAD) model (designed in 3DS max2020). **A)** tilted view of the scaffold, **B)** top view, **C)** zoomed photo of the one edge of the scaffold. The red color was added in photoshop to make the bowtie unit cell clearer, and **D)** tilted view of the whole scaffold.

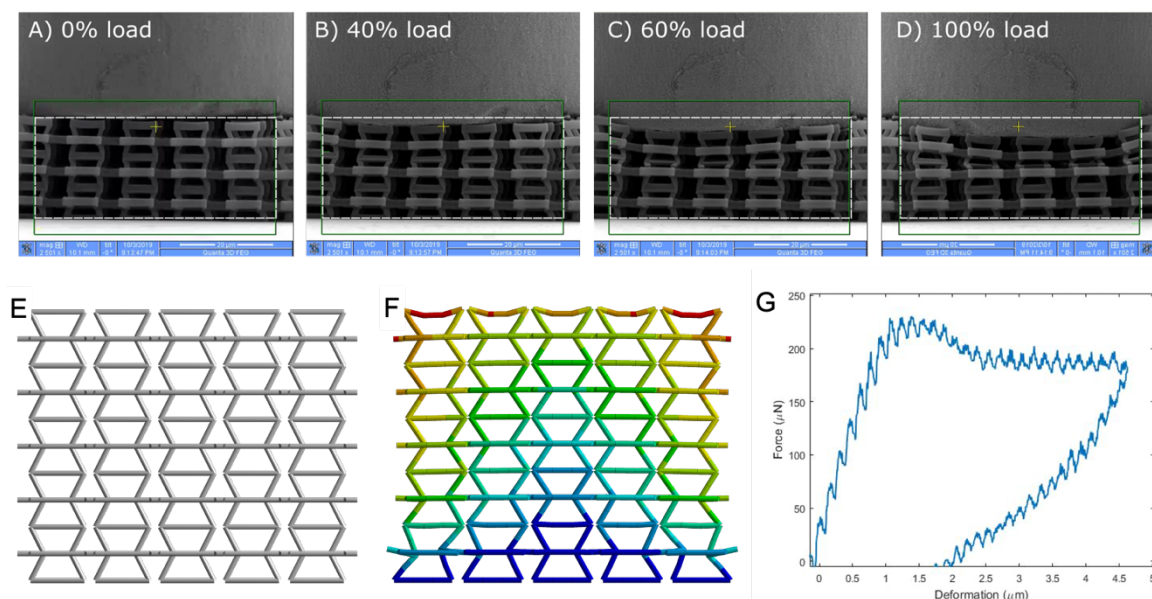


Figure 24. Microindentation scanning electron microscopy (SEM) pictures of the bowtie design. The white dashed box represents the initial uncompressed form of the scaffold. **A)** Uncompressed scaffold, **B)** at 40% load, some deformations are starting to be visible, **C)** 60% load, and **D)** at 100% load, the first layer of the scaffold is completely compressed and touches the lower one without cracking. **E)** 3D computer-aided design (CAD) design of the scaffold using ANSYS. **F)** Deformation of the scaffold while applying axial force on the top. The colors represent the total strain each node undergoes (red: maximum, blue: minimum). **G)** Diagram of the load in correlation to the indentation depth.

4.4 NIH-3T3 fibroblast cell line interactions with the Auxetic scaffold

The bowtie structure with the small pore size was initially used as a cell substrate. This pore size is too small to allow cell penetration; however, it is useful in order to investigate the ability of fibroblasts to adhere and proliferate on the scaffold and to adapt and deform it. All the cells were able to create filopodia, adhere on the surface as well as the sides of the scaffold (**Figure 25**) and pull the whole structure. We observed major deformations of many unit cells of the scaffold, as well as buckling around and on the scaffold. This was a very promising first indication that a hard and stiff material like SZ2080 can become soft and elastic only by tuning its geometry. Furthermore, no cell damage or cytotoxicity was observed.

In order to allow cell penetration and proliferation inside the scaffold, we built scaffolds with a large pore size of 40 μm, comparable to the size of a single cell (mouse fibroblasts have a diameter of $\approx 40\text{-}50\mu\text{m}$). Each scaffold consisted of two layers. To make the scaffold mechanically stronger, each line was 3D printed three times (scanning speed $100\mu\text{m.s}^{-1}$ with a laser fluence of 131mJ.cm^{-2}) with each line separated by 0.5 μm. After 4 days of cells in

culture, SEM pictures showed that they were able to enter into the pores of the scaffold and successfully proliferate (**Figure 26**). The structure seemed to be completely occupied by cells and deformed, especially on the one side which is completely flat (**Figure 26B**). Compared to cells growing on the glass, cells that grow inside the scaffold seem to have proliferated more and be more directional due to the fact that the unit cell itself is designed in X-axis. It is clear that the 3D culture with auxetic properties is more efficient than the 2D in terms of both proliferation and directionality. This design is ideal for cell types that require environments with well-characterized mechanical properties and directionality.

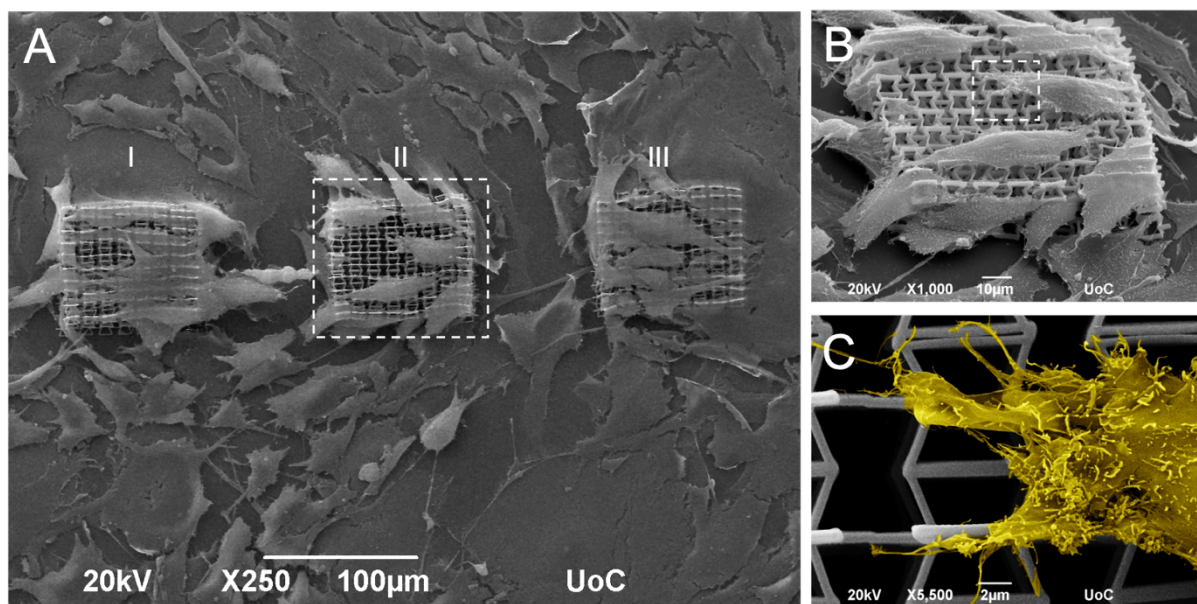


Figure 25. Culture of NIH-3T3 on small pore size auxetic scaffolds (I through III). **A)** General view of the three scaffolds where major deformations can be observed due to the mechanical forces applied by the fibroblasts. Due to the plasticity of the material, the scaffold is able to bend and deform without breaking, thus mimicking the mechanical properties of the extracellular matrix while providing the cells with an X axis directionality. **B)** Magnified image of the second scaffold. **C)** Further magnification of the filopodia of a single cell (yellow pseudo color).

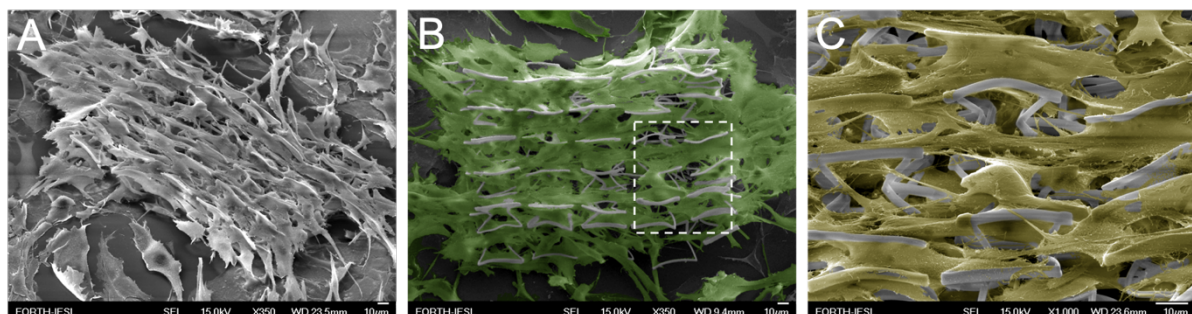


Figure 26. Culture of NIH-3T3 on large pore size auxetic scaffold. A) General tilted views of the auxetic scaffold with the large pore size. It is obvious that the cells were able to penetrate inside the pores of the structure making it the first 3D culture of an auxetic scaffold. The structure consisted of two layers and was able to withstand the forces. B) Top view of the scaffold with green colored cells (green pseudo color). C) Zoomed picture of several unit cells on the surface of the scaffold. The bowtie geometry is able to bend inwards because of the mechanical forces applied by the cells (Yellow pseudo color).

4.5 High polymer autofluorescence inhibits the use of advanced imaging methods

We used the large pore size scaffolds and the same culturing conditions as previously described to observe the cell-loaded scaffolds under the confocal microscope and take multiple z-stacks. In **Figure 27**, the confocal images are displayed with z-stacks overlaying one another in two different channels. The blue channel represents the DAPI dyed nuclei, whereas the red channel represents the actin filaments of the cytoplasm. As we observed, the scaffold's autofluorescence in both channels is so high that it makes it very difficult to distinguish the cells inside. Nevertheless, with some small image adjustments, we were able to spot the cells at the bottom of the scaffold (layer of unit cells attached on the glass), as well as some others inside higher unit cells, thus showing that the cells are actually capable to exploit their 3D microenvironment.

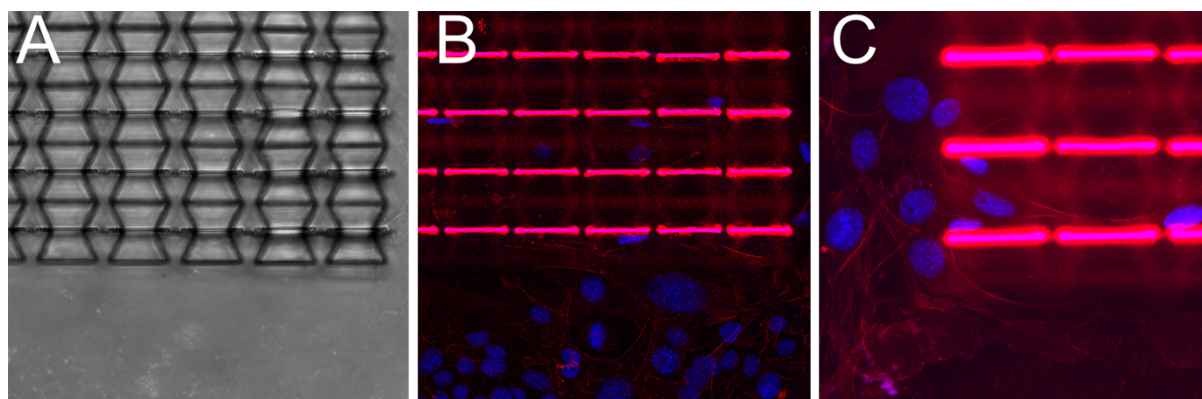


Figure 27. Confocal images of the large pore size scaffold with the fibroblasts. **A)** Brightfield image of the scaffold using a 20× objective lens, in which the cells are not visible. **B)** The same image with an overlay of the red and blue fluorescence channels. **C)** Image taken with a 40x objective lens showing the corner of the scaffold where a higher cell density was observed. The focal point in all images is on the bottom part of the scaffold.

4.6 Unlocking the confocal potentials: the Sudan Black B photoinitiator variant of SZ2080

Multiphoton lithography allows the high resolution, free-form 3D printing of structures such as micro-optical elements and 3D scaffolds for Tissue Engineering. A major obstacle in its application in these fields is material and structure autofluorescence. Existing photoresists promise near zero fluorescent in expense of poor mechanical properties, and low printing efficiency. Sudan Black B is a molecular quencher used as a dye for biological studies and as means of decreasing the autofluorescence of polymers. In this approach we reported the use of Sudan Black B as both a photoinitiator and as a post-fabrication treatment step, using the zirconium silicate SZ2080TM for the development of a non-fluorescent composite

The material employed for MPL fabrication is the organic-inorganic hybrid material SZ2080TM, reported previously [1]. Two photoinitiators were used in this study: SBB, for the fabrication of low-autofluorescence 3D structures, and 4,4'-bis(diethylamino) benzophenone (Michler's ketone), as a control. For brevity, the SBB-photosensitized composite will be called SBB-C, while the Michler's ketone -photosensitised composite will be called BIS-C.

To test the overall fluorescence of the new material SBB-C, a series of 3D woodpile scaffolds were fabricated employed both SBB-C and BIS-C as a control. These scaffolds were designed using the CAD software Fusion 360 (Autodesk, California, USA) to have dimensions 320 μ m x 264 μ m x 80 μ m.

We obtained fluorescence and SEM images of scaffolds fabricated with BIS-C and SBB-C before and after SBB treatment, at the red, green, and blue channels. The results are presented in **Figure 28**. Column (a) shows fluorescent images of scaffolds made using the BIS-C hybrid. Scaffold autofluorescence was so high that the green channel penetrated the blue one, making the scaffold glow green in both channels (exposure: 500ms). Even after treatment with SBB (column (b)), autofluorescence is very high, for the same exposure time. The SBB-C hybrid exhibits much lower autofluorescence (column (c)); any residual autofluorescence is most likely due to ZrO₂ nanoparticles formed in the resin during photopolymerization. In column (d) we show scaffolds fabricated using the SBB-C hybrid, and subsequently treated with SBB. Note that the camera exposure is 10,000ms, as a 500ms exposure was not sufficiently long for the scaffolds to be visible. Even at this longer exposure, autofluorescence levels are negligible and the scaffolds were barely visible, highlighting the efficiency of the SBB-C/SBB treatment combination. Column (e) shows SEM images of the SBB-C scaffolds and their surface before and after SBB treatment. It is clear that the SBB treatment does not damage or in any way

affect the integrity of the scaffolds. Furthermore, the high magnification SEM image (15,000x) shows that the SBB treatment leads to much smoother surfaces, where SBB has been adsorbed inside the polymer pores, as proposed by Jafaar et al [2]. It was obvious that a change on the polymeric surface may affect the wettability. So, after fabricating the kelvin foam we tested the wettability before and after the treatment with SBB through water contact angle measurement (**Figure 29**). Before treatment, the scaffold remains transparent and has a contact angle of 136° which places it in the hydrophobic area. However, after the treatment, the color of the scaffold changes to black and the contact angle changes to 92° thus making the structure hydrophilic.

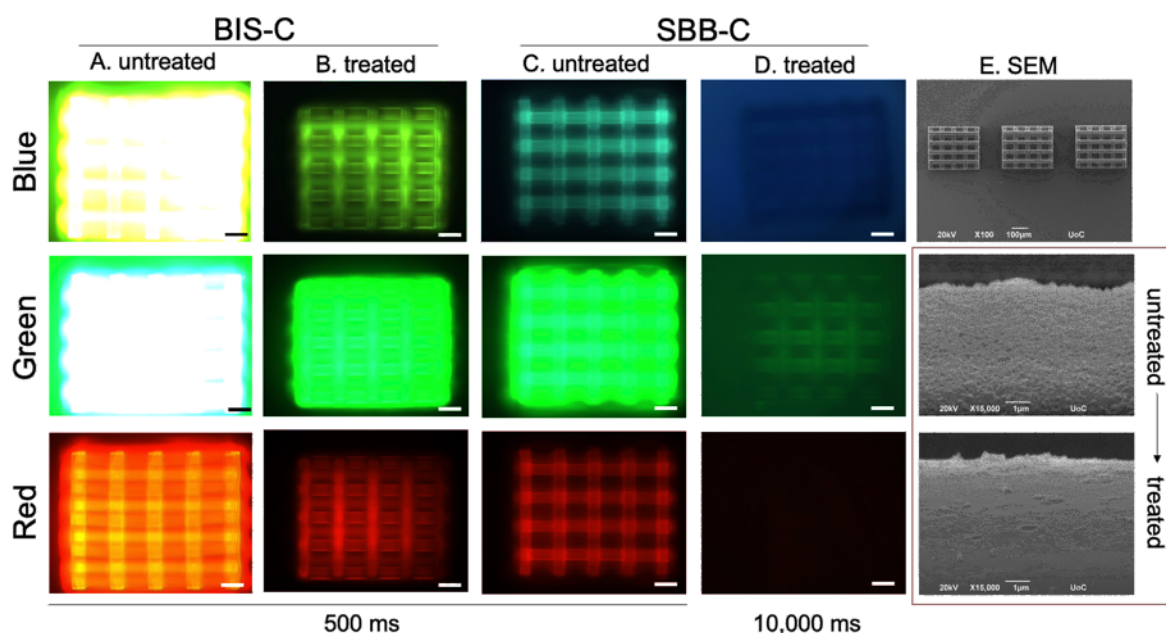


Figure 28. Comparative study of the fluorescence of BIS-C and SBB-C. Untreated scaffolds demonstrated the highest fluorescence, while treated SBB samples exhibited minimum fluorescence. The last column depicts SEM images of the scaffolds in top. Further magnification 15,000X reveals the effect of treatment on the polymer. Scale bar corresponds to $50\mu\text{m}$.

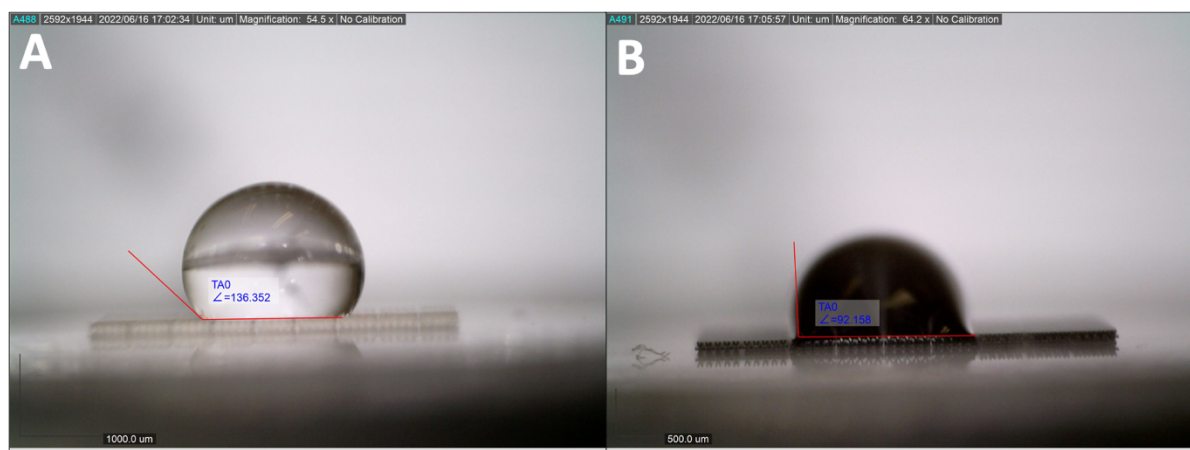


Figure 29. Wettability testing of the Kelvin foam A) before and B) after SBB treatment. The scaffold before treatment is super hydrophobic with a contact angle of 136° , while after treatment it becomes almost hydrophilic with a contact angle of 92° .

This effect was further investigated using the ImageJ software where the mean fluorescence intensities were measured (**Figure 30**). Green and blue color of BIS-C, untreated samples demonstrated the highest intensities of 250au while the red color showed a much lower intensity at around 150au. Treatment with SBB lowered the intensities of the BIS-C samples to comparable levels to the SBB-C untreated ones. Further treatment of SBB-C samples eliminated fluorescence almost completely. It is remarkable that almost 90% autofluorescence reduction between BIS-C untreated and SBB-C treated samples was observed.

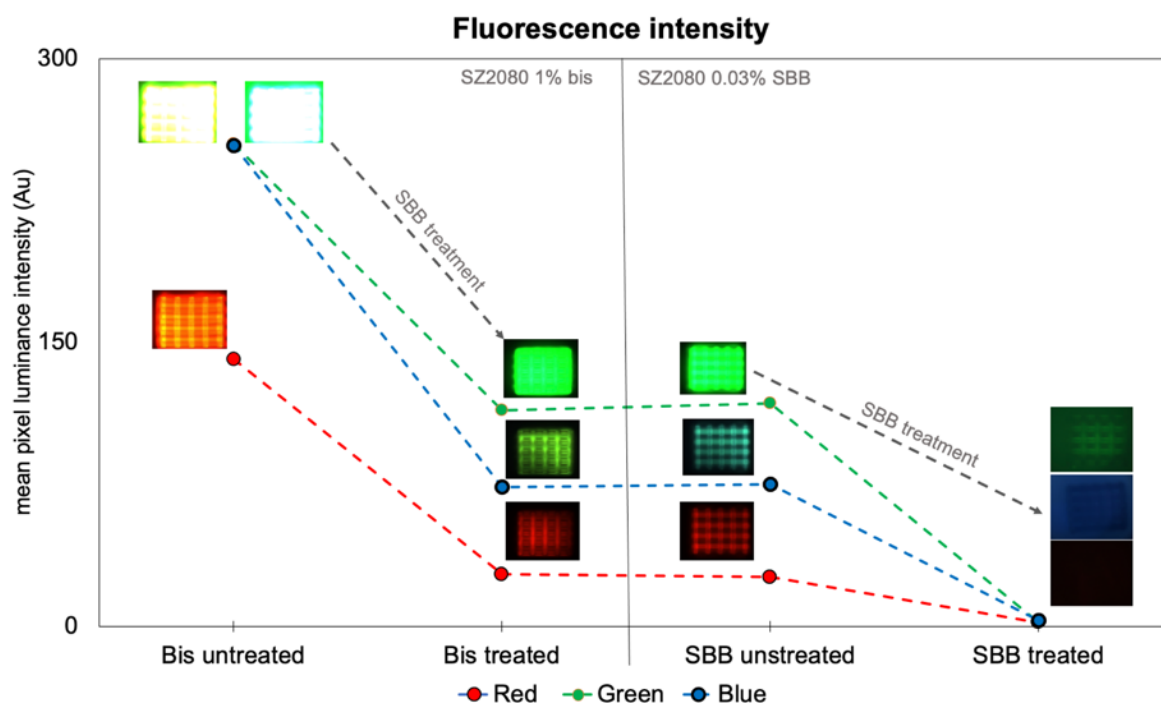


Figure 30. Fluorescent intensities of BIS-C and SBB-C samples. Exposure time was set at 500ms with the exception of SBB treated samples, where exposure time was set at 10,000ms due to the inability to observe the scaffolds at lower exposure times. Remarkably, Bis treated and SBB untreated samples exhibit comparable intensities, whereas the intensities of SBB treated samples at 500ms would be almost zero.

4.7 SBB cell study in simple geometries

As discussed earlier, the low autofluorescence of the SBB-C hybrid makes it an ideal material candidate for 3D scaffold fabrication, for the investigation of 3D cell cultures using fluorescence techniques. To this end, the woodpile geometry was chosen as our initial scaffold

fabrication, as it provides both complexity and large surface areas for cells to grow on. After 3 or 4 days of culture, MSCs reached confluence of 90% and for their staining were used three different dyes that fluoresce at different wavelength. More specifically, we used DAPI dye fluoresce at 358nm for the nucleus staining and the FITC conjugated phalloidin 568 as a high-affinity filamentous actin (F-actin) probe. Finally, the secondary anti-rabbit green (488 nm) conjugated antibody utilized to detect the primary YAP antibody (YAP) that was previously bound to the YAP protein isoforms. Each one corresponds to blue, red and green channels respectively. There were 4 different scaffolds prepared in total; woodpiles fabricated with BIS-C both treated and untreated with 0.3% SBB, and woodpiles made with SBB-C both treated and untreated with 0.3% SBB. It should be noted that the treatment took place right before cell seeding for 1h in Room temperature (RT).

Figure 31 clearly demonstrates the suitability of the SBB-C hybrid for scaffold fabrication regarding cell growth for various types of 2D and 3D studies. Cells show good survival rates, comparable with already established biomaterials such as gelatin methacryloyl (GELMA) hydrogels [3], poly(lactide-co-glycolide) (PLGA), polycaprolactone (PLA) etc. [4], this is backed up by the live/dead assay results (**Figure 31 I, J**). It can be seen that cell viability reached 99%. This is not surprising, as both the zirconium silicate and SBB are known to show good compatibility with cells [5].

Using the SBB-C for scaffold fabrication, and subsequently treating these scaffolds with SBB allowed us to eliminate scaffold autofluorescence. During confocal microscopy imaging, cells can be clearly distinguished both inside the pores of the scaffold and on its surface. The significance of these results is profound, as scaffold autofluorescence has been identified as a major hurdle in employing confocal microscopy in 3D cell studies [6]. Natural cell environments are three-dimensional and information gained from 2D or 2.5D studies may only be partial or incomplete. By allowing 3D imaging, the user can have a global understanding on cell behavior and interactions of cells with the scaffolds. The incorporation of confocal microscopy for imaging can be crucial and beneficial for fields such as tissue engineering when compared to alternative imaging techniques like SEM, which have no coloring options during observation, are not suitable for live imaging, and provide no information on the cell interior on molecular level.

Even though the SBB treatment reduced autofluorescence dramatically, is still noticeable. We believe this is due to the scaffold attachment to the substrate; the interface between the glass substrate and the scaffold is not reachable for SBB treatment thus allowing some fluorescence to be detected.

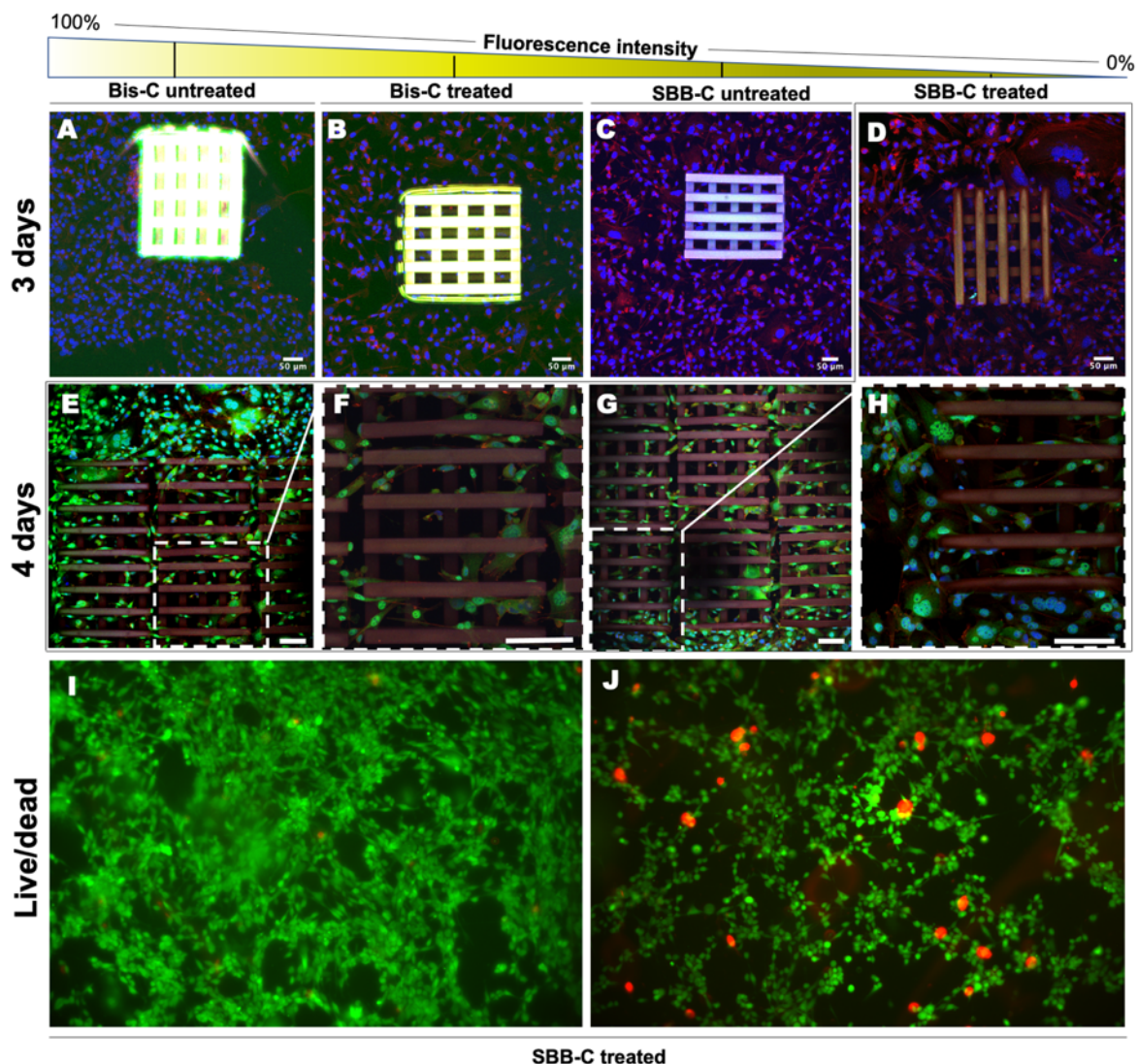


Figure 31. Confocal Microscopy images of the woodpile scaffolds seeded with MSCs (A- H). Each image is a composite of all z-stacks and merged channels. Images of live/dead experiment of MSCs on thin SBB-C films in 48h time point (I, J). **A)** BIS-C, untreated; highest fluorescence. Evaluation of the cell population inside was impossible. **B)** BIS-S, treated; significantly lower fluorescence resulting in some cells to be visible. **C)** SBB-C, untreated; low fluorescence as many cells are clearly visible inside the woodpile. **D)** SBB-C, treated; lowest fluorescence. The nuclei and the actin of the cells inside the scaffold are clearly visible. Cells that adhere on the top of the scaffold are distinguishable from those inside and under it. **E)** Image of 9 woodpiles with MSCs with the respective **F)** zoomed image of the middle scaffold. **G)** Upper end of the same 9 woodpile scaffolds with **H)** zoomed image of the left-end woodpile. **I, J)** 48h of MSCs culture on SBB-C film. Green represents live cells and red the dead ones.

4.8 SBB variant in mechanical metamaterials

To investigate the suitability of SBB-C for the fabrication of high resolution, complex geometries, we employed two very demanding metamaterial designs found in literatures: the

negative Poisson's ratio auxetic scaffold honeycomb reentrant (or bowtie scaffold) [7] and the positive Poisson's ratio ultra- stiff, ultra- light structure tetrakaidecahedron (often refer as Kelvin foam) [8]. Those geometries were fabricated using the 'Nanocube' setup in a unit-cell to unit-cell manner avoiding slicing and ensuring their best mechanical stability and resolution. The auxetic unit cell pore size was 50 μ m while the Kelvin cell pore size was 95 μ m, allowing us to create two different conditions for the cell culture, one 2.5D auxetic scaffold (total dimensions of 2mm x 2mm x 100 μ m) and a 3D Kelvin foam where the cells could penetrate the unit cells (total dimensions of 4mm x 4mm x 95 μ m). The large dimensions of both scaffolds ensured that a good number of cells would be seeded on them creating the perfect mechanical micro-environment for our culture. After 3 days of culture, both samples were stained and prepared for confocal observation as before. This time the observation was conducted from top to bottom in order to avoid the untreated interface regions of the scaffolds.

For the first time it was possible to observe stained MSCs inside such complicated architectures and quantify their interactions with the scaffolds at molecular level by visualizing the levels of YAP protein in the green channel (**Figure 32**). The whole 2mm x 2mm x 100 μ m scaffold was mapped but only a portion of it is shown for convenience. MSCs can be spotted all around both scaffolds and by using higher magnification, it is clear that cells bend and reform the auxetic scaffold in agreement with results acquired in previous work [9], indicating similar mechanical response to those of BIS-C. The Kelvin foam scaffold is a very stiff geometry [10]; thus, no deformations were observed. It is remarkable how further magnification using a 63x lens can make the scaffold barely visible, making it possible to focus the observation solely on the cells' responses to it without the limitations of background fluorescence in all 3 different colors. The unit cell is large enough for many cells to enter as it can be seen in the zoomed unit cell. Furthermore, multiple phenotypes of MSCs are distinguishable on the same scaffold where YAP protein is located mostly in the nucleus (hinting that the extracellular mechanical signal was transferred to the nucleus, inducing gene transcription) or in the cytoplasm with incomparable detail [11]. Alongside with the treated meta- material scaffolds, untreated ones were fabricated and prepared for SEM observation with exactly the same culture conditions as the confocal ones. Those images acquired from SEM were used as reference.

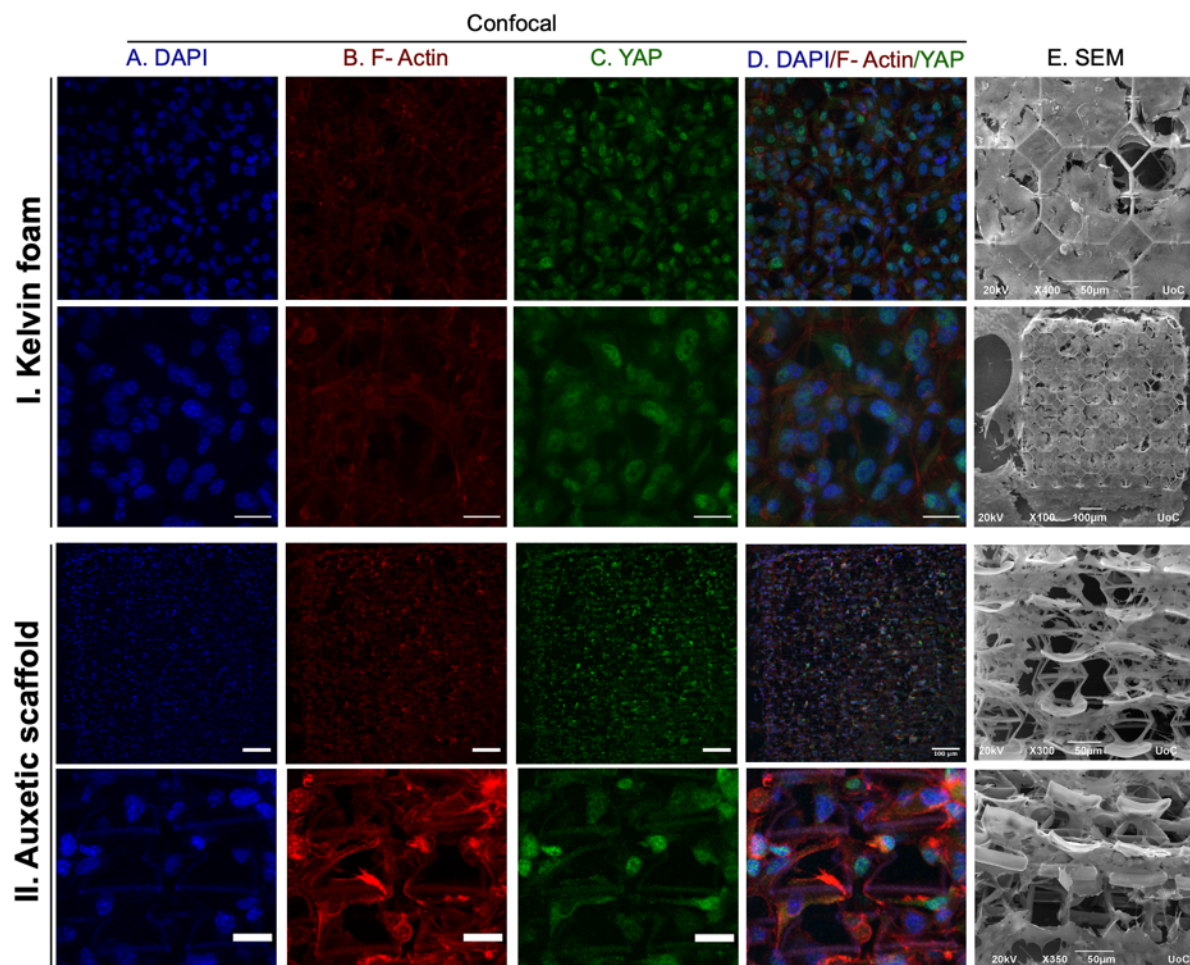


Figure 32. MSCs culture in auxetic scaffold and Kelvin foam made with SBB-C treated material under confocal microscopy and SEM. The first row shows a general view of the kelvin foam with scale bar corresponding to 50µm. The second row shows a zoomed area of a single unit cell with several cells inside (scale bar 20µm). The third row shows a general view of the Auxetic scaffold (scale bar 100µm), and the fourth row a zoomed picture of individual unit cells (scale bar 20µm). **(A) Blue channel:** nuclei, DAPI. **(B) Red channel:** F-actin, phalloidin 568. **(C) Green channel:** YAP protein, FC488. **(D)** All three channels merged together. All images have z- projected all the stacks. **(E)** SEM images.

4.9 Cell Morphology of MSCs with mechanical Metamaterials

MSCs have the ability to differentiate into almost any tissue of the human body under the right condition. There has been a great effort by numerous studies to fabricate scaffolds that can support the differentiated tissue *in vitro*. In our approach, we used a redesigned variant of the Auxetic bowtie scaffold, which now features a star-shaped unit cell, and the Kelvin foam that was previously fabricated [12]. The new design of the Auxetic scaffold (referred to as Auxetic v.2),

In order to rapidly fabricate scaffolds for the cell studies, the GALVO v. two setups was used. The STL file loaded was comprised of a scaffold with 6X6 unit cells of 100 μ m each, reaching a size of 600x600 μ m. Because this size is relatively large, we used a 20X objective lens with an XY field of view reaching 1mm. Then, by simply moving the XY stages of the setup the appropriate distances, we stitched those smaller scaffolds and created the full-size scaffold that could reach up to 1x1cm (**figure 11**). By taking advantage the large scanning area of the 20X objective, and the high speed the galvanometric mirrors can move, the total fabrication time of a 2x2mm scaffold was only 40min, meaning that more of those could be fabricated in a shorter period of time.

4.10 Cell Penetration and directionality studies

In order to investigate the penetration level of the MSCs into the scaffolds, we took advantage of the different z-stacks from the confocal microscope. The height the cells are living on the scaffold is very important piece of information as it reflects the way that this particular cell line would behave in case of a transplant. Another important aspect is that each scaffold has different mechanical environments parts, so this is a key information about the preferred environment. The histograms of the cell depth from the top of the scaffolds are shown in **Figure 33**, 3 different timepoints were chosen for this study, 3, 7 and 14 days of culture in osteogenic differentiation medium. The initial 3 days were important for the cells to successfully proliferate and reach almost 90% confluence. To investigate the point that cells are most found in the scaffold, confocal images were acquired for all the scaffolds in the mention timepoints and the ImageJ software was used to 3D count the blue channels representing the nuclei of the cells. As this was a 3D counting, we were sure about the height the cells were into. Afterwards, the histogram of cells was created by plotting the distance from the top of the scaffold on x-axis and the count of the cells on the y-axis. Interestingly, most of the cells are within the first 20 μ m from the top of the Auxetic scaffold while on Kelvin foam within 20 to 30 μ m, with more of them populating lower parts of the scaffold. Cells do not prefer to go to the highest point of the Kelvin foam, and maybe that's because of the geometry as that scaffold creates some kind of pocket, and the cells prefer to populate those instead of the very top. However, during seeding, the spherical MSC has a diameter of 50 μ m, which is way smaller than the unit cell. Consequently, the cells are migrating from the bottom of the scaffolds to the top, maybe because the top part is more exposed to the nutrients from the medium and also because they can easier create a monolayer which those cells are well known to create.

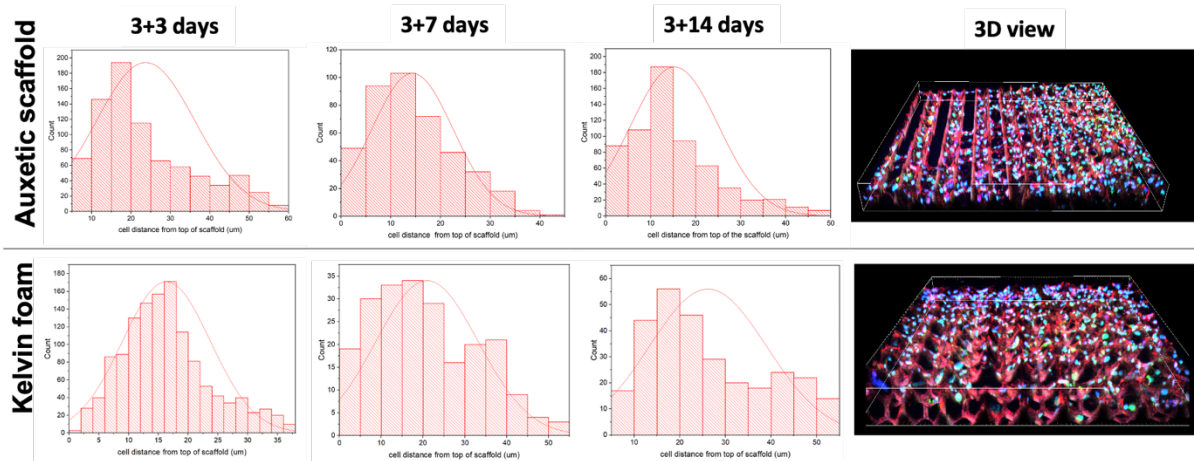


Figure 33. Analysis of the penetration depth of MSC in Auxetic scaffolds and Kelvin foam. Both scaffolds were analyzed in osteogenic differentiation for 3, 7, and 14 days after the initial three days of initial proliferation. The histograms of the different days reveal that cells prefer to proliferate in the first 20-30 μm of the top of the scaffold despite the fact that during initial seeding are able to penetrate the pores and fall to the substrate. The last column shows a 3D representation of the scaffolds after 7 days of culture with Imaris software. **Blue channel:** nuclei, DAPI. **Red channel:** F-actin, phalloidin 568. **Green channel:** Runx2 protein, FC488

Directional cell migration usually relies on a variety of external indications, such as electrical, mechanical, or chemical, which instruct cells in which direction to move [13]. In the case of the metamaterials the mechanical environment is the one that provides with this cue alongside with the architecture of the unit cell. As previously stated, the auxetic scaffold is an anisotropic structure whereas Kelvin foam is an isotropic and that fact by itself may led to a preferential cell directionality. To test this hypothesis, Confocal images were acquired from undifferentiated MSCs cultured on these scaffolds for 3 and 7 days. Then the images were inserted into ImageJ software and the directionality option was selected. The generated histogram shows the directionality of the cytoskeleton of the cells. In the Kelvin foam we see that the cells have no preferred directionality as the histogram shows random orientation in both 3 and 7 days. This is also confirmed by the confocal images where the cell body remains spread with no elongation. On other hand, histogram analysis of the Auxetic scaffold shows that the cells are guided from the scaffold to have the directionality of the unit cell which is $+90^\circ$, and -90° . This effect is observed as early as the 3-day timepoint and is maintained in the 7 days timepoint where cells have proliferated and reach almost 100% confluence on the scaffold. As a results, Auxetic scaffold can guide the cells into a favorable direction aspect really important in tissue engineering [14].

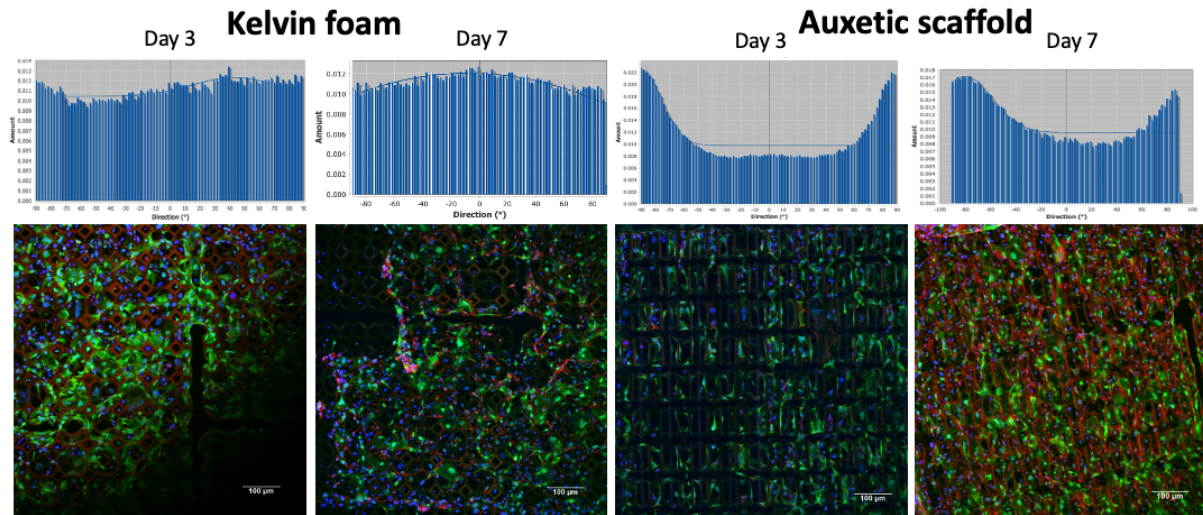


Figure 34. Cell directionality results. Confocal images were used to calculate the degrees of directionality on the scaffolds on days 3 and 7. Cells on kelvin foam show no preferred directionality, while cells on Auxetic are guided from the unit cell to have a directionality of 90°. **Blue channel:** nuclei, DAPI. **Red channel:** F-actin, phalloidin 568. **Green channel:** YAP protein, FC488. All channels are merged together.

4.11 Cell Morphology in differentiation conditions

Other than the depth that cells can reach into the scaffold, it is very important to have a complete knowledge of their morphology as in many cases it may affect their functionality. The best tool for this study is scanning electron microscopy (SEM) which can have up to several nanometers of resolution. Firstly, MSCs were culture on the two different scaffolds, the Auxetic and the Kelvin foam for 5 days until all the scaffold was covered, and then the medium was changed to osteogenic for a total period of 21 days. Then, at each timepoint of 3, 7, 14 and 21 days, those samples were fixed and observed in SEM (**Figure 35**). Scaffolds were fabricated with the Nano setup of the laser in a unit cell by unit cell manner and had size of 4x4mm while the pore size was 100μm. Moreover, all scaffolds were let in culture media for 7 days prior to seeding (timepoint -7). Lastly, the cell morphology on the scaffolds was compared with each other and with the glass substrate control.

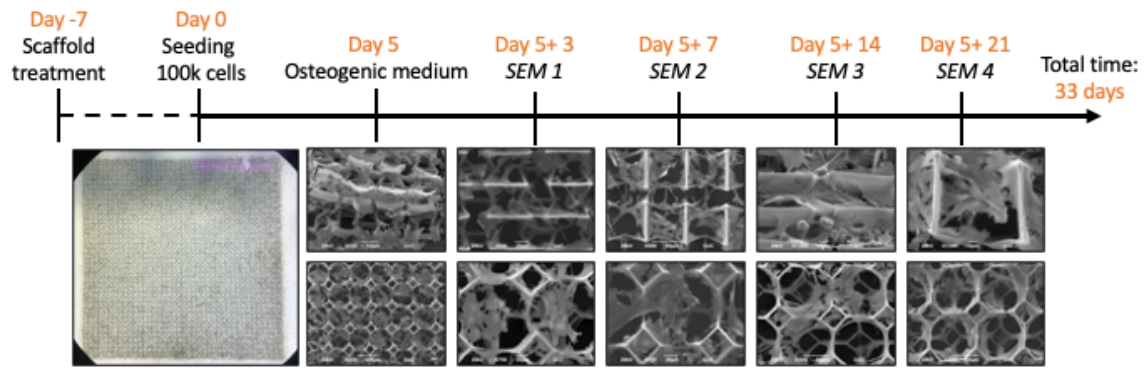


Figure 35. Experimental timeline of the SEM morphology experiment. The fabricated scaffolds were first let in culture medium for 7 days to become more friendly for the cells, and seeding took place at day 0. After 5 days, the confluence had reached almost 90%, and the medium was changed into osteogenic. At the 4 different timepoints, the samples were fixed and observed in SEM. The total experimental procedure lasted for 33 days.

Day 3 timepoint is shown in **Figure 36**. General view of the scaffolds reveal that the confluence of the cells is almost 90%, which means that cells proliferate and migrate towards the surface of the scaffolds successfully (detailed results in *4.10 Cell Penetration and directionality studies*) and in case of the Kelvin foam, the monolayer from the glass has climbed up the scaffold. The zoomed pictures on the unit cells reveal the morphology of the MSCs. As we can see, the cells on kelvin foam show to spread out whereas on the Auxetic scaffold they look elongated with more lamipodia. This differences in the phenotypes are mainly because of the different geometries that the unit cells have. The kelvin foam is an isotropic architecture, which doesn't provide with much directionality as the contact points of the unit cells to a cell are evenly distributed around it. The Auxetic scaffold, on the contrary, is an anisotropic architecture, giving a directionality along the Y-axis. Moreover, its elasticity may play an important role in that phenotype, as the force applied by the cells deform the unit cell, and consequently applies an equal force with the opposite vector to the cells, creating a large number of protrusions.

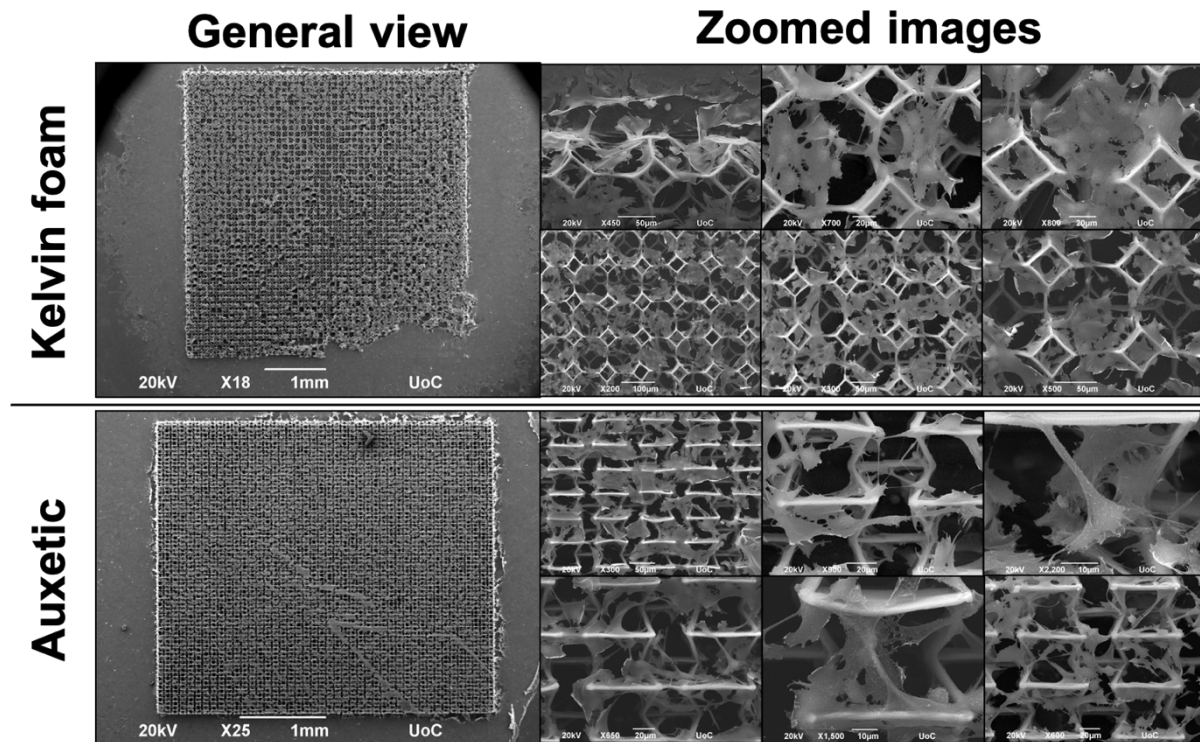


Figure 36. SEM images of MSCs differentiated for 3 days in Kelvin foam and Auxetic scaffold. First row shows the whole scaffolds. The other pictures concern individual unit cells of interest.

Day 7 show no major differences from day 3, cells no longer proliferate but continue to apply forces to the scaffold. Interestingly the image changes when day 14 of differentiation is reached (**Figure 37**). Even if cells stop the proliferation after receiving the signal from the osteogenic medium, the force continue to be applied to the scaffold and the overall deformation of the auxetic scaffold is even more obvious than day 3. Zoomed images also reveal that MSCs become elongated and by further magnification, we observed the formation of calcium depositions (shown with arrows) which seem to be more frequent than the cells in Kelvin foam.

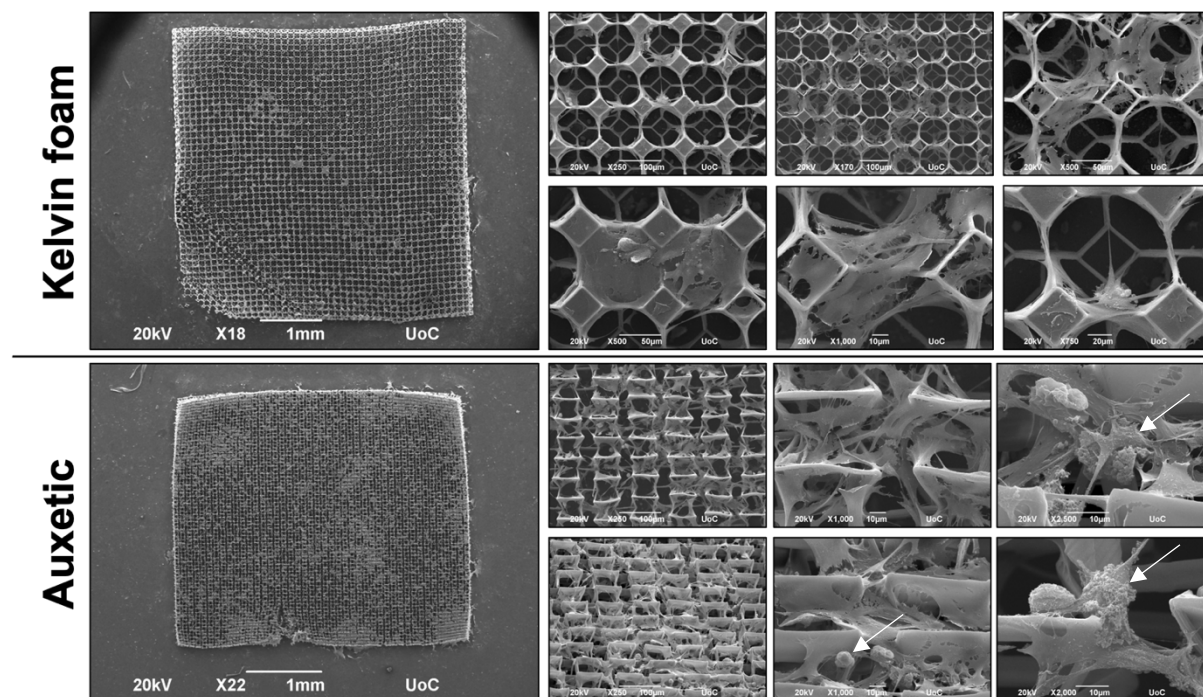


Figure 37. SEM images of MSCs on scaffolds after 14 days in differentiation medium. White arrows show the calcium depositions.

By further alizarin staining we were able to confirm that the accumulations we observed in SEM were actually calcium depositions. The challenging part was that this dye stained the polymeric structures too and not only the depositions, making it harder to distinguish and quantify the absolute values. However, it is obvious that the auxetic scaffold displays a large amount of stained red depositions especially in one of its corners where the cells from the glass substrate are migrating towards the scaffold. It should be noted that those results were obtained from just 14 days in osteogenic differentiation. A possible explanation for this result is that due to cells by applying forces and deform the unit cells, the scaffold is trying to go back into its original state, therefore applying the same force back, which leads to activation of various factors like mechanotransduction genes and proteins.

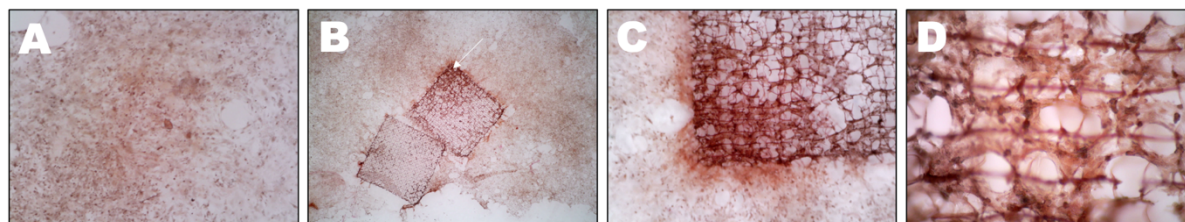


Figure 38. Alizarin red staining after 14 days in osteogenic differentiation A) control on glass coverslip, B) auxetic scaffold and Kelvin foam, C) zoomed corner image from the Auxetic scaffold, D) Further magnification

4.12 Runx2

Runx2 protein is one of the first proteins that gets expressed when MSCs start to differentiate into osteoblasts. In order to measure the levels of this protein in the cells under different scaffolds, 10^5 cells were seeded onto the scaffold and were observed via confocal microscopy in days 3 and 14 after an initial 3 days of proliferation with and without osteogenic differentiation medium. As a control, the glass substrate from the culture was used. It should be noted that for each timepoint, both scaffolds were fabricated via 2PP on the same glass cover slip. For the quantification of Runx2, an innovative pipeline in ImageJ was used, where each z-stack was thresholded individually for the green channel and then through the 3D counter command all the cells were individually counted in 3 dimensions, as well as their intensities. As the protein is located only in the nucleus, there was no need to calculate any cytoplasmic Runx2 which made the analysis more robust, accurate and fast. In this way the human error is eliminated as no hand-counting took place. Afterwards, the intensities from each sample were averaged and plotted. **Figure 39** shows the images from the confocal microscope after 3+3 days of cell culture. Cells on the glass substrate show very low Runx2 intensities while both scaffolds show a strong green color in both differentiation and non-differentiation conditions. By further analysis, Runx2 shows an increase in nucleus 72% in Auxetic scaffolds and 51% in Kelvin foam in comparison with the flat glass substrate (control) and in the osteogenic medium Auxetic scaffolds increased Runx2 by 132% and Kelvin foam 77% in comparison with the glass substrate (differentiation medium). Also, Auxetic scaffold have 12% more Runx2 than Kelvin foam in non differentiation medium and 24% more in differentiation medium.

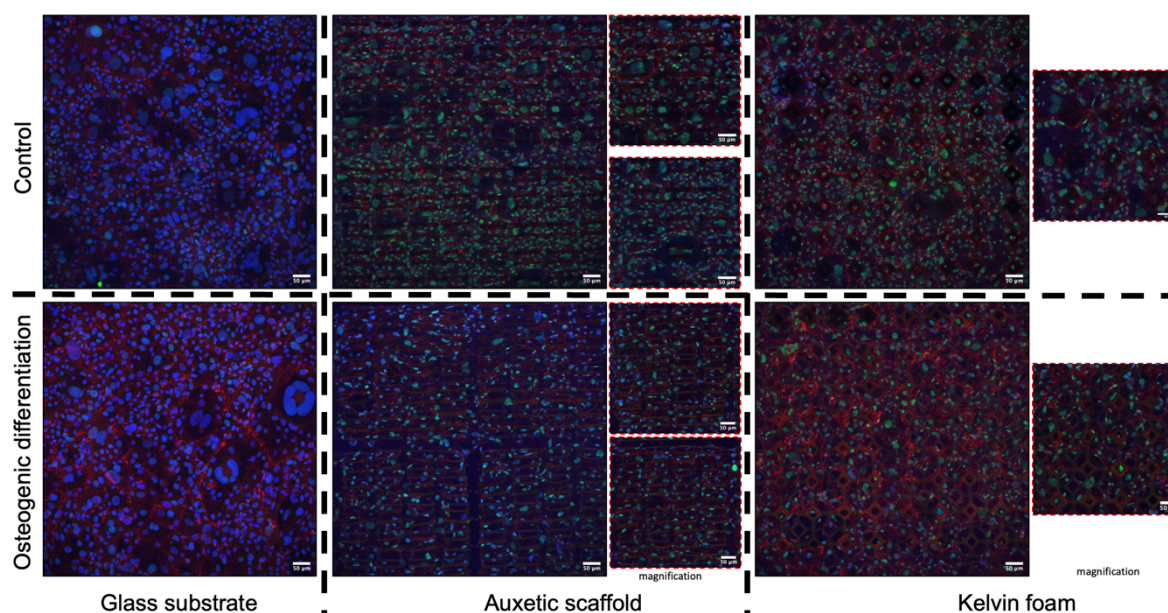
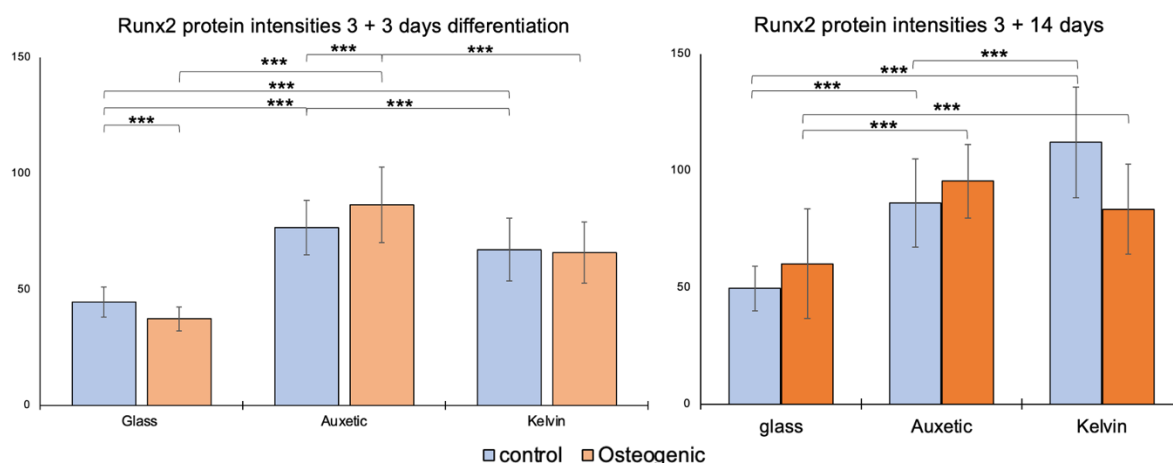


Figure 39. Confocal images of MSCs cultures on the different scaffolds stained for Runx2 protein after 3+3 days. Top row is the control where normal medium was used. Bottom row is the osteogenic differentiation medium. **Blue channel:** nuclei, DAPI. **Red channel:** F-actin, phalloidin 568. **Green channel:** Runx2 protein, FC488.

After 14 days, we observed that the glass and the auxetic scaffold signal stayed at about the same levels, whereas the Kelvin foam increased even higher than the Auxetic scaffold (**Figure 40**). Maybe that's because Runx2 is a very early marker, and the Auxetic scaffold showed the highest value early in osteogenic differentiation. The cell number in the osteogenic differentiation samples are much lower than those of the control as the cells stop proliferating while undergoing differentiation, while the cells in the control continue to proliferate as long as they have free space and enough nutrients.



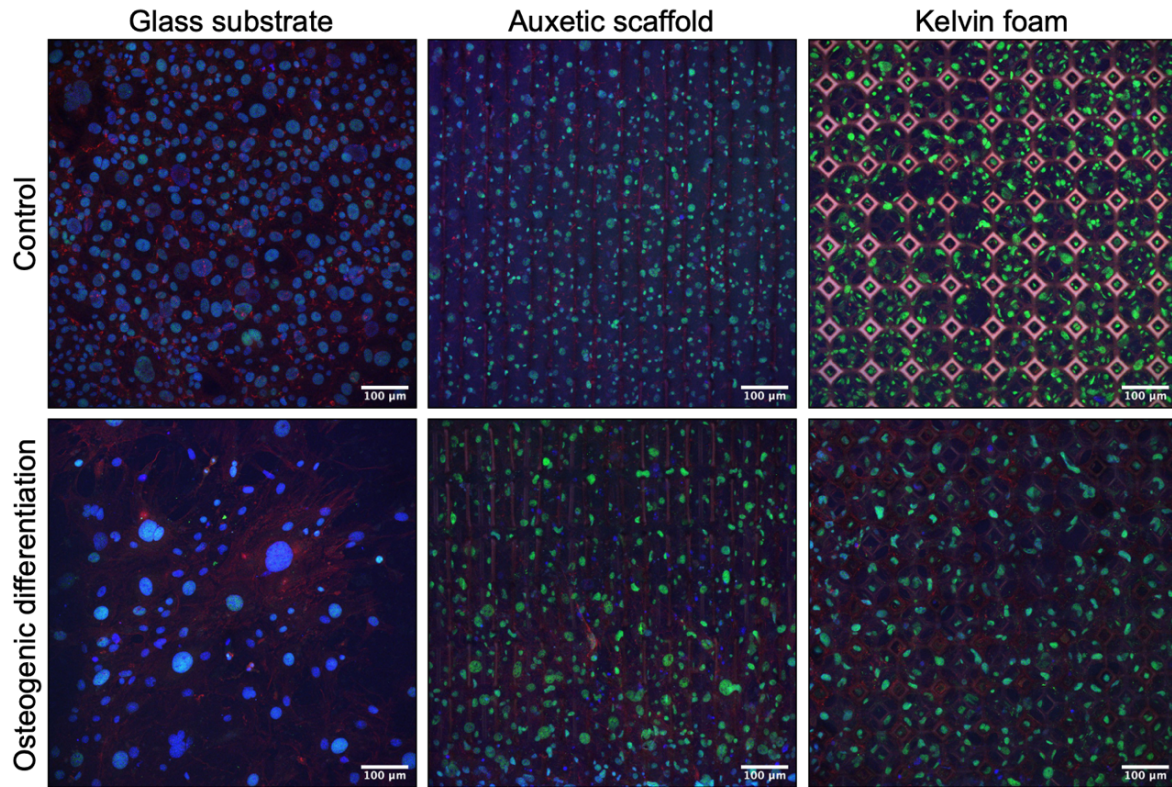


Figure 40. Diagram of the intensities of Runx2. Confocal images of MSC on different scaffolds after 3+14 days in culture in osteogenic differentiation medium and normal medium (control). **Blue channel:** nuclei, DAPI. **Red channel:** F-actin, phalloidin 568. **Green channel:** Runx2 protein, FC488. *** $p < 0.005$

4.13 Runx2 gene expression

Runx2 protein seemed to be elevated in Auxetic scaffolds in 3 days of differentiation. However, the gene expression needed to be also evaluated. For that purpose, special large scaffolds were fabricated. More precisely, both scaffolds for PCR were $4 \times 4 \times 0.1 \text{ mm}$, for a total of $1.6 \cdot 10^9 \mu\text{m}^3$. That means both scaffolds had more than 2,500 unit cells. An MSC cell may be from $1767 - 14138 \mu\text{m}^3$ [15] so, in total, more than 113,000 cells could fit in the overall volume of the scaffolds. This fact was crucial as large number of seeded cells means more quantity of mRNA harvested.

Firstly, the right house-keeping gene needed to be identified. For quantitative reverse transcription-PCR (RT-qPCR) study, normalization to a reference gene is the preferred approach. The stability of reference genes is essential for obtaining precise experimental findings and conclusion. In a study by Li *et al.*, the stability of expression of eight frequently used reference genes discovered in four distinct human mesenchymal stem cells (MSC) was evaluated [16]. The outcome of this study was that GAPDH gene could not be used as its

expression is different between the samples. In our approach, 3 different genes were used: GAPDH (Glyceraldehyde 3- phosphate dehydrogenase), RPL13A (ribosomal protein L13a) and B2m (Beta-2 microglobulin). The expression of those genes was tested in 4 different samples: cells seeded on cover slips with and without osteogenic differentiation for 3 days and on Auxetic scaffolds with the same conditions. After the 3 days culture, the samples were lysed with trizol and total mRNA was harvested. The measurement with nanodrop of the samples showed that more than 1000 ng/ μ l of mRNA was isolated from control sample without osteogenic differentiation medium, and about half of it with the osteogenic differentiation. This result is expected as the proliferation is arrested in cells undergoing differentiation. On the other hand, we were able to isolate 600 ng/ μ l from the Auxetic scaffold sample without differentiation and 450 ng/ μ l from the sample under differentiation conditions. Those results were very promising as there was more than enough mRNA template for the reverse transcription process and consequently for the RT-qPCR.

The mRNA was then reverse transcribed to cDNA, and the resulting DNAs run in agarose gel. By comparing the band's intensities, we concluded that GAPDH cannot be used as a house keeping gene as it is not equally expressed in all of the samples. Interestingly, alongside with RPL13a, their expression is downregulated in osteogenic differentiation samples and seems to follow the mRNA quantity trend. On the other hand, we acquired bright bands in the case of B2M, which are equal in all of the samples (**Figure 41**). Consequently, this gene was the perfect candidate for the qPCR experiments.

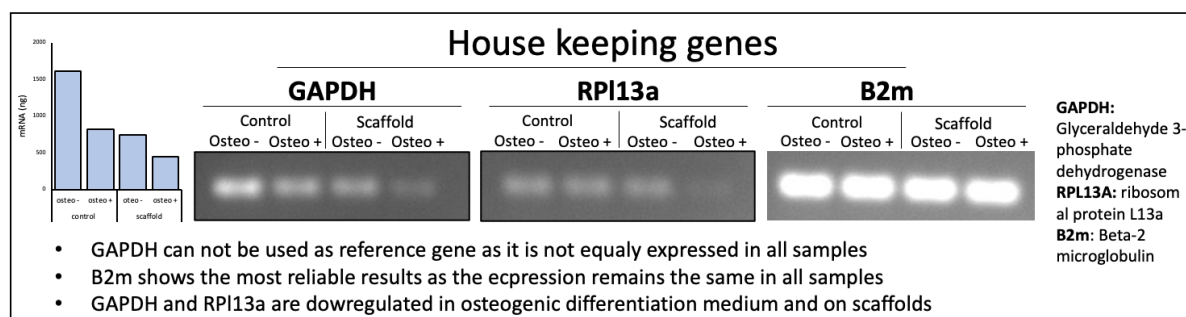


Figure 41. House -keeping gene test. On the left, the isolated mRNA quantities are graphed in all four samples (ng/ μ l). Centre: Bands on the agarose gel of the samples. GAPDH and Rpl13a show great inconsistency in their expression through the samples, whereas B2m show a constant expression making it the ideal housekeeping gene.

For the RT-qPCR, large area scaffolds were fabricated and seeded with 10^5 cells. After a period of 3 + 3 days, RNA was isolated, reverse transcribed into cDNA and primers for B2m and Runx2 were used to identify the expression of Runx2. Using the Δ CCt method, we

identified that both Auxetic and Kelvin foam have 15- and 21-fold Runx2 expression in comparison with the flat surface glass in undifferentiated medium, and, remarkable, Auxetic had 21- fold expression in the differentiation medium samples letting Kelvin foam in 2 -fold (**Figure 42**). The gene expression results are in agreement with the immunofluorescence results where both scaffolds had an increase in Runx2 protein intensities than the glass, meaning that upregulation of osteogenesis is succeeded more efficiently in Auxetic environments.

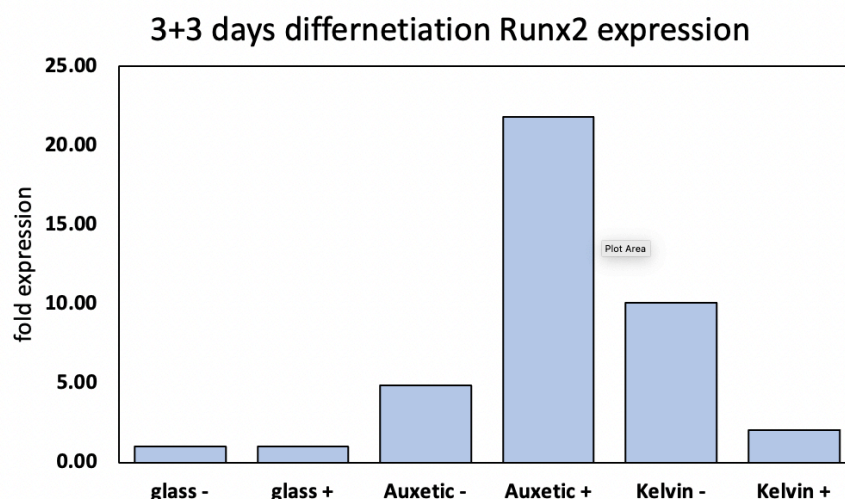


Figure 42. Relative expression of Runx2 gene after 3 + 3 days in both scaffolds and control glass substrate.

4.14 Yap protein

As stated before, YAP is controlled by mechanical cues such as different mechanical properties of the extracellular matrix rigidity, strain, shear stress, or adhesive area, processes that are dependent on cytoskeletal integrity [17]. In our case, the extracellular environment that cells could sense were the Auxetic scaffold and the stiff Kelvin foam. In order to test how YAP protein behaves under those different mechanical environments, MSCs were cultured on the scaffold for 3, 7 and 17 days without differentiation medium. Then on each timepoint samples were fixed and stained with specific antibodies for YAP protein and observed in confocal microscope where several z-stacks of the scaffolds were acquired. Afterwards, the images were inserted into ImageJ software and YAP intensities were analyzed through a novel pipeline. The most important aspect of this protein was to distinguish the signal that derives from the nucleus from the cytoplasmic signal. This distinction is much harder in case of a 3D culture. Furthermore, it is impossible to count those intensities by hand, so we had to develop a new pipeline in the software to be able to distinguish those two signals. This pipeline includes co-localizing the blue channel which corresponds to the nucleus with the green channel through the AND command. In that way, the new image only includes the intensity of YAP protein

inside the nucleus. By applying certain thresholds in each different stack, it was possible to 3D count the signal only from the nucleus and exclude the one from the cytoplasm. Then, by a simple subtraction of the nuclear signal to the overall green channel we were able to calculate the cytoplasmic signal of YAP protein and eventually calculate the ratios of nucleic/cytoplasmic protein.

Results from these experiments summarized in **Figure 43**. On 3rd day of the culture, the control which is the glass substrate shows a ratio of around one between the cytoplasmic in the nuclear protein. Also, the intensity of the control is much lower the intensity in the two scaffolds. The Auxetic scaffold shows a higher concentration of cytoplasmic yap protein as well as the Kelvin foam which means that the mechanical cues from the extracellular matrix have not yet pass to the nucleus.

The picture completely changes on the 7th day of culture, where control's nuclear YAP protein is much higher than the cytoplasmic. On the other hand, because of the fact that Auxetic scaffold is elastic, the Yap protein does not translocate to the nucleus, since higher cytoplasmic signal was observed. Kelvin foam displays a higher nuclear signal than the cytoplasmic one, a fact that is expected due to the high stiffness of this architecture.

After 17 days of culturing, we see that there are no major differences from the 7th day. The nuclear YAP protein of the control remains higher from the cytoplasmic, as well as the Kelvin foam. However, the intensity of the protein in the Kelvin foam shows an increase which means that more YAP protein is produced by the cell. The cytoplasmic protein on the Auxetic scaffold remained higher than the nuclear, as expected.

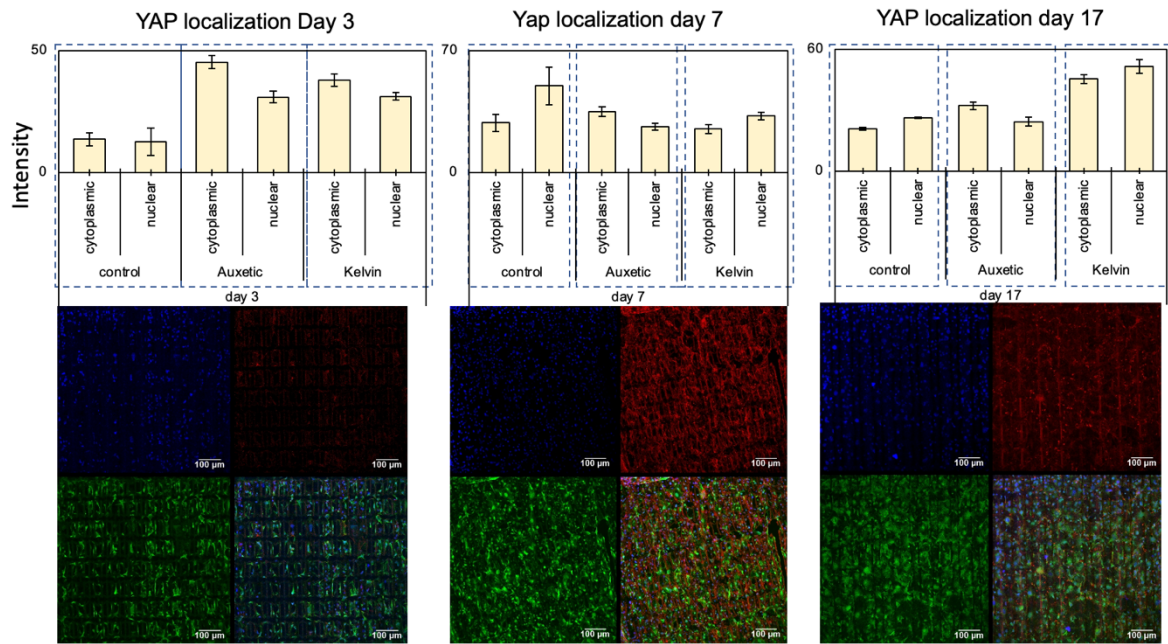


Figure 43. Confocal images of MSCs culture on the Auxetic scaffold alongside with their YAP localization diagrams. $P < 0.005$ for all the samples.

4.15 Summary

Two different mechanical metamaterials were fabricated through MPL, one auxetic and one ultra-stiff. Those two opposite mechanical environments were used to study the differentiation potential into bone of MSCs. Initially, Alizarin red staining revealed that Auxetic environment induce the formation of calcium depositions in a higher rate than the control and Kelvin foam in a 14 days culture with differentiation medium. This result hinted that auxetic environment may have a positive effect on bone formation. For that reason, SEM images were acquired on different timepoints and the morphology of cells was revealed. More precisely, Auxetic scaffolds encouraged cells to be more elongated, whereas Kelvin foam induced a flatter phenotype. Also, some calcium depositions were observed. Furthermore, confocal microscopy revealed that cells preferred to populate the top of the scaffolds, rather than the whole volume of it, and also that Auxetic could provide with nice directionality of cell bodies. Consequently, it was proven that those two environments could indeed differentiate the morphology of cells. The next step was to evaluate the main mechanotransduction sensing element of the cells, YAP protein. In that case, we showed that YAP translocated into the nucleus in case of the stiff Kelvin foam, but mainly remained in the cytoplasm in case of Auxetic scaffolds. These results agreed with the bibliography, where stiffer substrates induce the nuclear translocation of YAP while softer ones didn't. Moreover, Runx2 protein

measurement showed a higher expression in Auxetic environment even without differentiation medium, a fact that proves the mechanical environment by itself can induce osteogenic differentiation in early stages. Remarkably, both environments showed higher expression than the flat glass substrate, showing the necessity of 3D environments when it comes to researching cell responses. The explanation behind those results is that by sensing soft and elastic mechanical environments, MSCs lead YAP protein into proteasomes in the cytoplasm for degradation, allowing Runx2 to be expressed and translocated into the nucleus where it can induce early stages of osteogenesis. On the other hand, When YAP isn't degraded, it can create a complex with Runx2, thus not allowing it to induce early stages of osteogenesis by inhibiting its transcriptional activity [18]. Therefore, we propose that auxetic environment is able to induce early stages of osteogenesis and differentiation better than 2D glass substrate and stiff environments such as Kelvin foam (**Figure 44**).

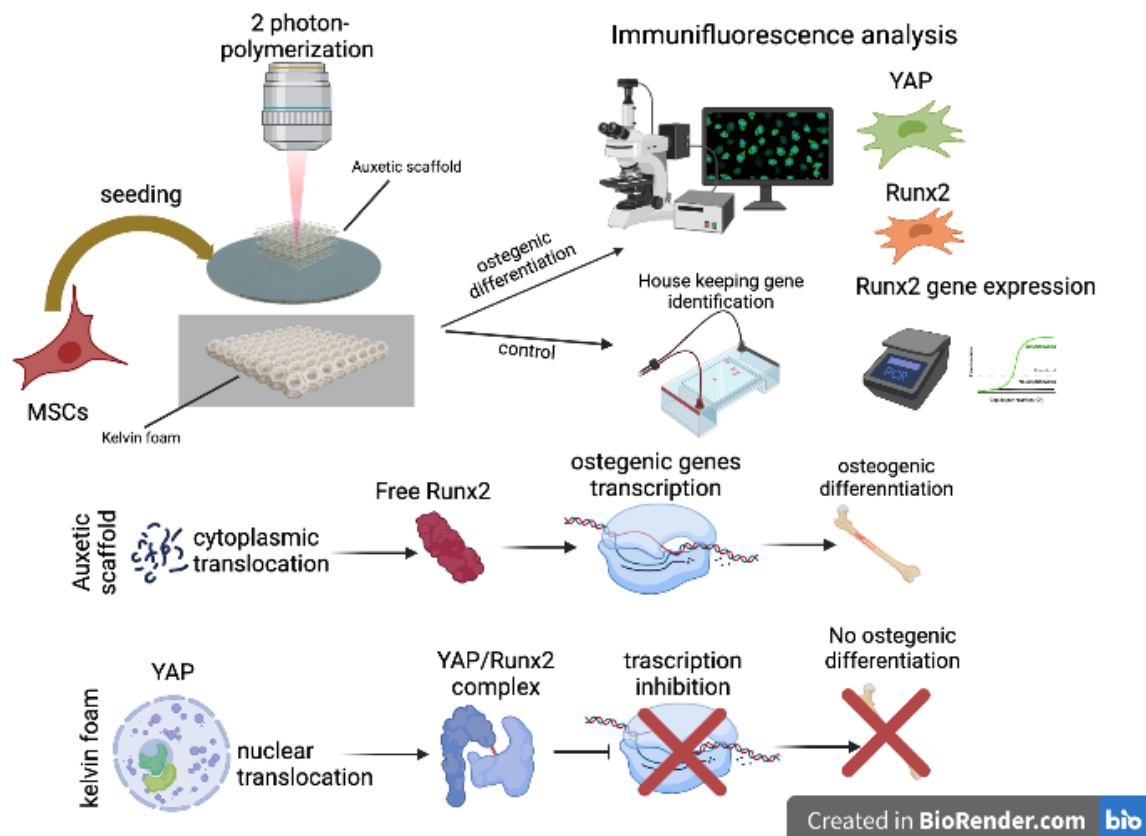


Figure 44. Graphical abstract of the experimental procedure and proposed model of auxetic environment bone differentiation induction.

4.16 Breaking the size barrier: SLA method

Even though MPL is very powerful technique with great resolution, it lacks the ability to use it for the fabrication of large-scale scaffolds comparable to an organism. However, the excising light additive manufacturing techniques can provide with such structures. For example, the SLA based 3D printer 4k MONO from Anycubic, promises great pixel resolution up to 35 μm . By taking advantage of that small pixel size, we tried to create high-resolution scaffolds with very small feature. To achieve as high resolution as possible, the exposure time of the UV lamp for each layer needed to be fine-tuned and adjusted. Moreover, an important asset was the slicing distance which refers to the distance that each layer has from the other. We decided to keep the smallest length the machine could provide which was 20 μm . So, by keeping the slicing distance the same and optimizing the exposure time at 1s, we were able to create 3 different structures, each one with unique geometries and properties. Those scaffolds ranged from simple 2.5D groove-like scaffolds to a complicated gyroid scaffolds (**Figure 45**). The STL file for the gyroid scaffold was made using the Hyperganic software which allowed us to create via AI this complicated structure with minimum effort. After fabrication, the scaffold was observed via SEM and the pictures shows a very well-defined structure with each line to be only 50 μm and pores 200 μm . The total size of the scaffold was 14mm which is ideal for the 24 well plate was seeding and culturing of cells takes place.

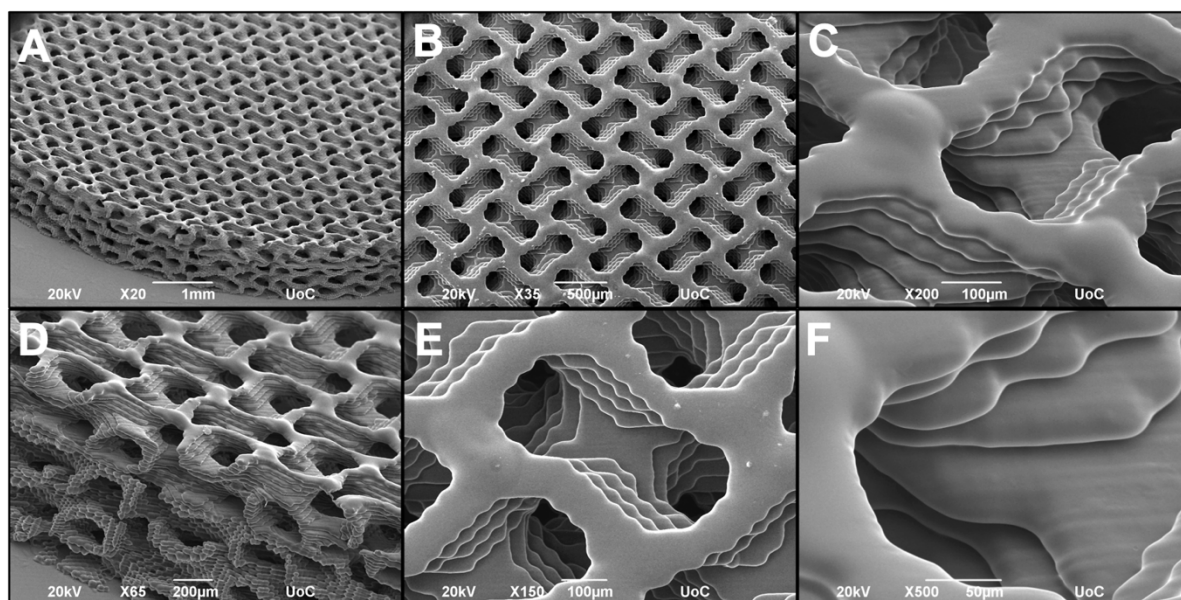


Figure 45. SEM pictures of the TPMS gyroid scaffold fabricated via SLA with a commercially available UV 3D printer. The overall diameter of this scaffold was 14mm and the pore size was 200 μm .

The particular 3D printer and resins used are meant to be used for creating mainly everyday life utilities and decoratives. It was important to assess the cytotoxicity and the compatibility of this method in order to demonstrate its suitability for tissue engineering applications. Consequently, all the above structures were seeded with 2 different cell lines and observed under both an optical microscope and SEM for a total period of 10 days. Furthermore, histochemical staining was conducted on days 3 and 7 and the results are shown in **Figure 46** showing that MSCs appear to have spread to the whole scaffold keeping an elongated morphology and reaching a confluence of 100%. Unexpectedly, due to the large size of the period of the lines, we were unable to obtain favorable cell directionality, a problem that could be solved by reducing the period.

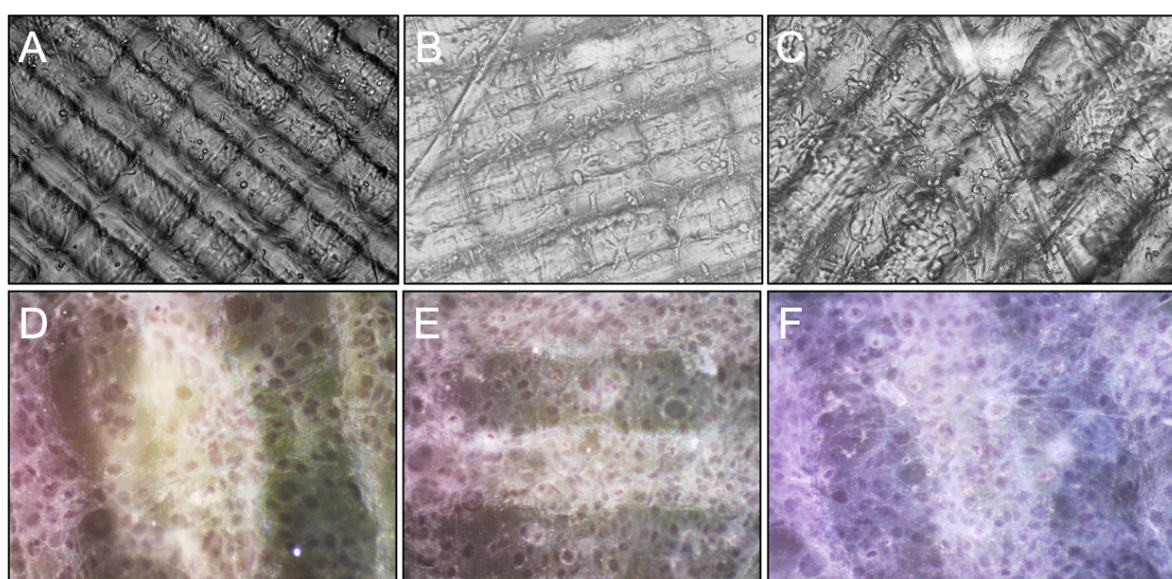


Figure 46. Brightfield microscopy images of the groove scaffold seeded with MSCs. **A)** 1d of culture **B)** 3 days of culture with **C)** 7 days of culture **D)** DAB staining of Hematoxylin (nuclei) on day 1, **E)** day 3 and **F)** day 7

In addition to MSCs, mouse macrophages were cultured on both a simple grid scaffold and on gyroid scaffold. SEM images were acquired after 2, 4 and 6 days in order to evaluate the morphology of the cells in the presence of the scaffold. Cells appear to make aggregates in both scaffolds. Also, they have penetrated all the holes of the gyroid scaffold and after 6 day they appear to have greatly proliferated and also immersed to the surface, where more elongated phenotypes are observed.

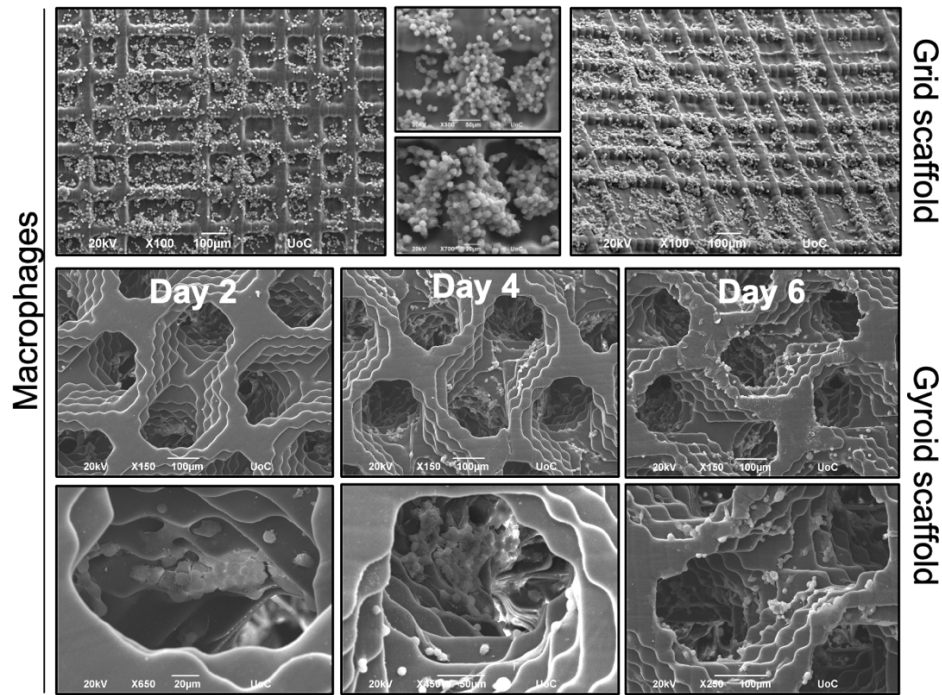


Figure 47. SEM images of grid scaffold and gyroid scaffold seeded with mouse macrophages.

Discussion

The use of metamaterials in tissue engineering applies the principles of interdisciplinarity by combining physical science, computational modeling, and mechanical biology. Mechanical metamaterials have considerable benefits over standard scaffolds on mechanical controls of cells and tissues, including improved cellular geometries and hitherto unseen mechanical characteristics. Poison rationing has been used in biomedical applications both *in vitro* and *in vivo*. Despite the fact that the value of metamaterials in biological investigations has been thoroughly proved, the range of cellular designs employed in cell and tissue engineering is very restricted when compared to the abundance of available geometries. Many other remarkable mechanical features of metamaterials, such as negative compressibility, have yet to be widely exploited in biological disciplines. Extrusion printing was utilized to create dilatational metamaterials with 3D isotropic auxeticity at centimeter sizes, while TPP was used to create a homogeneous tissue construct with multidirectional elasticity at micrometer scales. Because of the limitations of production procedures, simpler microstructured metamaterials were more commonly employed for various applications. More comparisons of metamaterials with

comparable mechanical properties but distinct unit cell microstructures are required. Both re-entrant and rotating rigid structures, for example, can give the auxetic feature, while the former is more commonly used in the production of tissue engineering scaffolds.

Two photon lithography set the basis for the fabrication of very complicated structure in the microscale. By using different photoresists there is the possibility for the creation of structures with various mechanical properties and characteristic ranging from 2D to 3D [19] and even 4D [20] which is a very new field in the field of additive manufacturing technologies first introduced in 2013. 4D printing technologies enable for the fabrication of structures that can be changed in space and time under different stimuli such as temperature [21]–[23], radiation [24]–[26] pH [27], [28] and other. In this work the fabrication of the auxetic scaffold paved the way for a new kind of adaptable scaffolds, that can change their morphology under mechanical stimuli from the cells and are a perfect candidate for tissue engineering applications [29]. Furthermore, it was shown that even though SZ2080TM photoresist is a hard, positive photoresist material, after polymerization, it can display elastic properties by just fine-tuning the architecture of the unit cell and make it display negative Poisson ratio. In addition, we have shown that fibroblast cells can readily penetrate and proliferate in these scaffolds, adapting the scaffold shape to suit their necessities increasing their proliferation and acquiring desirable directionality [29]. Previous studies used auxetic foam for vascular differentiation of pluripotent stem cells [30], simple 2D auxetic sheets to investigate cellular responses [31] and even use of such scaffolds for neural differentiation [32]. So, there is an extent effort of groups around the globe to incorporate negative Poisson ratio scaffolds into tissue engineering applications. This work aimed to move a step further into that effort by not only fabricating auxetic scaffold, but also creating a true 3D auxetic environment, as the difference between 2D and 3D cultures is vast [33]–[35]. Two main cell lines were used to test those environments, NIH-3T3 mouse fibroblasts and MSCs. Furthermore, MSCs were differentiated into osteoblast under auxetic conditions and their ability to form calcium deposition was evaluated with Alizarin red staining, showing that under that environment bone formation was induced in just 15 days. As a control the opposite mechanical environment was used known as kelvin foam, as well as the simple 2D glass substrate.

One of the most basic challenges this work had to overcome was the accurate and robust analysis of the results, as a 3D environment is much more complicated than 2D. For that reason, confocal microscope enables for such analysis because it can penetrate the sample to a specific depth and image the cells through fluorescent molecules. Having acquired all the z- stacks, one

is able to combine them and represent the scaffold in 3D in computer environment. In most cases where cells are grown on a well in a 2D culture the analysis is more straightforward. By developing an innovative pipeline alongside with the autofluorescence free material SBB-C [12] this obstacle was surpassed and the protein levels of YAP and Runx2 were calculated accurately. Interestingly, the nuclear/cytoplasmic ratio of YAP protein remained high in Kelvin foam and the glass control, where in the Auxetic it was <1 even after 17 days in culture. This result was expected as elastic environments doesn't allow YAP to translocate into the nucleus, where stiff ECM allows it to be translocated. This translocation was the main component of the osteogenic homeostasis and differentiation as YAP is able to make a complex with Runx2, thus not allowing it to induce the expression of downstream genes [18].

Naturally, the overall size of scaffold is still a considerable drawback, as 2PP allows for the fabrication of small scaffolds with great resolution. However, with the right optimization of the design and the considerably fast scanning speed of the galvanometric mirrors we were able to fabricate large scaffold that covered an area of 1cm^2 in just 8 hours. Large scaffolds are crucial for molecular biology methods that require large number of cells such as PCR or western blotting. Additionally, in order to overcome this size drawback, a commercial 3D printer (Anycubic) was used to create large- free standing scaffolds with the commercially available resin Clear provided by the same company. The fabricated scaffolds proved to be promising as cells can be seeded on them with little to non cytotoxicity, and the method by itself is really fast, cheap and the setup is a fraction of the total size of a typical 2PP system. Moreover, a great resolution was obtained regardless the large size of the scaffolds of approximately $25\mu\text{m}$. **Figure 48** depicts the size difference of the same scaffold fabricated with the Anycubic printer and 2PP. The one photon 3D printer opens new possibilities for the creation of high-resolution large scaffolds and it requires further investigation to exploit its' full capabilities. All experiments conducted on the 2PP system could be replicated with the scaffolds made with the 3D printer as no cytotoxicity is observed.

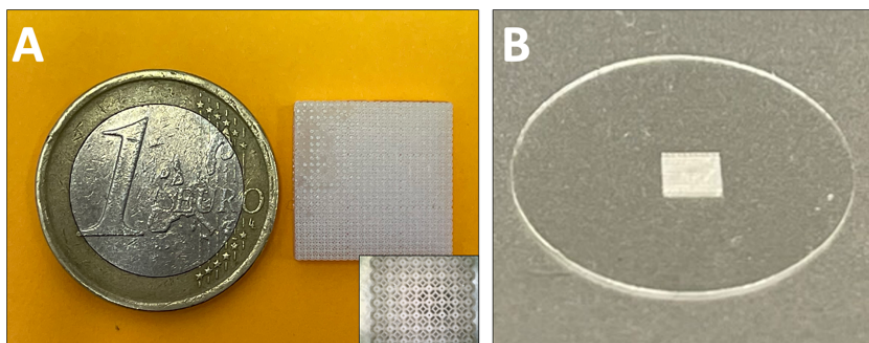


Figure 48. Comparison between 3D printer and 2PP fabricated scaffolds **A)** Kelvin foam made with the Anycubic printer next to a 1-euro coin used as scale **B)** the same scaffold fabricated with 2PP on a 13mm cover glass.

This extended work paved the way for the use of metamaterials in tissue engineering and expanded the conventional scaffolds used until now like woodpiles structures. Nevertheless, future plans involve the measurement of the shear stress applied to the Auxetic scaffold. This measurement can be made by fabricating a thin column of auxetic inside a microfluidic channel and applying microfluidic flow with simultaneous observation under a microscope. This is a very important measurement as the next generation culture for tissue engineering involves the application of flow representing the flow of various fluids such as blood inside the human body [36].

Nanoindentation is ideal for quantifying different mechanical properties of the scaffolds. However, its small size doesn't allow for real life scaffolds seeded with cells which change the mechanical environment as forces are applied. Moreover, the calcium depositions which is a hard material may change the properties of the scaffold in later osteogenic stages. Also, those late stages could be monitored past the confocal microscopy, using Alizarin Red staining, or ALP activity to visualize even better the calcium depositions. One main drawback for this late timepoints is that due to the applied force from cells, scaffolds detach from the glass substrate and the monolayer floats in the medium after 28 days of culture. To overcome this issue, scaffolds could be fabricated over pedestals in order to increase the contact area with the glass substrate and make it harder to detach due to applied forces.

In conclusion, in this extended work we aimed to fabricate and characterize novel auxetic metamaterial scaffolds and used them for different tissue engineering approaches. Auxetics seems to have a promising future regarding osteogenic differentiation potentials, and by further investigation those metamaterials could find their way into clinical trials. This study paved the way for the introduction of such complicated structures into the tissue engineering routine, and hopefully, in the future those results may improve the lives of millions of people.

References

- [1] A. Ovsianikov *et al.*, "Ultra-low shrinkage hybrid photosensitive material for two-photon polymerization microfabrication," *ACS Nano*, vol. 2, no. 11, 2008, doi: 10.1021/nn800451w.

- [2] I. H. Jaafar, C. E. Leblon, M. T. Wei, D. Ou-Yang, J. P. Coulter, and S. S. Jedlicka, “Improving fluorescence imaging of biological cells on biomedical polymers,” *Acta Biomater*, vol. 7, no. 4, pp. 1588–1598, Apr. 2011, doi: 10.1016/j.ACTBIO.2010.12.007.
- [3] K. Yue, G. Trujillo-de Santiago, M. M. Alvarez, A. Tamayol, N. Annabi, and A. Khademhosseini, “Synthesis, properties, and biomedical applications of gelatin methacryloyl (GelMA) hydrogels,” *Biomaterials*, vol. 73, pp. 254–271, 2015, doi: <https://doi.org/10.1016/j.biomaterials.2015.08.045>.
- [4] S. Abdulghani and G. R. Mitchell, “Biomaterials for in situ tissue regeneration: A review,” *Biomolecules*, vol. 9, no. 11, 2019, doi: 10.3390/biom9110750.
- [5] S. Psycharakis, A. Tosca, V. Melissinaki, A. Giakoumaki, and A. Ranella, “Tailor-made three-dimensional hybrid scaffolds for cell cultures,” *Biomedical Materials*, vol. 6, no. 4, p. 045008, Aug. 2011, doi: 10.1088/1748-6041/6/4/045008.
- [6] M. T. Raimondi, S. M. Eaton, M. M. Nava, M. Laganà, G. Cerullo, and R. Osellame, “Two-photon laser polymerization: from fundamentals to biomedical application in tissue engineering and regenerative medicine,” *J Appl Biomater Funct Mater*, vol. 10, no. 1, pp. 56–66, Aug. 2012, doi: 10.5301/JABFM.2012.9278.
- [7] L. Song, M. F. Ahmed, Y. Li, C. Zeng, and Y. Li, “Vascular differentiation from pluripotent stem cells in 3-D auxetic scaffolds,” *J Tissue Eng Regen Med*, vol. 12, no. 7, pp. 1679–1689, 2018, doi: 10.1002/term.2695.
- [8] C. Ge, L. Priyadarshini, D. Cormier, L. Pan, and J. Tuber, “A preliminary study of cushion properties of a 3D printed thermoplastic polyurethane Kelvin foam,” *Packaging Technology and Science*, vol. 31, no. 5, pp. 361–368, 2018, doi: <https://doi.org/10.1002/pts.2330>.
- [9] G. Flamourakis *et al.*, “Laser-made 3D Auxetic Metamaterial Scaffolds for Tissue Engineering Applications,” *Macromol Mater Eng*, p. 10.1002/mame.202000238, 2020.
- [10] X. Zheng *et al.*, “Ultralight, ultrastiff mechanical metamaterials,” *Science (1979)*, vol. 344, no. 6190, pp. 1373–1377, Jun. 2014, doi: 10.1126/SCIENCE.1252291/SUPPL_FILE/ZHENG.SM.PDF.
- [11] A. E. Stanton, X. Tong, S. Lee, and F. Yang, “Biochemical Ligand Density Regulates Yes-Associated Protein Translocation in Stem Cells through Cytoskeletal Tension and Integrins,” *ACS Appl Mater Interfaces*, vol. 11, no. 9, pp. 8849–8857, 2019, doi: 10.1021/acsami.8b21270.
- [12] G. Flamourakis, A. Kordas, G. D. Barmparis, A. Ranella, and M. Farsari, “Low-autofluorescence, transparent composite for multiphoton 3D printing,” *Opt. Mater. Express*, vol. 11, no. 3, pp. 801–813, Mar. 2021, doi: 10.1364/OME.418269.

- [13] A. Shellard and R. Mayor, “All Roads Lead to Directional Cell Migration,” *Trends Cell Biol*, vol. 30, no. 11, pp. 852–868, Nov. 2020, doi: 10.1016/J.TCB.2020.08.002.
- [14] J. Koffler *et al.*, “Biomimetic 3D-printed scaffolds for spinal cord injury repair,” *Nature Medicine* 2019 25:2, vol. 25, no. 2, pp. 263–269, Jan. 2019, doi: 10.1038/s41591-018-0296-z.
- [15] T. E. G. Krueger, D. L. J. Thorek, S. R. Denmeade, J. T. Isaacs, and W. N. Brennen, “Concise Review: Mesenchymal Stem Cell-Based Drug Delivery: The Good, the Bad, the Ugly, and the Promise,” *Stem Cells Transl Med*, vol. 7, no. 9, pp. 651–663, Sep. 2018, doi: 10.1002/SCTM.18-0024.
- [16] X. Li, Q. Yang, J. Bai, Y. Xuan, and Y. Wang, “Identification of appropriate reference genes for human mesenchymal stem cell analysis by quantitative real-time PCR,” *Biotechnol Lett*, vol. 37, no. 1, pp. 67–73, Jan. 2015, doi: 10.1007/S10529-014-1652-9.
- [17] A. Elosegui-Artola *et al.*, “Force Triggers YAP Nuclear Entry by Regulating Transport across Nuclear Pores,” *Cell*, vol. 171, no. 6, pp. 1397–1410.e14, Nov. 2017, doi: 10.1016/j.cell.2017.10.008.
- [18] S. K. Zaidi *et al.*, “Tyrosine phosphorylation controls Runx2-mediated subnuclear targeting of YAP to repress transcription,” *EMBO Journal*, vol. 23, no. 4, pp. 790–799, Feb. 2004, doi: 10.1038/SJ.EMBOJ.7600073.
- [19] A. Sharaf, B. Roos, R. Timmerman, G.-J. Kremers, J. J. Bajramovic, and A. Accardo, “Two-Photon Polymerization of 2.5D and 3D Microstructures Fostering a Ramified Resting Phenotype in Primary Microglia,” *Front Bioeng Biotechnol*, vol. 0, p. 1105, Jul. 2022, doi: 10.3389/FBIOE.2022.926642.
- [20] P. Fu *et al.*, “4D printing of polymers: Techniques, materials, and prospects,” *Prog Polym Sci*, vol. 126, p. 101506, Mar. 2022, doi: 10.1016/J.PROGPOLYMSCI.2022.101506.
- [21] S. Pandini *et al.*, “Shape memory response and hierarchical motion capabilities of 4D printed auxetic structures,” *Mech Res Commun*, vol. 103, Jan. 2020, doi: 10.1016/j.mechrescom.2019.103463.
- [22] S. van Hoa, “Development of composite springs using 4D printing method,” *Compos Struct*, vol. 210, pp. 869–876, Feb. 2019, doi: 10.1016/j.compstruct.2018.12.003.
- [23] M. C. Mulakkal, R. S. Trask, V. P. Ting, and A. M. Seddon, “Responsive cellulose-hydrogel composite ink for 4D printing,” *Mater Des*, vol. 160, pp. 108–118, Dec. 2018, doi: 10.1016/j.matdes.2018.09.009.
- [24] I. Roppolo *et al.*, “3D printable light-responsive polymers,” *Mater Horiz*, vol. 4, no. 3, pp. 396–401, 2017, doi: 10.1039/C7MH00072C.

- [25] B. M. Boyle, T. A. French, R. M. Pearson, B. G. McCarthy, and G. M. Miyake, “Structural Color for Additive Manufacturing: 3D-Printed Photonic Crystals from Block Copolymers,” *ACS Nano*, vol. 11, no. 3, pp. 3052–3058, Mar. 2017, doi: 10.1021/ACSNANO.7B00032.
- [26] E. C. Davidson, A. Kotikian, S. Li, J. Aizenberg, and J. A. Lewis, “3D Printable and Reconfigurable Liquid Crystal Elastomers with Light-Induced Shape Memory via Dynamic Bond Exchange,” *Advanced Materials*, vol. 32, no. 1, Jan. 2020, doi: 10.1002/ADMA.201905682.
- [27] L. Larush *et al.*, “3D printing of responsive hydrogels for drug-delivery systems,” *J 3D Print Med*, vol. 1, no. 4, pp. 219–229, Oct. 2017, doi: 10.2217/3DP-2017-0009.
- [28] M. Nadgorny, Z. Xiao, C. Chen, and L. A. Connal, “Three-Dimensional Printing of pH-Responsive and Functional Polymers on an Affordable Desktop Printer,” *ACS Appl Mater Interfaces*, vol. 8, no. 42, pp. 28946–28954, Oct. 2016, doi: 10.1021/ACSAMI.6B07388.
- [29] G. Flamourakis *et al.*, “Laser-made 3D Auxetic Metamaterial Scaffolds for Tissue Engineering Applications,” *Macromol Mater Eng*, vol. 305, no. 7, pp. 1–9, 2020, doi: 10.1002/mame.202000238.
- [30] L. Song, M. F. Ahmed, Y. Li, C. Zeng, and Y. Li, “Vascular differentiation from pluripotent stem cells in 3-D auxetic scaffolds,” *J Tissue Eng Regen Med*, vol. 12, no. 7, pp. 1679–1689, 2018, doi: 10.1002/term.2695.
- [31] W. Zhang, P. Soman, K. Meggs, X. Qu, and S. Chen, “Tuning the poisson’s ratio of biomaterials for investigating cellular response,” *Adv Funct Mater*, vol. 23, no. 25, pp. 3226–3232, Jul. 2013, doi: 10.1002/ADFM.201202666.
- [32] Y. Yan, Y. Li, L. Song, C. Zeng, and Y. Li, “Pluripotent stem cell expansion and neural differentiation in 3-D scaffolds of tunable Poisson’s ratio,” *Acta Biomater*, vol. 49, pp. 192–203, Feb. 2017, doi: 10.1016/J.ACTBIO.2016.11.025.
- [33] B. N. L. Costa, R. M. R. Adão, C. Maibohm, A. Accardo, V. F. Cardoso, and J. B. Nieder, “Cellular Interaction of Bone Marrow Mesenchymal Stem Cells with Polymer and Hydrogel 3D Microscaffold Templates,” *ACS Appl Mater Interfaces*, vol. 14, no. 11, pp. 13013–13024, Mar. 2022, doi: 10.1021/ACSAMI.1C23442/ASSET/IMAGES/LARGE/AM1C23442_0005.JPEG.
- [34] A. Rodriguez-Garcia, J. Oliva-Ramirez, C. Bautista-Flores, and S. Hosseini, “3D in Vitro Human Organ Mimicry Devices for Drug Discovery, Development, and Assessment,” *Advances in Polymer Technology*, vol. 2020, 2020, doi: 10.1155/2020/6187048.

- [35] B. Bhaskar, R. Owen, H. Bahmaee, P. S. Rao, and G. C. Reilly, “Design and Assessment of a Dynamic Perfusion Bioreactor for Large Bone Tissue Engineering Scaffolds,” *Appl Biochem Biotechnol*, vol. 185, no. 2, pp. 555–563, Jun. 2018, doi: 10.1007/S12010-017-2671-5.
- [36] E. Babaliari, P. Kavatzikidou, A. Mitraki, Y. Papaharilaou, A. Ranella, and E. Stratakis, “Combined effect of shear stress and laser-patterned topography on Schwann cell outgrowth: synergistic or antagonistic?,” *Biomater Sci*, vol. 9, no. 4, pp. 1334–1344, Feb. 2021, doi: 10.1039/D0BM01218A.

5 List of publications

- 1) **G. Flamourakis**, I. Spanos, Z. Vangelatos, P. Manganas, L. Papadimitriou, C. Grygoropoulos, A. Ranella and M. Farsari, “Laser-made 3D Auxetic Metamaterial Scaffolds for Tissue Engineering Applications,” *Macromol. Mater. Eng.*, vol. 2000238, p. 10.1002/mame.202000238, 2020, doi: 10.1002/mame.202000238.
- 2) **G. Flamourakis**, A. Kordas, G. D. Barmparis, A. Ranella, and M. Farsari, “Low-autofluorescence, transparent composite for multiphoton 3D printing,” *Opt. Mater. Express*, vol. 11, no. 3, pp. 801–813, Mar. 2021, doi: 10.1364/OME.418269.
- 3) **G. Flamourakis**, A. Kordas, M. Papageorgiou, V. Pateraki, M. Farsari and A. Ranella, ‘High-Resolution lightweight and multifunctional one-photon 3D printed scaffolds for cell studies’ under submission in **Additive Manufacturing of Advanced Composites** journal
- 4) **G. Flamourakis**, P. Manganas, G. Bambaris, M. Farsari and A. Ranella, ‘The effect of Auxetic scaffolds in osteogenic differentiation of Mesenchymal Stem Cells’ under preparation

International Collaborations

- 5) Vangelatos, Z. *et al.* (2020) ‘Design and Testing of Bistable Lattices with Tensegrity Architecture and Nanoscale Features Fabricated by Multiphoton Lithography’, *Nanomaterials* . doi: 10.3390/nano10040652.
- 6) Z. Vangelatos, H. Moazam, P. S. Marcus, C. Grygoropoulos, V. Lopez, **G. Flamourakis** and M. Farsari “Strength through defects: A novel Bayesian approach for the optimization of architected materials,” *Sci. Adv.*, vol. 7, no. 41, 2021, doi: 10.1126/sciadv.abk2218.
- 7) Wang, C. *et al.* (2021) ‘Remodeling of Architected Mesenchymal Microtissues Generated on Mechanical Metamaterials’, <https://home.liebertpub.com/3dp>. doi: 10.1089/3DP.2021.0091.

6 List of conferences

1. Poster presentation: ‘Laser made Auxetic metamaterial scaffolds for tissue engineering applications’, “V summer school photonics meets biology” and 1st price poster, Heraklion, July 2019
2. Poster presentation ‘Laser made Auxetic metamaterial scaffolds for tissue engineering applications’, Tissue Engineering and Regenerative Medicine International Society conference (canceled due to coronavirus pandemic), Manchester, March 2020
3. Oral presentation: ‘Low-autofluorescence, transparent composite for multiphoton 3D printing’, ‘European Materials Research Society’ conference, online, June 2021
4. Oral presentation: ‘The effect of Auxetic environment in MSCs osteogenic differentiation’, Tissue Engineering and Regenerative Medicine International Society conference, Krakow, June 2022
5. Oral presentation: ‘The effect of Auxetic environment in MSCs osteogenic differentiation’ and Poster in ‘VI summer school photonics meets biology’ and ‘Best scientific discussion poster award’, Spetses, July 2022

7 Funding

1. Stavros Niarchos Foundation project ARCHERS (“Advancing Young Researchers’ Human Capital in Cutting Edge Technologies in the Preservation of Cultural Heritage and the Tackling of Societal Challenges”) 1 year scholarship
2. In2Sight: Innovative microchip for in vivo analysis of biomaterials



8 Disclaimer

All figures used from another sources were reproduced with permissions from the individual journals.